

Politecnico di Torino

ScuDo
Scuola di Dottorato ~ Doctoral School
WHAT YOU ARE, TAKES YOU FAR

Doctoral Dissertation
Doctoral Program in Electrical, Electronics and Telecommunications Engineering
(38^{th}cycle)

Electromagnetic Modeling and EMI Mitigation Techniques for EMC Analysis and Design Optimization in DC-DC Power Converters

By

Silvia Simone

******

Supervisor(s):
Prof. Fabio Pareschi, Supervisor
Prof. Gianluca Setti, Co-Supervisor

Doctoral Examination Committee:
Prof. Alessandro Trifiletti , Referee, Sapienza Università di Roma
Prof. Gaetano Palumbo, Referee, Università di Catania

Politecnico di Torino
2026

Declaration

I hereby declare that, the contents and organization of this dissertation constitute my own original work and does not compromise in any way the rights of third parties, including those relating to the security of personal data.

Silvia Simone
2026

* This dissertation is presented in partial fulfillment of the requirements for **Ph.D. degree** in the Graduate School of Politecnico di Torino (ScuDo).
* This publication is part of the project PNRR-NGEU which has received funding from the MUR - DM 352 / 2022.
* Part of the research presented in this dissertation was conducted in collaboration with STMicroelectronics at the Turin and Grenoble sites.

Abstract

Electromagnetic compatibility (EMC) has become a critical design consideration in modern electronic systems. As devices increase in complexity and operate at progressively higher frequencies, ensuring correct system operation within a given electromagnetic (EM) environment is essential to guarantee reliability and compliance with regulatory standards. Failure to meet EMC requirements may result in malfunctioning circuits, degraded signal integrity, and unpredictable system behavior.

DC–DC converters, widely used in power electronics for efficient voltage regulation, represent a particularly challenging case from an EMC perspective. Their high switching frequencies and steep transient currents inherently generate both conducted and radiated emissions. Conducted emissions propagate through power distribution networks, potentially affecting adjacent circuitry and compromising reliable operation. Radiated emissions, instead, may induce unintended coupling phenomena, interfering with nearby electronic systems. For these reasons, effective mitigation strategies are required from the earliest stages of the design process.

A widely adopted solution consists in the implementation of electromagnetic interference (EMI) filters. When properly designed and combined with optimized layout and packaging techniques, these filters enable compliance with EMC standards, reduce undesired EM coupling between subsystems and limit the impact of interference on the system's own operation. During the design process particular attention must be devoted to the interaction between the filter and the converter, since it can significantly influence system stability and dynamic response.

In this context, EM simulation tools play a fundamental role. Their adoption is essential for the accurate characterization of parasitic effects and EM interactions, which cannot be adequately captured using conventional circuit-level models.

In light of the considerations discussed above, this dissertation addresses the analysis, mitigation, and characterization of electromagnetic phenomena, particularly in DC–DC converters. EM disturbances are first examined through the identification of the primary mechanisms responsible for their generation and the investigation of how these phenomena affect overall system behavior and influence compliance with EMC requirements.

Subsequently, the state of the art in passive EMI filtering techniques is presented, with a focus on their design and optimization in DC–DC converters operating under Quasi-Square-Wave Zero-Voltage-Switching (QSW-ZVS) conditions, addressing the associated design trade-offs and damping strategies required to ensure effective EMI attenuation while preserving converter performance and proper operating conditions.

The work then provides an overview of the main commercial EM simulation tools, highlighting their capabilities, solution methods, and supported types of analysis. Afterward, particular emphasis is placed on the integration of EM simulation results into time-domain circuit simulations, enabling parasitic effects and EM interactions to be investigated under realistic operating conditions.

Finally, the use of EM simulators for the analysis of electromagnetic fields is discussed, with a focus on near-field magnetic emissions. The corresponding measurement techniques based on magnetic microprobes are discussed, together with the extraction and post-processing of simulation results to enable a direct comparison with the experimental measurements.

Contents

List of Figures viii

List of Tables xv

Nomenclature xvii

1 Electromagnetic Compatibility in Power Electronic Systems 1

1.1 Introduction 1

1.2 Fundamentals of EMC 3

1.2.1 Conducted Emissions 7

1.2.2 Radiated Emissions 11

1.3 EMI Mitigation Techniques and Oriented Design Considerations . . 15

1.3.1 EMI Filter 17

1.3.2 EM Simulations 22

2 EMI Passive filter for DC-DC converter 26

2.1 Design of passive filter 27

2.2 Optimization of damping element for DC-DC converter with ZVS . 42

3 Overview of EM simulators software and performed analysis 62

3.1 Analysis Workflow 63

3.2 Classification of EM simulator capability 66
3.2.1 Numerical Methods 67
3.2.2 Geometrical representation 76
3.2.3 Physical Modeling Regime 77
3.2.4 Validity limits of modeling approaches 79
3.3 Commercial EM simulator tools 85

4 Electromagnetic Modeling and Parasitic Extraction of Interconnect Systems 90
4.1 Quasi-static analysis 92
4.1.1 Port Definition and Simulation Settings 92
4.1.2 Derivation of parasitic inductance and resistance 96
4.1.3 Co-simulation between PCB and PKG 98
4.1.4 Time-domain model 109
4.2 Full-wave analysis 129
4.2.1 Port Definition and Simulation Settings 130
4.2.2 Derivation of parasitic inductance and resistance 133
4.2.3 Co-simulation in time domain 135
4.3 Broadband model 140
4.3.1 Measurement technique of low-impedance values 141
4.3.2 Model derivation 148
4.3.3 Time-domain model 150

5 Near-field magnetic probing 156
5.1 Near-field analysis 157
5.2 Experimental setup and measurement technique with magnetic micro-probe 160

5.3 Reconstruction of measurement output by EM simulation 166

6 Conclusions **174**

Publications **176**

References **177**

List of Figures

1.1 Schematic of DC-DC buck converter. 2

1.2 Main loop responsible for EMI generation and its equivalent RLC model after the turn-on of M_{HS}. 5

1.3 Overshoot and undershoot on the voltage at SW node of buck converter. 6

1.4 DM and CM conducted noise path in a buck converter as observed through a LISN in EMC compliance testing. 8

1.5 Graphical representation of conducted emission limits showing peak and quasi-peak detectors in CISPR standards. 11

1.6 Electric coupling mechanism due to SW voltage of DC-DC converter to Metal Chassis through capacitive coupling. 12

1.7 Measure of magnetic field around SW loop. 13

1.8 Spectrum of DM voltage obtained at the LISN for a DC-DC converter with a switching frequency of 1 MHz, without input EMI filter. . . . 19

1.9 Cascade system of LISN, EMI filter and DC-DC converter. 19

1.10 EMI filter topology: (a) LC filter and (b) π-filter. 20

1.11 Ideal attenuation of input EMI filter. 20

1.12 Spectrum of DM voltage obtained at the LISN for a DC-DC converter with the insertion of an input EMI filter. 21

1.13 Comparison of the workflows from design to hardware manufacturing with (a) and without (b) EM simulations. 24

2.1 System of DC-DC converter and input EMI LC filter. 29

2.2 Low-frequency small-signal model of the LC input filter with the switching regulator represented as a negative incremental resistance load. 31

2.3 Interconnection of two stable and independent subsystems in cascade. 33

2.4 Interconnection of two stable and independent subsystems in cascade. 34

2.5 Conservative stability condition ensuring that the output impedance of the input filter $Z_{\text{out,filter}}$ remains below the closed-loop input impedance of the converter $Z_{\text{in,DC-DC}}$. 35

2.6 Different damping strategies on LC input filter, with (a) a single resistor in parallel to filter capacitance, (b) a single resistor in parallel to filter inductance, and (c) a DC blocking capacitor in series to R_d. 38

2.7 Architecture of the QSW-ZVS DC-DC buck converter with EMI filter considered in this paper. 43

2.8 Main voltage and current waveforms in QSW-ZVS operation of the converter in Fig. 2.7. 44

2.9 The averaged small-signal model of the considered QSW-ZVS DC-DC Buck converter and the passive EMI filter. 45

2.10 High-level view of the averaged small-signal model shown in Fig. 2.9. (a) The EMI filter is modeled as an extra element in the small-signal representation of Fig. 2.9; (b) reference circuit model adopted for the computation of the impedances in (2.38). 48

2.11 Asymptotic construction of Bode plot of $|Z_d(j\omega)|$. 53

2.12 Comparison of $Z_o(s)$ and $Z_d(s)$ with minimum impedance levels for damping network design for traditional and QSW-ZVS modes in Table 2.7. (a) Case I, (b) case II and (c) Case III. 55

2.13 Ratio of the values of the damping elements over the entire operating range of the Buck converter computed according to the developed criteria. (a) Capacitance C_d^{Trad} and C_d^{ZVS} and (b) resistances R_d^{Trad} and R_d^{ZVS}. Case I, II and III in Table 2.7 are highlighted by red, blue and yellow markers, respectively. 56

2.14 TFs comparison without and with the EMI filter for both traditional and QSW-ZVS designs: (a) output impedance $Z_{\text{out}}(s)$, (b) control-to-output transfer function $G_{\text{vc}}(s)$, and (c) line-to-output transfer function $G_{\text{vg}}(s)$. 58

2.15 TFs comparison without and with the EMI filter for both traditional and QSW-ZVS designs: (a) output impedance $Z_{\text{out}}(s)$, (b) control-to-output transfer function $G_{\text{vc}}(s)$, and (c) line-to-output transfer function $G_{\text{vg}}(s)$. 59

2.16 EMI filter output impedances with different f_c designed to be constrained below the respective tracking lines, for traditional and QSW-ZVS mode. The bottom panel illustrates the relative variation of C_d^{ZVS} with respect to traditional case across the frequency. 60

3.1 Time domain waveform of switching node voltage of buck converter and its spectral envelope. 64

3.2 Classification of different main numerical methods adopted by EM simulators, highlighting in blue the region of applicability relevant to DC-DC converters. 68

4.1 Schematic representation of Source and Sink terminals in Q3D. . . . 93

4.2 Resistance and inductance behavior due to the skin effect and division of the frequency range into DC region, transition region and AC region. 95

4.3 Z-matrix converted from S-matrix obtained from electromagnetic simulation. (a): closing alternately the sink of each net to GND to compute the parasitic values of that net, (b): closing sink of every net to GND to compute the parasitic values between different nets. . 97

4.4 STMicroelectronics evaluation board based on (a) DC-DC converter buck regulator A6983CQTR (STEVAL-A6983CV1) and (b) synchronous iso-buck converter L6983I (STEVAL-L6983IV1). 99

4.5 Q3D simulation of the whole system constituted of PCB highlighted in dark blue and PKG in light blue. 100

4.6 EM simulation of the two separate system and cascade of the obtained results. 102

4.7 Representation of a two-port network. 103

4.8 Simulation of PCB (S1), simulation of PKG+signal traces connected to it (S2), and simulation of signal traces only (S3). 104

4.9 Comparison between (self) parasitic inductance and (self) resistance on the same net (computed for source1 on net1 and for source1 on net2) starting from Z-matrix (a) using the three different methods explained. 108

4.10 Comparison between (mutual) parasitic inductance and (mutual) resistance between two sources on different nets (from source1 on net1 to source1 on net2) obtained starting from Z-matrix (b) using the three different methods explained. 108

4.11 Equivalent model of parasitic values extracted at a single frequency with Q3D. 112

4.12 Ladder circuit for network synthesis with Foster 1st form (a) and Cauer 1st form (b). 114

4.13 Equivalent circuit for skin-effect loss and corresponding conductor ring definition. 116

4.14 Neikirk Ladder model. 117

4.15 Representation of the proposed equivalent circuit to reproduce the skin-effect behavior. 118

4.16 Comparison of resistance and inductance behavior of a PCB coil between proposed circuit, Kim and Neikirk iterative method and wanted value obtained from electromagnetic simulation. 122

4.17 Comparison of resistance and inductance behavior of a copper wire of a package between proposed circuit, Kim and Neikirk iterative method and wanted value obtained from electromagnetic simulation. 123

4.18 Different tools used for the data translation from frequency to time domain. 125

4.19 Broadband circuit generated from Q3D simulator to reproduce the variation of parasitic element in frequency of a generic N-port system. 126

4.20 (a) Circuit schematic of the DC–DC Buck converter with parasitic impedance, and terminals representing the differential ports of EM simulation. (b) Usually adopted method for first-order estimation of SW voltage. (c) Presented model of parasitic components. 136

4.21 Comparison between SW voltage of complete model of parasitic element (a), first approximation model (b) and proposed model (c). . 138

4.22 (a) Comparison between measurement of the real part of the loop impedance and the one derived from the model, and (b) measurement of imaginary part of the loop impedance divided by 2πf and the model. 140

4.23 Different configurations of impedance measurement for a DUT . . . 141

4.24 Magnitude of S-parameter as a function of DUT resistance for the three different impedance measurements methods. 142

4.25 Two-Port Shunt Through measurement with VNA, in this case with Bode 100. 142

4.26 Two-Port Shunt Through circuit configuration. 143

4.27 Representation of ground loop problem with generation of common mode current. 144

4.28 Measurement setup with Bode 100 (and Rigol RSA 3030N) as VNA, J2102B Common Mode Transformer, 2-port probe P2102A and PCB layout. 147

4.29 Comparison between parasitic (a) inductance and (b) resistance of the described PCB, obtained with measurement using Bode 100 and Rigol RSA 3030N VNA and with simulation employing Q3D and HFSS. 148

4.30 Proposed flow for the generation of an accurate time-domain model of parasitic suitable for SPICE-like circuit simulation. 149

4.31 (a) N-ports PCB, and different port configuration, considering one port as example, between (b) HFSS and Q3D for EM analysis and (c) ADS for the translation in the same format. 150

4.32 (a) Magnitude of the variation of the reflection coefficient S_{ii} in (4.40) varying the real and imaginary part of Z_{in}, fixing the reference impedance Z_0 to 50 Ω. (b) Variation of the real part of Z_{in} looking from port P1 (Fig.4.31-a) as a function of frequency, varying Z_0, and intersection with plane Z=Z_0 highlighted in red. 151

4.33 (a) Comparison between original and derived S-parameters obtained from the time-domain netlist when Z_0 is equal to 50Ω and when it is close to Z_{in} seen from port P1 (Fig.4.31-a). (b) Comparison of the parasitic inductance estimated from measurements with Bode 100 and Rigol VNA and evaluated from the netlist with different Z_0, after ensuring passivity for both. 153

4.34 Schematic of Buck converter and final equivalent model adding the netlist that reproduce EM simulation results. With this approach co-simulation between pure electrical and parasitic components can be performed within a time-domain simulator, in this case LTspice is employed and main voltage and current waveforms of the converter are represented. 155

5.1 TEM cell measurement standard setup. 157

5.2 Magnetic field detection with microprobe. 159

5.3 Langer microprobe with (a) vertical orientation and (b) horizontal orientation. 160

5.4 Complete setup of measurment using microprobe and IC scanner. . . 162

5.5 Test line on a Mini TEM cell used for H field measurement with microprobe and creation of the physical model in HFSS and the same plane used in the scanning environment. 166

5.6 Reproduction of the measurement environment. (a) HFSS simulation step and corresponding probe measurement step configuration. (b) Complete set of probe positions defined on the scanning plane. . . . 167

5.7 Correction factor K_H provided by Langer manufacturer. 169

5.8 Flow of simulation starting from the modeling of the structure, the definition of the observation plane above the PCB corresponding to the measurement scanning plane, and the resulting spatial distribution of the magnetic field component evaluated on this plane. 171

5.9 Comparison of the voltage amplitude in dBμV associated with the H_z magnetic field component obtained from (a) near-field measurements using a magnetic microprobe and (b) full-wave electromagnetic simulations performed in HFSS. 172

List of Tables

1.1 EMI standards by product sector 9

1.2 Noise classification in DC–DC converters 16

2.1 Parameters and coefficients of the small-signal circuit model in Fig. 2.9. 47

2.2 Parameters of the main TFs of the small-signal circuit model in Fig. 2.9. 49

2.3 Impedances derived with EET for traditional and QSW-ZVS operation modes. 51

2.4 Parameters in the expression of Z_d for traditional operation mode. . 52

2.5 Parameters in the expression of Z_d for QSW-ZVS operation mode. . 52

2.6 Buck converter component values. 54

2.7 Operating cases and corresponding parameter values. 54

2.8 Damping network component values and size reduction comparison between capacitance in traditional and QSW-ZVS mode. 56

2.9 Selected components with physical dimensions of damping network capacitors. 57

3.1 Comparison of commercial electromagnetic simulation tools based on numerical formulation, modeling regime, and typical application domains. 88

4.1 Performance comparison between the full sistem simulation, the standard cascade approach and the proposed approach. 107

Nomenclature

Acronyms / Abbreviations

CISPR	Comité International Spécial des Perturbations Radioélectriques
CM	Common-mode
DM	Differential-mode
EET	Extra Element Theorem
EM	Electromagnetic
EMC	Electromagnetic Compatibility
EMI	Electromagnetic Interference
EN	European Norms
EQS	Electro-quasi-static
EUT	Equipment under test
FEM	Finite Element Method
HS	High-side
IC	Integrated Circuit
IEC	International Electrotechnical Commission
LISN	Line Impedance Stabilization Network
LS	Low-side

LTI Linear time-invariant

MoM Method of Moments

PCB Printed Circuit Board

PR Positive-real

PS Power Stage

QSW-ZVS Quasi-Square-Wave Zero-Voltage-Switching

RE Radiated emissions

SMPS Switched Mode Power Supplies

SOA Safe operating area

SW Switching

TEM Transverse Electromagnetic

Mathematical Notation

$(\cdot)^{\dagger}$ Conjugate transpose (Hermitian transpose)

$(\cdot)^{\mathsf{T}}$ Transpose of a vector or matrix

$\mathfrak{I}(\cdot)$ Imaginary part

$\mathfrak{R}(\cdot)$ Real part

$\mathbf{M}$ Matrix

j Imaginary unit

Chapter 1

Electromagnetic Compatibility in Power Electronic Systems

1.1 Introduction

The continuous advancement of electronic technologies has led to a significant increase in the integration, performance, and operating frequency of modern electronic devices. As a consequence, the design of such systems can no longer be limited to ensuring their intended electrical functionality, but it must also account for their interaction with the surrounding Electromagnetic (EM) environment. During operation, electronic devices inherently generate EM disturbances that may propagate through conductive paths or radiate into free space, potentially affecting the performance of nearby systems. The ongoing trend toward miniaturization and higher switching speeds has further intensified these challenges. Modern electronic systems exhibit an increased tendency to generate Electromagnetic Interference (EMI), while simultaneously becoming more sensitive to frequency-dependent parasitic effects. These phenomena are intrinsically linked to the physical implementation of the system, including circuit layout, interconnections, and component packaging, and may significantly deviate the real behavior from ideal circuit-level predictions. As a result, the combined capability to effectively manage emission levels and the ability to accurately account for non-idealities has become a key requirement in the design of modern electronic systems. Conventional design approaches based

solely on schematic-level analysis are often insufficient to accurately capture the electromagnetic behavior of high-performance electronic systems.

Within this context, power electronic systems represent a particularly critical class of applications. Specifically, DC–DC converters play a fundamental role in providing efficient and controlled power conversion across a wide range of operating conditions. They are extensively employed in automotive, aerospace, industrial, and consumer electronics, where they are required to achieve high efficiency, reduced volume, and increased power density. These requirements are commonly met through fast-switching of semiconductor devices and high-frequency operation, which, however, make these converters significant sources of EM emissions. An high level view of a DC-DC buck converter is depicted in Fig. 1.1.

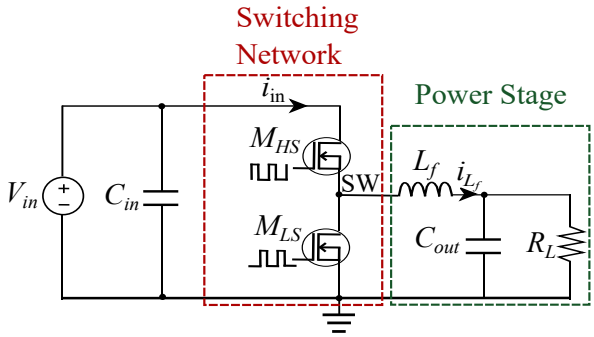


Fig. 1.1 Schematic of DC-DC buck converter.

The switching operation inherently associated with converters results in voltage and current transitions with high dv/dt and di/dt values. These rapid variation couple with the distributed parasitic elements of the system, including Printed Circuit Board (PCB) traces, interconnect structures, and power semiconductor packages. Consequently, DC–DC converters constitute prominent sources of conducted and radiated electromagnetic interference, potentially impacting the operation of neighboring subsystems sharing common power paths or operating within the same electromagnetic environment.

To address these challenges, the discipline of Electromagnetic Compatibility (EMC) has emerged as a fundamental pillar in the design of modern electronic systems. EMC is defined as the ability of a device or system to operate as intended in its EM environment without introducing unacceptable disturbances to other systems

and without being adversely affected by external EM phenomena. This definition inherently encompasses two complementary aspects: the limitation of EM emissions and the ability of a system to withstand external interference. On the other side, the evaluation and mitigation of frequency-dependent parasitic effects require advanced EM modeling techniques, which enable the identification of parasitic behaviors.

The present chapter focuses on the core principles and regulatory aspects of EMC, particularly in power electronic systems, introducing the fundamental mechanisms underlying conducted and radiated EMI generation and presenting design-oriented techniques aimed at reducing electromagnetic disturbances. The use of EM simulators for the precise characterization and integration of parasitic effects into system design will be addressed in the subsequent chapters.

1.2 Fundamentals of EMC

EM disturbances can be broadly classified into conducted and radiated emissions. Conducted emissions propagate along physical electrical connections, such as power supply lines, signal traces, or interconnects, and may affect other devices connected to the same network. Radiated emissions, in contrast, arise from EM fields that couple through free space, potentially influencing nearby systems even in the absence of direct electrical connections. Both types of emissions originate from rapid voltage and current transitions within the system and are often exacerbated by high switching frequencies, compact layouts, and intrinsic parasitic elements. While EM emissions describe the generation of unwanted EM energy, the response of a system to external disturbances is characterized by its susceptibility and immunity. Susceptibility quantifies the degree to which a system is influenced or perturbed by unwanted EM energy from external sources, whereas immunity denotes its capability to maintain correct and stable operation under such conditions. The interplay of these factors—emissions, susceptibility, and immunity—ultimately determines whether a system can be regarded as electromagnetically compatible.

From a system-level perspective, EMC issues arise from the interaction of three fundamental elements: a source of interference, a coupling path, and a susceptible receiver. The source generates unwanted EM energy, the coupling path allows its

propagation, either through conduction or radiation, and the receiver is affected by the disturbance. This framework identifies three complementary mitigation strategies: reducing emissions at the source, interrupting or attenuating the coupling path, and enhancing the immunity of the affected system. Effective implementation of EMC principles therefore relies on a systematic identification of these elements and on the adoption of proper techniques. Addressing these isues only during the final testing phases often results in costly redesigns, extended development timelines, and suboptimal solutions. When instead, these considerations are incorporated from the early stages of the design process, it becomes possible to develop electronic systems that operate reliably and satisfy the constraints imposed by their intended application context.

Accordingly, EMC requirements are regulated through international standards and directives. In the United States, the Federal Communications Commission (FCC) establishes legally binding emission limits for electronic devices. At the international level, electromagnetic compatibility standards are developed by the Comité International Spécial des Perturbations Radioélectriques (CISPR), operating under the International Electrotechnical Commission (IEC), which is responsible for the standardization of electrical and electronic technologies. In Europe, these IEC/CISPR standards are adopted by the European Committee for Electrotechnical Standardization (CENELEC) and published as harmonized European Norms (EN), which provide presumption of conformity with the EMC Directive. Within this international regulatory framework, Mutual Recognition Agreements (MRAs) facilitate the mutual acceptance of EMC test results between different regions, reducing redundant compliance testing. Compliance with these standards is mandatory for devices across different application domains, and the responsibility for ensuring conformity prior to system deployment lies with the manufacturer.

In switching DC–DC converters, the most critical region from an EM standpoint is represented by the high-frequency power loop, illustrated in Fig 1.2.

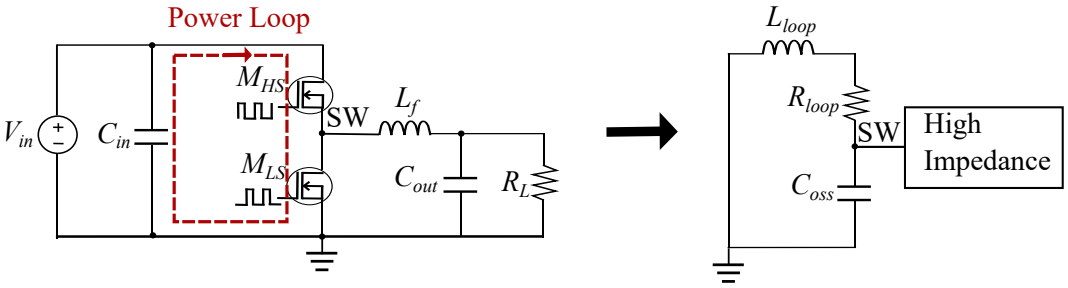


Fig. 1.2 Main loop responsible for EMI generation and its equivalent RLC model after the turn-on of M_{HS}.

This loop, in a buck converter, is formed by the input decoupling capacitor C_{in}, the high-side (HS) and low-side (LS) MOSFET (i.e. M_{HS}, M_{LS}), and the associated interconnections. During each switching transition, a large current commutation takes place within this loop over a very short time interval. The resulting current slew rate is therefore significantly high. The high-frequency behavior of the power loop is dominated by its parasitic elements, which arise from the physical implementation of the circuit. In particular, the finite geometry of the loop gives rise to a parasitic inductance, which includes contributions from PCB traces, vias, plane and device packages. Considering for example the moment in which the HS MOSFET turns on and the LS MOSFET turns off, an effective capacitance is present at the switching node (SW), mainly associated with the output capacitance of the MOSFET that is turned off, along with additional stray capacitances to reference planes and surrounding conductive structures.

When analyzed from a high-frequency, EMI-oriented perspective, the switching loop can therefore be approximated by an equivalent series RLC network, also depicted in Fig. 1.2. In this representation L_{loop} models the total power loop parasitic inductance, the effective capacitance C_{oss} is dominated by the MOSFET output capacitance at the switching node, and a lumped resistance R_{loop} accounts for the loss behavior within the loop, including MOSFET on-state resistance, equivalent series resistance of capacitive elements and conductive losses in the interconnections.

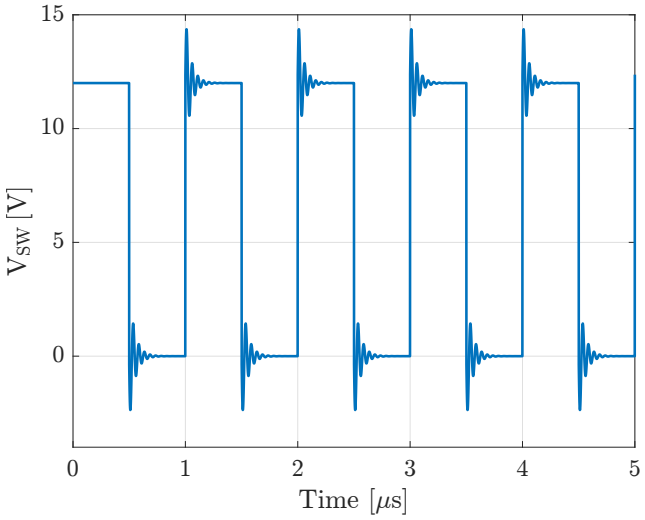


Fig. 1.3 Overshoot and undershoot on the voltage at SW node of buck converter.

The excitation of this parasitic RLC network occurs during the switching transitions. This process gives rise to a damped high-frequency oscillation, commonly referred to as ringing. This phenomenon is directly observable on the switching-node voltage waveform, as illustrated in Fig. 1.3. The natural resonance frequency of this oscillation is determined by the parasitic elements of the loop and can be expressed as

$$f_0 = \frac{1}{2\pi\sqrt{L_{\text{loop}}C_{\text{oss}}}}. \tag{1.1}$$

The dynamics of the power loop described above represent a fundamental mechanism of EM disturbance generation in buck converters. Once generated, these high-frequency components can propagate through the electrical interconnections of the system and couple to the surrounding environment through conductive and capacitive paths. As a result, the parasitic behavior of the power loop constitutes a primary link between the switching operation of the converter and the resulting conducted and radiated EM emissions, which are ultimately assessed in EMC compliance measurements. On the basis of this interpretation, the mechanisms of conducted and radiated EM emissions are discussed in detail in the following sections.

1.2.1 Conducted Emissions

Conducted emissions (CE) arise from the generation of unwanted EM energy within an electronic system that is transferred to external circuits through physical electrical connections, such as power supply lines and signal interconnections. In power electronic systems, and in particular in switching DC–DC converters, these emissions are primarily associated with the intrinsic switching behavior of semiconductor devices and the non-ideal characteristics of the circuit implementation. Once injected into the electrical network, the resulting disturbances can propagate over extended distances, potentially affecting other interconnected systems and contributing to the overall EMI environment.

From a physical perspective, conducted EM emissions can be classified into two distinct components [1], namely differential-mode (DM) and common-mode (CM) disturbances. This distinction is fundamental as DM and CM currents arise from different mechanisms and propagate along different paths.

- DM conducted currents are associated with signal or power currents flowing in opposite directions along a pair of conductors. These currents are typically aligned with the intended functional operation of the circuit and flow within a closed loop formed by the forward and return conductors. As a result, DM disturbances are often referred to as symmetric or transverse mode signals. From an EM standpoint, DM currents are primarily driven by time-varying currents and are therefore closely related to high di/dt phenomena.

- CM conducted currents, in contrast, correspond to currents flowing in the same direction along multiple conductors with respect to a common reference, such as chassis ground or earth. The return path of CM currents is generally not a dedicated conductor but is distributed through parasitic capacitances, ground structures, or the surrounding environment. For this reason, CM disturbances are also referred to as asymmetric or longitudinal mode signals. CM currents are predominantly driven by time-varying voltages and are thus strongly associated with high dv/dt events.

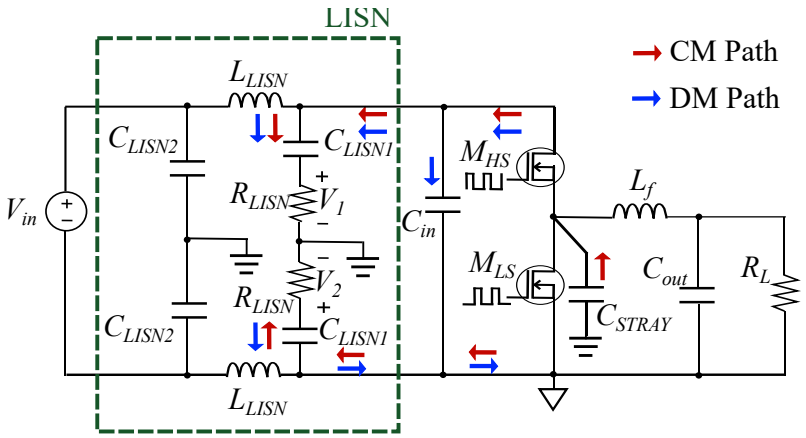


Fig. 1.4 DM and CM conducted noise path in a buck converter as observed through a LISN in EMC compliance testing.

To illustrate the physical meaning of these concepts, a practical example can be considered in the context of a typical buck converter as represented in Fig. 1.4. In this system, DM noise is generated between the supply line and the corresponding return line, following the main power delivery path. CM noise, on the other hand, is generated between the supply lines and the ground plane, (e.g. the copper test table), through stray parasitic capacitances, denoted as C_{STRAY}. These capacitive paths provide a return route for CM currents that is external to the intended power circuit and often extends over a much larger spatial region. Between the power supply and the buck converter, a Line Impedance Stabilization Network (LISN) is inserted for conducted EMC testing [2, 3].

The LISN establishes a controlled interface between the equipment under test (EUT) and the external power network. Its primary role is to present a well-defined and reproducible impedance to the EUT over the regulated frequency range, while simultaneously isolating the measurement environment from undesired external disturbances. By doing so, the LISN ensures that the measured noise levels depend primarily on the emission characteristics of the EUT rather than on variations in the supply network impedance.

In this configuration, the LISN provides a standardized impedance of $50\,\Omega$ with respect to the reference ground for each supply line. The noise voltages appearing at the LISN terminals, commonly denoted as V_1 and V_2, represent the conducted disturbances on the supply and return conductors, respectively. The DM noise

voltage can be obtained as half of the difference between the measured line voltages,

$$V_{DM} = \frac{V_1 - V_2}{2}, \tag{1.2}$$

whereas the CM noise voltage is defined as half of their sum,

$$V_{CM} = \frac{V_1 + V_2}{2}. \tag{1.3}$$

The high-frequency ringing generated within the power loop has direct and significant implications for conducted EMI [4–8]. The oscillatory voltage at the SW node introduces additional rapid voltage variations superimposed on the nominal switching transition. These fast voltage changes increase the effective voltage slew rate. Since displacement currents through parasitic capacitances are directly proportional to the time derivative of the voltage at the SW node, these rapid voltage variations enhance capacitive coupling toward reference structures, thereby increasing CM conducted emissions. Simultaneously, the interaction between the parasitic loop inductance and the rapid current commutation injects high-frequency noise components into the supply path and thus exacerbating DM conducted emissions. For these reasons, the high-frequency power loop represents the primary source of conducted EM disturbances in synchronous buck converters [9, 10]. Its parasitic inductance, in particular, establishes a direct link between circuit layout, voltage overshoot across the switching devices, and overall EMI performance. Consequently, minimizing the loop area and carefully controlling the associated parasitic elements are essential not only for reducing voltage stress and improving device reliability, but also for mitigating CE at their source.

The limits imposed on conducted emissions generated by electronic equipment are defined by regulatory bodies and vary depending on the application domain, as illustrated in Table 1.1.

Table 1.1 EMI standards by product sector

Product Sector	**CISPR Standard**	**EN Standard**	**FCC Standard**
Automotive	CISPR 25	EN 55025	–
Multimedia	CISPR 32	EN 55032	Part 15
ISM	CISPR 11	EN 55011	Part 18

In the automotive sector, EM compatibility requirements are specified by CISPR 25. Measurements are typically carried out using one or two 5 μH / 50 Ω Artificial Networks (ANs), functionally equivalent to LISNs depending on the grounding configuration of the device under test. The most stringent requirement corresponds to Class 5, which ensures compliance across frequency bands allocated to broadcast radio and mobile communication services. The relevant frequency range extends from 150 kHz to 108 MHz.

For information technology and multimedia equipment, the initial applicable standard was CISPR 22, which has been replaced by CISPR 32 [11]. Conducted emission measurements are generally performed over the range from 150 kHz to 30 MHz. Equipment is classified according to its intended operating environment: Class B applies to devices used in residential contexts and imposes stricter limits, whereas Class A refers to equipment intended for non-residential environments with less stringent requirements. Measurements are performed using a 50 μH / 50 Ω V-type Line LISN.

EM disturbances generated by industrial, scientific, and medical (ISM) radio-frequency equipment are regulated by CISPR 11 [12]. This standard distinguishes between Group 1 equipment, intended for general-purpose applications, and Group 2 equipment, which includes RF-specific devices. Each group is further divided into Class A and Class B. Class A equipment is intended for use in all environments other than residential settings and may be evaluated either in dedicated test sites or in situ, whereas Class B equipment is designed for domestic environments and is tested under controlled conditions. For Class B devices, the emission limits are consistent with those defined in CISPR 32, while for Class A the limits depend on the equipment category and power level.

A representative example of CISPR conducted emission limits is presented in Fig. 1.5 to illustrate the regulatory constraints discussed above. The figure shows a typical limit profile as a function of frequency, highlighting the peak and quasi-peak detector levels commonly specified in CISPR standards. Although the exact limits and detector characteristics depend on the specific standard and equipment class, this example clarifies the frequency-dependent behavior and relative stringency of the constraints.

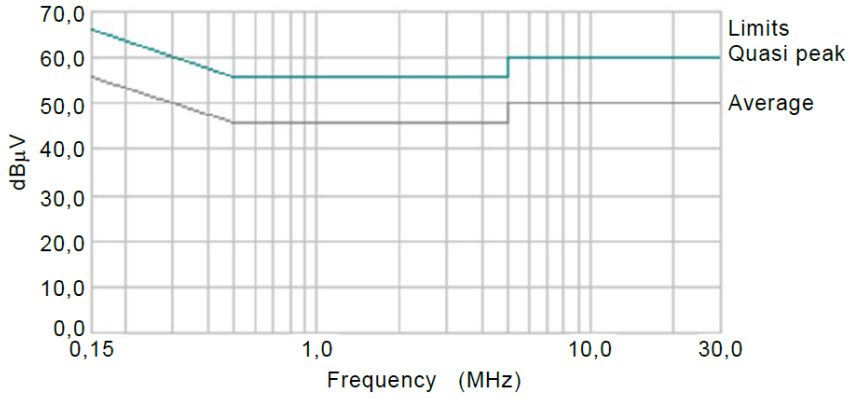


Fig. 1.5 Graphical representation of conducted emission limits showing peak and quasi-peak detectors in CISPR standards.

1.2.2 Radiated Emissions

Radiated emissions (RE) arise from EM disturbances that propagate through space in the surrounding environment as electric and magnetic fields, without requiring a direct conductive path between source and victim. In contrast, radiated susceptibility refers to the ability of a system to operate correctly in the presence of externally generated EM fields.

In switching DC–DC converters, radiated emissions originate from high frequency voltage and current transients inherently associated with semiconductor commutation [13–15]. These rapid variations excite nearby conductive structures, which behave as unintended radiators. Unlike conducted emissions, which are confined to defined electrical paths, radiated emissions are governed by the interaction between these high-frequency phenomena and the physical geometry of the system. As a result, disturbances generated within the converter can excite resonant modes of the surrounding interconnection network, making radiated behavior strongly dependent on the overall system configuration.

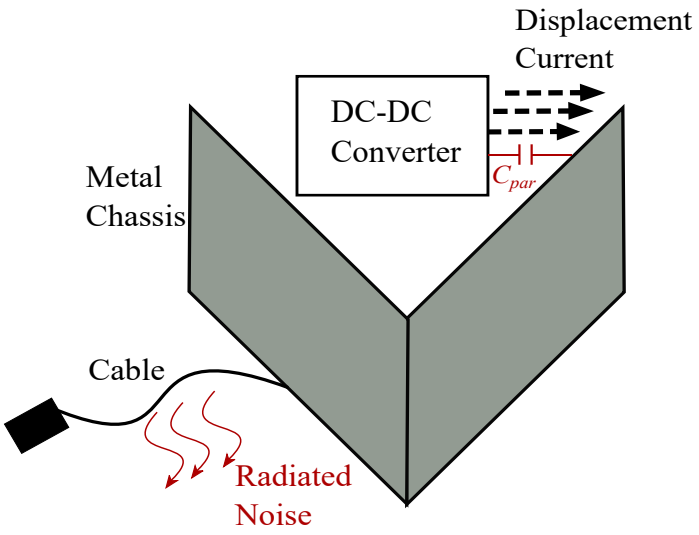


Fig. 1.6 Electric coupling mechanism due to SW voltage of DC-DC converter to Metal Chassis through capacitive coupling.

Two main coupling mechanisms govern the generation of radiated emissions [16]. The first is electric coupling, primarily associated with high dv/dt nodes such as the SW node. Rapid voltage transitions at this node produce displacement currents through parasitic capacitances between the PCB and nearby conductive structures. These currents generate CM voltages that can drive extended conductors, such as cables, which then act as efficient radiating elements. Considering for example a voltage on the SW node that goes from 0 to 12V in $5ns$ and a C_{STRAY} of 150 fF between that node and the chassis, a peak current of 360 μA is driven from the chassis into the PCB, which in turn produces a CM voltage that excites the surrounding antenna structures, as can be seen in Fig 1.6.

The second mechanism is magnetic coupling, associated with high di/dt current loops. The main switching loop, affected by parasitic LC ringing, produces time-varying magnetic fields that can couple to adjacent structures or drive an antenna structure, as represented in Fig. 1.7 from the near field scanning result of a magnetic loop probe around the SW loop. The effectiveness of this coupling is strongly dependent on the loop area therefore minimizing loop size the magnetic coupling can be reduced.

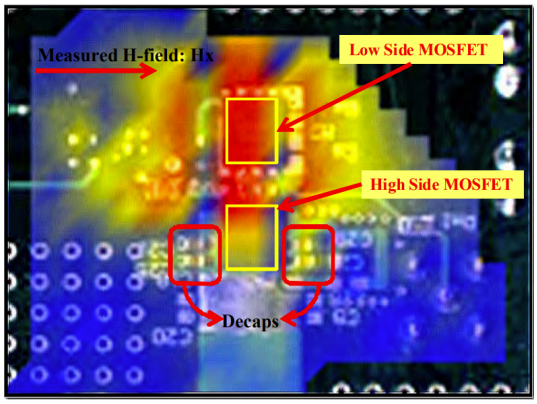


Fig. 1.7 Measure of magnetic field around SW loop. Picture from [10]

As previously analyzed, DM currents flow in closely coupled forward and return paths, forming compact loops thus generating limited radiation efficiency, although they still contribute at higher harmonics through their magnetic dipole nature. In contrast, CM currents involve distributed return paths through ground planes, chassis, and external wiring, leading to much larger effective loop areas and higher radiation capability.

Moreover, conducted disturbances can propagate along both input and output paths and interact with external interconnections. When these currents flow through extended structures such as cables, they may excite resonances or couple to nearby conductive elements, effectively converting conducted noise into radiated emissions.

Consequently, radiated emissions must be addressed as a system-level phenomenon. Their magnitude and spectral content are strongly influenced by layout-dependent parasitics, as well as by design choices such as loop geometry, trace routing, SW node placement, grounding strategy, and cable routing. Effective mitigation therefore requires minimizing high-frequency loop areas and reducing capacitive coupling to reference structures.

Radiated EM emission requirements are intended to limit the fields generated by electronic equipment and to prevent harmful interference with radio communication services.

In the automotive sector, radiated emission requirements are primarily defined within the framework of CISPR standards and international vehicle regulations.

CISPR 25 specifies radiated emission limits and test methods intended to protect on-board radio receivers, while CISPR 12 addresses the protection of off-board radio services. In addition, regulatory compliance for complete vehicles and electronic subassemblies is governed by United Nations Economic Commission for Europe (UNECE) Regulation 10, which references CISPR standards as the technical basis for radiated emission evaluation. Radiated emission measurements are performed over frequency ranges that typically extend from 30 MHz up to 1 GHz, with extensions up to 2.5 GHz in CISPR 25 to cover modern wireless communication services. The limits are specified using peak and average detector functions, and the applicable class depends on the required level of protection for the intended automotive application.

For information technology and multimedia equipment, radiated emission requirements are specified by CISPR 32. These requirements apply to equipment supplied by AC or DC voltages up to 600 V and define radiated field-strength limits typically evaluated over the frequency range from 30 MHz to 1 GHz, with additional limits above 1 GHz depending on the highest internal operating frequency of the device. Equipment is classified into Class A and Class B, corresponding to non-residential and residential environments, respectively, with Class B imposing more stringent limits. Radiated emission measurements are carried out in semi-anechoic chambers or open-area test sites using standardized antenna distances, receiver bandwidths, and detector functions.

Radiated emissions from ISM equipment are regulated by CISPR 11. This standard applies to a wide range of products that intentionally or unintentionally generate radio-frequency energy and distinguishes between Group 1 and Group 2 equipment based on the intended use of RF energy. Each group is further subdivided into Class A and Class B depending on the operating environment. Radiated emission limits are specified over frequency ranges relevant to broadcast and communication services.

1.3 EMI Mitigation Techniques and Oriented Design Considerations

Building upon the general principles of EMC introduced in the previous section, it becomes evident that DC–DC converters require a dedicated oriented design approach. In practical applications, they are embedded within multi-functional electronic platforms, often sharing power distribution networks with sensitive analog, digital, and communication subsystems. In such environments, insufficient control of EM emissions may lead to system-level performance degradation, malfunction, or non-compliance with applicable EMC standards.

Moreover, parasitic effects significantly impact the internal electrical behavior of DC–DC converters. The inclusion of parasitic elements associated with the PCB layout, interconnections, and device packaging enables a more realistic representation of converter waveforms during switching operation. For instance, the analysis of the SW node allows the identification of parasitic contributions to voltage overshoots and ringing phenomena occurring during switching transients. Accurately capturing these effects is essential for evaluating whether semiconductor devices operate within their respective safe operating areas (SOAs) , especially under worst-case switching conditions. Furthermore, the assessment of voltage and current waveforms across the switching elements, when parasitic effects are properly accounted for, enables a more reliable estimation of switching and conduction losses. This information is crucial for thermal management, efficiency optimization, and long-term reliability analysis. In addition, parasitic-aware modeling improves the prediction of output voltage ripple, providing insight for the appropriate sizing and selection of output filtering components, as well as for ensuring converter stability under dynamic load conditions. Similarly, an accurate representation of the input current waveform, including high-frequency components induced by switching action, is essential for the proper design of input filtering solutions.

Based on the discussion presented in the previous sections on conducted and radiated emissions, the EMI behavior of DC–DC converters can be interpreted in terms of a limited set of dominant mechanisms acting over different frequency regions [17]. A simplified classification of the main noise contributions, based

on their physical origin, spectral extent, and coupling mechanism, is reported in Table 1.2.

Table 1.2 Noise classification in DC–DC converters

Noise Type	**Dominant Noise Source**	**Frequency Range**	**Emission Type**
Low-frequency	Switching-frequency harmonics	150 kHz - 50 MHz	Conducted
Broadband	Switch-node ringing due to power-loop parasitics	50 MHz - 300 MHz	Conducted & Radiated
High-frequency	Body-diode reverse recovery	Above 200 MHz	Radiated

Overall, this classification shows that EMI in DC–DC converters includes both conducted and radiated components distributed over a broad frequency range.

Consequently, the achievement of EMC in DC–DC converters relies on the combined application of complementary techniques that address both the suppression of EM disturbances at the system interfaces and the control of the physical mechanisms responsible for their generation. A comprehensive and predictive EMC-oriented design methodology therefore relies on the integration of EMI mitigation strategies with accurate electromagnetic modeling approaches. In this regard, two key aspects play a central role in EMC-oriented DC–DC converter design.

- The first aspect concerns the implementation of EMI filtering solutions, which are primarily aimed at attenuating conducted emissions and limiting the propagation of switching noise through power and signal connections. When properly designed, EMI filters provide an effective means of ensuring compliance with emission limits while reducing the interaction between the converter and the external EM environment.

- The second aspect involves the use of EM simulations, which enable the analysis and prediction of frequency-dependent parasitic effects arising from the physical implementation of the converter. EM modeling supports the identification and characterization of parasitic coupling paths and layout-induced phenomena, thereby supporting a more predictive and robust design process.

These two approaches are inherently complementary, while EMI filters operate at the system level to reduce disturbances, EM simulations address the underlying physical mechanisms responsible for their generation within the converter structure. An integrated consideration of both aspects is therefore essential for the realization of EMC-compliant DC–DC converters in modern power electronic systems. In this context, the following sections introduce the fundamental principles of EMI filtering in DC–DC converters and discuss the role of EM simulations in the accurate modeling of parasitic effects and their integration into the overall design flow.

1.3.1 EMI Filter

In high-density DC–DC converter designs, the implementation of a compact and effective EMI input filter represents one of the most critical engineering challenges. Due to the employment of passive elements, the input filter often constitutes a significant fraction of the overall converter footprint, in some cases accounting for a substantial portion of the total solution volume. As converter power density continues to increase, the ability to integrate an EMI filter that combines high attenuation performance with reduced size and losses becomes a key enabling factor.

The input EMI filter fulfills several essential functions within the power conversion system.

- It conditions the input current drawn by the converter, suppressing the high frequency harmonic components introduced by the switching action and ensuring that the average input current remains predominantly direct current.
- It limits the propagation of conducted electromagnetic disturbances generated by the switching process, preventing both differential-mode and common-mode noise from reaching the upstream power lines and interfering with neighboring

subsystems or sensitive equipment. This aspect is of particular importance in environments such as automotive and industrial applications, where multiple electronic systems share the same power distribution network.

- The input filter enhances the immunity of the converter and its load by attenuating disturbances originating from the supply side, including voltage transients, surges, sags, and burst-type events, thereby improving overall system robustness.

From a design perspective, the synthesis of an EMI input filter involves the simultaneous satisfaction of multiple, and often competing, objectives. Foremost among these is compliance with international EMC regulations governing conducted emissions, which impose stringent attenuation requirements on both differential-mode and common-mode noise over specified frequency ranges. At the same time, the filter must incorporate adequate damping to control resonant behavior and limit the peak value of its output impedance, ensuring stable interaction with the converter.

The practical design of EMI input filters therefore requires a balanced approach that accounts not only for attenuation targets, but also for stability, efficiency and physical integration, and economic constraints. These considerations form the basis for the analysis and design methodologies.

In this section, the focus is placed on EMI filters intended for the mitigation of DM conducted disturbances, as these constitute one of the dominant contributions to conducted emissions in DC–DC converters over the frequency range of primary interest.

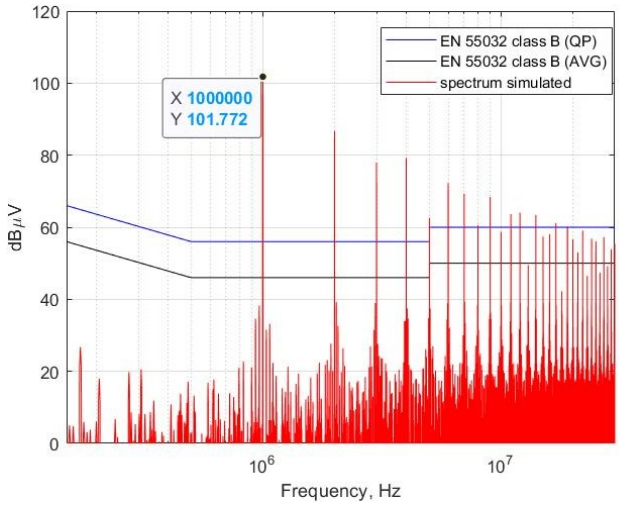


Fig. 1.8 Spectrum of DM voltage obtained at the LISN for a DC-DC converter with a switching frequency of 1 MHz, without input EMI filter.

The effectiveness of the EMI input filter can be clearly illustrated by examining the conducted emission spectrum obtained at the converter input through a LISN. Figure 1.8 shows an example of the magnitude of the conducted emissions detected at the LISN terminals in the absence of any input filtering. As expected for a switching DC–DC converter, the spectrum is characterized by pronounced peaks at the switching frequency and its low-order harmonics, which dominate the conducted emission profile over the frequency range of interest. These components clearly exceed the applicable CISPR conducted emission limits, demonstrating that, without filtering, the converter does not satisfy EMC requirements.

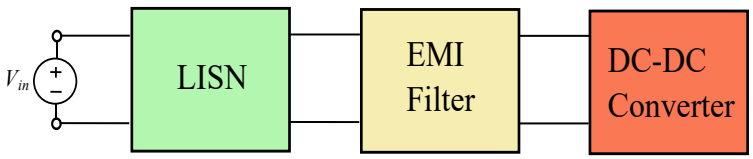


Fig. 1.9 Cascade system of LISN, EMI filter and DC-DC converter.

To mitigate these disturbances, the EMI input filter is introduced between the converter and the LISN, as shown in Fig. 1.9. Conducted electromagnetic interference in DC–DC converters is commonly mitigated using passive low-pass filter networks designed to attenuate high-frequency DM noise propagating along the power lines.

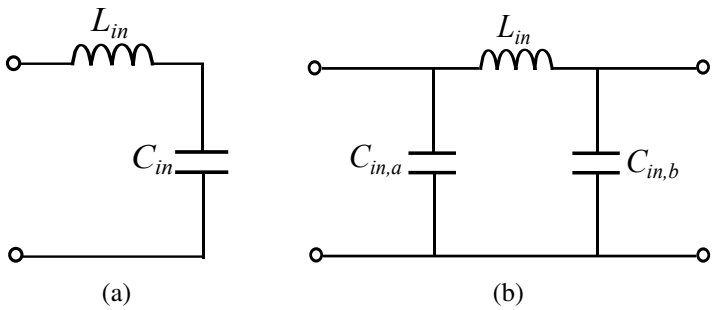


Fig. 1.10 EMI filter topology: (a) LC filter and (b) π-filter.

The most widely adopted topologies for DM noise suppression are LC and π-type filters, owing to their simplicity, effectiveness, and ease of integration, the filters configuration is reported in Fig. 1.10(a) and Fig. 1.10(b) respectively.

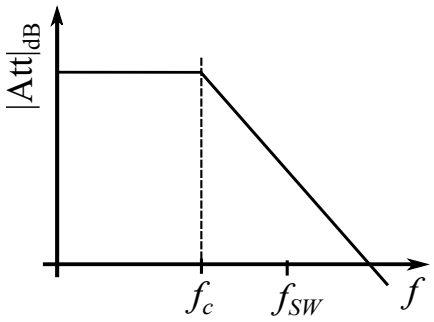


Fig. 1.11 Ideal attenuation of input EMI filter.

The EMI input filter is implemented as a low-pass network characterized by a cutoff frequency f_c, which defines the boundary between the passband and the stopband of the filter. Below f_c, the filter exhibits negligible attenuation, allowing the DC component and low-frequency variations of the input signal to propagate without significant distortion. Above f_c, the filter increasingly attenuates higher-frequency components, according to its characteristic roll-off. In order to ensure effective mitigation of conducted emissions, the cutoff frequency must be selected sufficiently lower than the converter switching frequency f_{SW}. This separation guarantees that the dominant spectral components generated by the switching action, which are concentrated around f_{SW} and its harmonics, lie well within the stopband of the filter, where significant attenuation is achieved. The ideal attenuation profile of the target

filter is depicted in Fig. 1.11, where the relative position of the cutoff frequency f_c with respect to the switching frequency f_{SW} is highlighted.

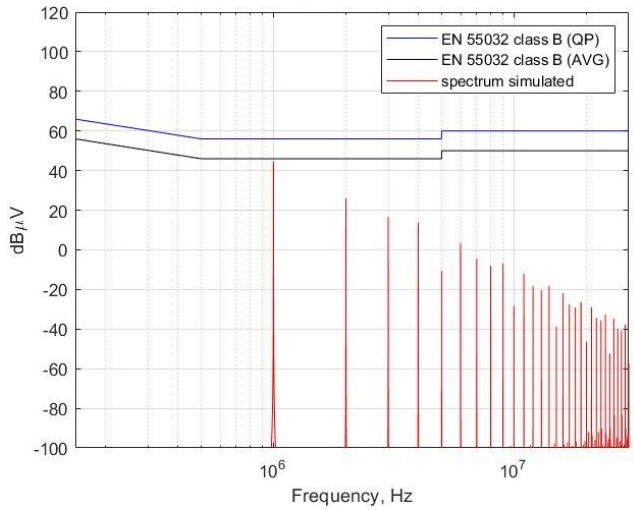


Fig. 1.12 Spectrum of DM voltage obtained at the LISN for a DC-DC converter with the insertion of an input EMI filter.

After the insertion of the EMI input filter, the amplitude of the switching-related harmonics is reduced across the frequency range of interest. As shown in Fig. 1.12, the conducted emission spectrum measured at the LISN terminals exhibits an attenuation of 4 dB at the most critical harmonic components, which is sufficient to bring the emission levels below the applicable CISPR limits, thereby ensuring compliance over the entire measured frequency range.

While the attenuation of conducted emissions constitutes a primary objective in EMI input filter design, the filter cannot be regarded as an electrically isolated element within the overall converter system. Its inclusion inherently modifies the impedance environment seen by the DC–DC converter and may interact with its internal dynamics. As a result, the design process must explicitly account for the potential impact on system stability and ensure that the fundamental small-signal characteristics of the converter are preserved. The stability of the coupled filter–converter system and the preservation of dynamic performance are critical in practical implementations and are therefore examined in detail in the following Chapter.

1.3.2 EM Simulations

As discussed in the previous sections, consider EM aspect in DC–DC converters requires design approaches capable of addressing both system-level emissions and layout-dependent physical phenomena. In this context, EM simulations play a crucial role, as they directly relate the physical implementation of the converter to its electrical behavior.

Parasitic effects associated with the PCB layout, interconnections, and semiconductor packaging introduce frequency-dependent behaviors that cannot be adequately captured by conventional circuit-level simulations alone. While this analysis remains essential for verifying converter functionality, it relies on models that neglect the real physical structures of the system.

EM simulations are therefore employed to consider parasitic resistances, inductances, capacitances, and coupling mechanisms arising from the converter implementation. By incorporating the results of EM analysis during the early stages of the design flow, the impact of parasitic phenomena on circuit operation can be assessed prior to physical prototype fabrication. This predictive approach enables the identification and mitigation of critical issues in the initial phases of the design process, thereby reducing the risk of costly downstream design iterations and increasing confidence in meeting performance, reliability, and compliance requirements.

A comprehensive prediction of EM effects on DC–DC converter operation requires the combined analysis of both the electrical and physical domains. This is typically achieved through an EM/circuit co-simulation, in which EM-derived models of the PCB, package, and interconnect structures are combined with circuit-level models of active and passive components. As a result, EM simulators characterize the frequency-dependent behavior of physical structures, whereas SPICE-based circuit simulators capture the response of the electrical system components.

The general procedure for predicting the impact of parasitic effects on the final DC–DC converter system can be summarized as follows [18]:

- Design of the circuit schematic, using ideal or manufacturer-provided circuit models of active and passive components.

- Execution of a pure circuit simulation, in which the schematic is simulated without explicitly considering PCB or package parasitic effects.
- Design of the PCB layout and package interconnection.
- EM simulation of the physical layout to extract parasitic effects, represented in either the frequency domain or the time domain.
- Co-simulation of the circuit schematic with the EM-extracted models, enabling the inclusion of parasitic effects that are not present in the original schematic representation.

Through this workflow, the influence of parasitic effects on voltage and current waveforms can be systematically analyzed.

Although specific implementations may vary depending on the selected simulation tools, EM analysis environments generally follow a similar workflow. The main steps involved in performing an EM analysis can be summarized as follows:

- *Creation of the physical model*: definition of layout geometry, conductor shapes, layer stack-up, and material properties.
- *EM simulation setup*: assignment of ports, boundary conditions, excitation sources, and solver configuration settings.
- *Execution of the EM simulation*: discretization of the physical model through appropriate meshing techniques and numerical solution of the EM field equations.
- *Post-processing of results*: extraction and computation of quantities of interest, such as parasitic RLCG parameters, impedance frequency behavior, current distributions, and coupling effects.

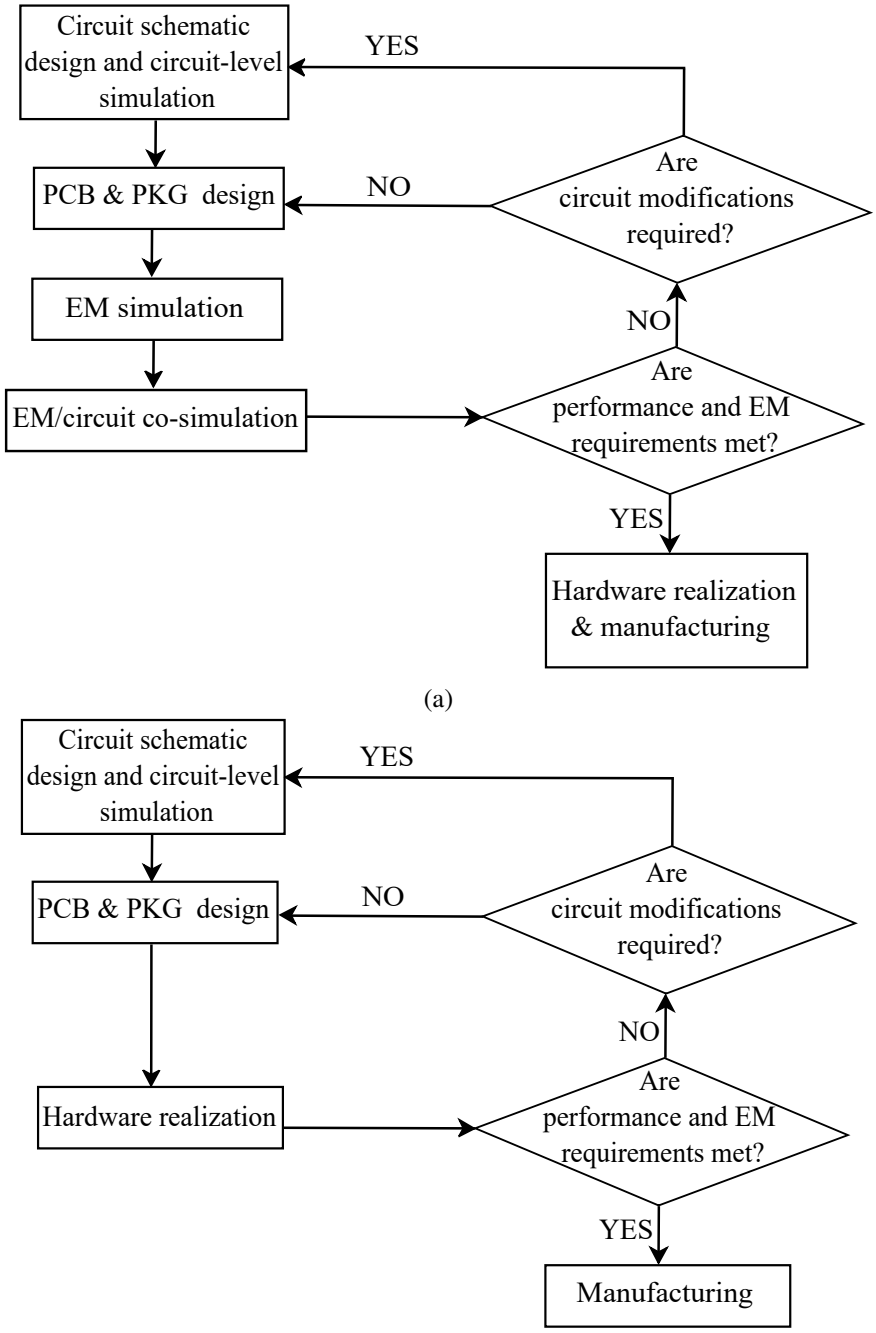


Fig. 1.13 Comparison of the workflows from design to hardware manufacturing with (a) and without (b) EM simulations.

The advantages of integrating EM simulations into the design process can be illustrated by comparing the two workflows shown in Fig. 1.13, which describe

the development process from the initial design to hardware realization and manufacturing. In the workflow incorporating EM simulations, Fig. 1.13(a), the design can be iteratively refined at the circuit and physical levels, through modifications to the circuit schematic and to the PCB and package layout, before proceeding to hardware realization. The compliance of the resulting design with the required performance and EM specifications can therefore be assessed through simulation, reducing the need for repeated hardware iterations. In contrast, when EM simulations are not included, as shown in Fig. 1.13(b), verification of the final design requires hardware realization before its compliance with the required specifications can be assessed. Any subsequent modification may therefore require a new hardware iteration, resulting in increased development time and cost.

Overall, the comparison highlights how the integration of EM simulations into the design process can support a more efficient development methodology, allowing electromagnetic aspects to be considered as an integral part of the design rather than as a verification step performed only after hardware realization.

Chapter 2

EMI Passive filter for DC-DC converter

The results presented in this chapter are adapted from articles P1 that is the direct outcome of the analysis presented herein. This work was developed within the framework of a joint research collaboration with Francesco Gabriele, Ph.D. graduate at Politecnico di Torino, and Amirali Hosseini, Ph.D student at Università di Pavia.

This chapter addresses the synthesis of an LC EMI input filter, which represents the most conventional and widely adopted configuration for Buck converters. Owing to its structural simplicity and well-understood behavior, the LC topology provides a suitable basis for the systematic development of EMI mitigation strategies, while allowing straightforward extension of the proposed methodology to more complex filter topologies. A comprehensive design flow is presented, detailing all the relevant steps required to achieve effective conducted-emission attenuation while ensuring compatibility with impedance-based stability constraints. Particular emphasis is placed on the synthesis of the damping network, whose role is crucial in controlling resonant phenomena and preserving the desired frequency-domain characteristics of the filter–converter system.

Subsequently, the analysis is extended to DC–DC converters operating under the Quasi-Square-Wave Zero-Voltage-Switching (QSW-ZVS) technique. In this context, the converter dynamics are revisited and new expressions fulfilling the EET conditions are derived, enabling an optimal filter and damping network synthesis

under soft-switching operation. The resulting damping solutions are then systematically compared with those obtained for conventional hard-switched converters, highlighting the impact of the operating mode on impedance characteristics and filter parameter selection.

2.1 Design of passive filter

This section focuses on the analytical design methodology of the DM stage of the EMI input filter. The discussion aims at establishing a clear relationship between the spectral characteristics of the noise generated by the converter, the regulatory emission constraints, and the resulting requirements imposed on the passive filter components. Starting from the identification of the dominant spectral components of the input noise, the design procedure proceeds by determining the attenuation that the filter must provide at the relevant frequencies of interest. This required attenuation profile constitutes the primary design constraint and directly drives the dimensioning of the passive components. In this framework, regulatory emission limits are effectively translated into explicit electrical specifications, which can then be systematically addressed through circuit-level synthesis. In this way, a systematic design flow for the passive filter is established, ensuring compliance of the converter with the applicable standard limits. At the same time, this methodology guarantees predictability of the overall EM performance and facilitates subsequent analyses of system stability and dynamic interactions between the converter and the filter.

The starting point of the DM filter synthesis is the quantitative determination of the attenuation required to ensure compliance with conducted emission regulations. From a design perspective, this step is essential, as it translates regulatory constraints—typically expressed in terms of maximum allowable noise levels—into explicit electrical requirements that the filter must satisfy. The required DM attenuation can be formulated as

$$A_{DM}[\mathrm{dB}] = A_{DM,\mathrm{nofilter}}[\mathrm{dB}\,\mu\mathrm{V}] - A_{\mathrm{std}}[\mathrm{dB}\,\mu\mathrm{V}] + m[\mathrm{dB}\,\mu\mathrm{V}] \tag{2.1}$$

where $A_{DM,\mathrm{nofilter}}$ represents the maximum amplitude of the differential-mode noise voltage at the converter input in the absence of any filtering action. This quantity

can be obtained either from direct measurements, circuit-level simulations, or analytical estimations. The term A_{std} denotes the limit imposed by the applicable EMC standard, while m is a design safety margin introduced to account for modeling uncertainties, component tolerances, and deviations between idealized assumptions and experimental conditions. In practical designs, this margin typically ranges between 3–6 dBμV [19].

In switching converters, the most critical contribution is associated with the first significant harmonic of the input current. Under standard operating conditions, this harmonic coincides with the switching fundamental. However, if the switching frequency lies below the lower boundary of the conducted emission band (150 kHz), the dominant spectral component shifts to the second or higher-order harmonics that fall within the regulated frequency range.

For a buck converter operating in continuous conduction mode, the DM input current waveform, i_{in} in Fig. 1.1, can be expressed through its Fourier series expansion as

$$i_{\text{in}}(t) = I_{\text{L}_f} D + \sum_{n=1}^{\infty} \frac{2I_{\text{L}_f}}{n\pi} \sin(n\pi D) \cos(n\omega t) \tag{2.2}$$

where I_{L_f} denotes the cycle-average value of the inductor current i_{L_f} in steady state and D is the duty cycle of the converter.

The magnitude of the dominant harmonic component is directly obtained from the Fourier series and constitutes the primary contributor to the DM conducted noise. To estimate the resulting noise voltage at the converter input terminals, this current harmonic is multiplied by the impedance presented by the input capacitance C_{in} at the corresponding frequency. The resulting attenuation requirement becomes

$$A_{DM}[\text{dB}] = 20\log\left(\frac{I_{\text{L}}}{\pi f_s C_{in}} \cdot \frac{\sin(\pi D)}{\pi} \cdot \frac{1}{\mu\text{V}}\right) - A_{\text{std}}[\text{dB}\,\mu\text{V}] + m[\text{dB}\,\mu\text{V}] \tag{2.3}$$

This formulation establishes a direct and quantitative relationship between the converter operating conditions, and the applicable EMC requirements, thereby providing an explicit estimate of the target minimum attenuation of the input filter to ensure regulatory compliance.

The attenuation requirement previously derived provides a quantitative target that the input filter must satisfy at the frequencies responsible for DM conducted emissions, notably at the switching frequency. Once the required attenuation A_{DM} has been determined, the appropriate passive filter topology and its corresponding component values must be selected, in order to meet the prescribed frequency-domain constraint.

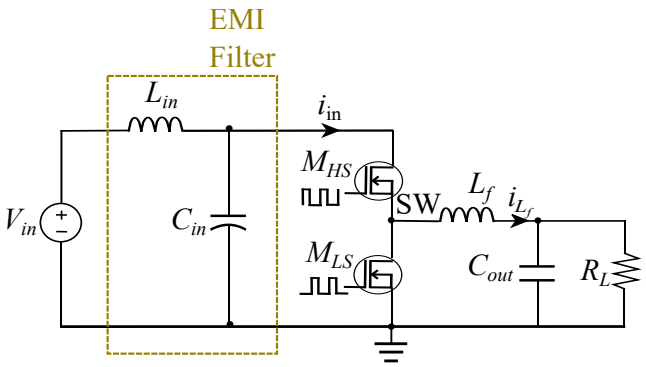


Fig. 2.1 System of DC-DC converter and input EMI LC filter.

Among the available passive solutions, the LC low-pass filter, represented in Fig. 2.1, is the most commonly adopted configuration for DM EMI mitigation in DC-DC converters. This choice is motivated by its structural simplicity. It is worth noting that the same design considerations and analytical approach can be straightforwardly extended to other passive topologies, such as the π-filter. The LC configuration therefore provides a convenient and general starting point for filter synthesis, while preserving the validity of the analysis for more complex filter structures.

This filter is characterized by unity gain in the low-frequency region and an asymptotic attenuation of 40 dB/decade beyond its cutoff frequency. Due to the absence of dissipative elements, this configuration exhibits a resonant peak at its natural frequency. The LC filter topology and the corresponding ideal attenuation profile are shown in Fig. 1.10(a) and Fig. 1.11, respectively. The cutoff frequency of the filter, which coincides with the resonant frequency in the ideal lossless case, is given by

$$f_c = \frac{1}{2\pi\sqrt{L_{in}C_{in}}}. \tag{2.4}$$

Considering that the dominant contribution to DM conducted emissions occurs at the switching frequency f_{sw}, the filter must be designed to provide the required attenuation primarily at this component. Accordingly, the attenuation at the switching frequency can be considered equal to

$$A_{DM} = \left(\frac{f_{sw}}{f_c} \right)^2 . \tag{2.5}$$

By inverting Eq. (2.5) and expressing the attenuation in decibels, the filter cutoff frequency must be selected such that the following condition is satisfied:

$$f_c = \frac{f_{sw}}{10^{A_{DM}[\mathrm{dB}]/40}} . \tag{2.6}$$

Once the cutoff frequency has been determined, the individual values of the inductance and capacitance can then be selected.

In order to analyze the interaction between a switching DC-DC converter and its input power-line filter, it is instructive to begin with an idealized yet insightful operating scenario. Let us consider a switching regulator capable of perfectly compensating any variation in the input voltage. Under this assumption, the output voltage remains strictly constant and unaffected by disturbances originating from the supply side.

For a fixed load condition, a constant output voltage directly implies constant output power. In an ideal lossless converter, this constraint extends to the input port as well, such that the average input power remains invariant with respect to input voltage variations. Consequently, when the input voltage increases, the control mechanism governing the pulse-width modulation reduces the duty ratio of the main switch in order to preserve the regulated output voltage. This adjustment results in a proportional reduction of the average input current.

The resulting inverse relationship between input voltage and input current leads to a fundamental property of switching regulators, when observed through an averaged, low-frequency perspective, the converter behaves as an element exhibiting a negative incremental input resistance. Specifically, an increase in input voltage produces a decrease in the average input current, and vice versa. Provided that the frequency

range of interest is sufficiently lower than the switching frequency, the averaged model accurately captures the relevant system behavior.

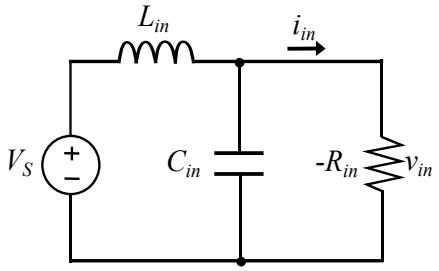


Fig. 2.2 Low-frequency small-signal model of the LC input filter with the switching regulator represented as a negative incremental resistance load.

This characteristic can be formally derived by expressing the input voltage v as a function of the average input current $\bar{i}$ under constant power conditions, obtaining

$$v = \frac{P}{\bar{i}}. \tag{2.7}$$

The incremental input resistance is then defined as

$$\frac{\partial v}{\partial \bar{i}} = \frac{\partial}{\partial \bar{i}}\left(\frac{P}{\bar{i}}\right) = -\frac{P}{\bar{i}^2} = -\frac{v^2}{P} = -R_{in}. \tag{2.8}$$

The combined system consisting of the input filter and the switching regulator, represented by its negative incremental input resistance model, is depicted in Fig. 2.2.

The negative sign explicitly indicates that the incremental resistance associated with the converter input port assumes negative values. This model is inherently nonlinear, as the effective resistance depends on the operating point through the input voltage or current. However, when the analysis is restricted to small perturbations around a given steady-state operating condition, the input resistance can be approximated as constant, allowing the system to be treated as linear.

When such a negative incremental resistance is combined with a simple LC input filter, the resulting small-signal system may exhibit unstable dynamics. In the linearized operating region, the characteristic polynomial of the combined system can be expressed as

$$s^2 - \frac{s}{R_{in}C_{in}} + \frac{1}{L_{in}C_{in}}. \tag{2.9}$$

Due to the negative value of R_{in}, the coefficient of the first-order term becomes positive, which corresponds in the time domain to an exponentially growing response. This behavior indicates an unbounded solution and, therefore, instability. The most critical condition occurs when the magnitude of the negative input resistance is minimized, which corresponds to minimum input voltage.

In practice, no switching regulator is truly lossless. Nevertheless, modern converters are characterized by very high efficiencies, such that the constant-power behavior associated with the load is often dominant with respect to internal losses. As a result, the destabilizing effect associated with negative incremental input resistance remains a significant design concern. Despite this theoretical prediction, in some case DC-DC converters equipped with simple LC input filters operate successfully. Several factors contribute to this apparent discrepancy between theory and practice. First, parasitic resistances associated with inductors, capacitors, interconnections, and supply lines may provide sufficient damping to suppress oscillations. Secondly, in applications where only high-frequency interference components well above the converter control bandwidth are of concern, an LC filter whose resonant frequency lies outside the region where the behavior of the regulator act as a negative input resistance may be adequate. Finally, the control bandwidth of the regulator may be intentionally limited so that its effective gain-bandwidth product remains below the resonant frequency of the input filter.

However, these mitigating factors are not generally applicable to high performance converters. Systems supplying dynamically varying loads, such as microprocessors or power amplifiers, require wide control bandwidths to ensure fast transient response. In such cases, the frequency range over which the converter exhibits negative input impedance may overlap with the resonance of the input filter, particularly when advanced compensation techniques or input-voltage feedforward schemes are employed. Under these conditions, the interaction between the regulator and the input filter becomes critical and cannot be neglected.

For this reason, the following analysis concentrates on DC–DC converters operating under conditions in which the interaction between the input filter and the converter cannot be assumed inherently stable, as this configuration represents the

most general and commonly encountered operating condition in modern converter designs.

A systematic design methodology is required to determine the minimum filter component values that ensure sufficient attenuation of switching-frequency conducted emissions, without introducing unacceptable degradation in stability or dynamic performance.

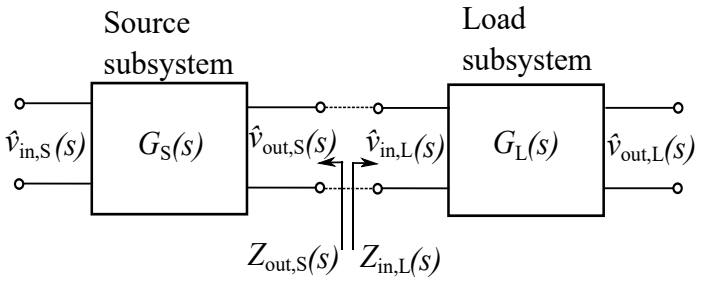


Fig. 2.3 Interconnection of two stable and independent subsystems in cascade.

The stability of a system obtained by cascading two individually stable subsystems can be analyzed by examining the interaction mechanism between them. The influence of this interaction on the overall system dynamics is captured by the quantity referred to as loop gain, defined as

$$T_M(s) = \frac{Z_{\text{out,S}}(s)}{Z_{\text{in,L}}(s)}. \tag{2.10}$$

Here, $Z_{\text{out,S}}(s)$ denotes the output impedance of the upstream subsystem, while $Z_{\text{in,L}}(s)$ represents the input impedance of the downstream subsystem.

The minor-loop gain provides an indication of the dynamic interaction between the two subsystems as mediated by their terminal impedances.

Let $G_S(s)$ and $G_L(s)$ denote the small-signal transfer functions of the source and load subsystems, respectively, as shown in Fig. 2.3, under the assumption that each subsystem is internally stable when considered separately. The small-signal transfer function of the cascaded system can then be expressed as

$$\frac{\hat{v}_{\text{out,L}}(s)}{\hat{v}_{\text{in,S}}(s)} = G_S(s)\,G_L(s)\,\frac{1}{1+T_M(s)}. \tag{2.11}$$

This expression highlights that all effects of the interconnection between the two subsystems are embedded in the term $1/(1+T_M(s))$. Consequently, even if both subsystems are stable on a stand-alone basis, the stability of the interconnected system is governed by the frequency-domain properties of the minor-loop gain.

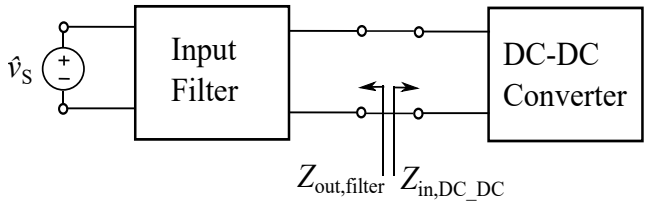


Fig. 2.4 Interconnection of two stable and independent subsystems in cascade.

When this general formulation is applied to a DC-DC converter preceded by an input EMI filter, the source side subsystem corresponds to the input filter, while the load side subsystem is represented by the converter itself, as shown in Fig.2.4. In this case, the minor-loop gain associated with the filter-converter interaction is given by

$$T_M(s) = \frac{Z_{\text{out,filter}}(s)}{Z_{\text{in, DC-DC}}(s)}, \tag{2.12}$$

where $Z_{\text{out,filter}}$ is the output impedance of the EMI filter and $Z_{\text{in, DC-DC}}$ the closed-loop input impedance of the converter

The stability of the combined system can therefore be assessed by applying the Nyquist criterion to the minor-loop gain $T_M(s)$. Oscillatory behavior occurs under the following condition:

$$\left|\frac{Z_{\text{out, filter}}(j\omega)}{Z_{\text{in, DC-DC}}(j\omega)}\right| = 1, \qquad \angle\left(\frac{Z_{\text{out, filter}}(j\omega)}{Z_{\text{in, DC-DC}}(j\omega)}\right) = -180^\circ. \tag{2.13}$$

where ω correspond to the angular frequency.

This condition shows that instability cannot be attributed to the presence of a resonant input filter or to the negative incremental input resistance of the converter when considered in isolation. Instead, it arises from their combined frequency-domain interaction.

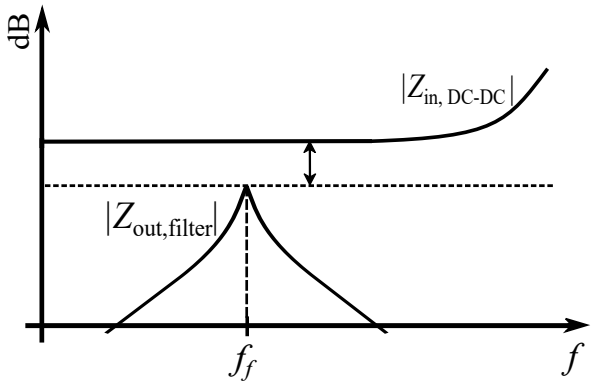


Fig. 2.5 Conservative stability condition ensuring that the output impedance of the input filter $Z_{\text{out,filter}}$ remains below the closed-loop input impedance of the converter $Z_{\text{in,DC-DC}}$.

Therefore, a conservative stability condition, as depicted in Fig. 2.5, is obtained by imposing that the magnitude of the input filter impedance be significantly smaller than the magnitude of the converter input impedance across the frequency range of interest:

$$|Z_{\text{out, filter}}(j\omega)| \ll |Z_{\text{in, DC-DC}}(j\omega)|, \qquad \forall\, \omega. \tag{2.14}$$

When this condition is satisfied, the minor-loop gain remains well below unity, and the correction factor $1/(1+T_M(s))$ has a negligible influence on the dynamics of the cascaded system. From a physical standpoint, this condition implies that the input filter remains weakly coupled to the converter dynamics, so that it does not supply sufficient energy to excite resonant modes or to perturb the regulated behavior of the converter. Under these circumstances, the filter can be regarded as a passive element whose presence does not alter the intrinsic stability properties of the DC–DC converter. The resulting criterion therefore constitutes a practical guideline for the design of input EMI filters intended for high-performance DC–DC converter applications.

While stability represents a fundamental requirement, the introduction of an input EMI filter also alters the dynamic characteristics of the DC–DC converter and can adversely affect closed-loop performance. The presence of the filter modifies the small-signal transfer characteristics of the converter by introducing additional dynamic elements at its input port. It is therefore necessary to adopt an analytical approach to quantify how the inclusion of the input filter modifies the converter

transfer functions and to identify the conditions under which these modifications remain negligible.

For this purpose, the Extra Element Theorem (EET) [20, 21] is employed to rigorously account for the effect of the added element. The theorem enables the inclusion of this circuit element, referred to as the extra element, into a known transfer function without requiring a complete re-derivation of the system model.

Consider a system for which a small-signal transfer function $G(s)$ is known under a reference condition in which the extra element is absent. The reference transfer function is denoted as

$$G(s)\big|_{Z\to 0}, \tag{2.15}$$

where $Z \to 0$ indicates that the port where the extra element will be connected is short-circuited. This reference system represents the converter dynamics without the influence of the input filter.

When an element with impedance $Z(s)$ is connected at the designated port, the modified transfer function becomes

$$G(s) = G(s)\big|_{Z\to 0} \left(\frac{1 + \frac{Z(s)}{Z_n(s)}}{1 + \frac{Z(s)}{Z_d(s)}} \right). \tag{2.16}$$

The multiplicative correction factor fully captures the effect of the added element on the system dynamics. The quantities $Z_n(s)$ and $Z_d(s)$, referred to as the null-condition impedance and the driving-point impedance, respectively, depend only on the original system and on the way the extra element is connected.

- The driving-point impedance $Z_d(s)$ is obtained as the impedance seen at the connection port when the independent input excitation is set to zero. Physically, it represents the impedance seen by the extra element when the system is unexcited. In controlled converters, this impedance depends on the operating point and control action, and reflects how the converter loads the added element.

- The null-condition impedance $Z_n(s)$ is defined as the impedance seen at the same port when the output variable is constrained to zero. In practice, this

corresponds to an ideal feedback condition in which the control system suppresses any variation of the output. Under this assumption, $Z_N(s)$ characterizes the converter input behavior under perfectly regulated output conditions.

The structure of the EET correction factor reveals two distinct mechanisms. The denominator term, involving $Z_d(s)$, accounts for the loading effect of the extra element on the system. The numerator term, involving $Z_n(s)$, describes how the extra element affects the controlled behavior of the system.

When the magnitude of the added impedance $Z(s)$ is small compared to both $Z_n(s)$ and $Z_d(s)$ over the frequency range of interest, the correction factor approaches unity, and the original transfer function is only weakly perturbed.

In the case of an EMI input filter, the extra element corresponds to the filter output impedance $Z_{\text{out,filter}}$. To ensure that the control-to-output transfer function is not significantly altered, the following conditions must be satisfied:

$$|Z_{\text{out,filter}}(j\omega)| \ll |Z_n(j\omega)|, \qquad |Z_{\text{out,filter}}(j\omega)| \ll |Z_d(j\omega)|. \tag{2.17}$$

These inequalities define upper bounds on the allowable filter output impedance and provide explicit design constraints.

A similar condition applies to the preservation of the converter output impedance. Defining $Z_e(s)$ as the input impedance of the converter evaluated under short-circuited output conditions, the following requirement must hold:

$$|Z_{\text{out,filter}}| \ll |Z_e(j\omega)|. \tag{2.18}$$

Consequently, by applying the general formulation of $G(s)$ to the main small-signal characteristics of the buck converter, namely the control-to-output transfer function $G_{vc}(s)$, the input-to-output transfer function $G_{vg}(s)$, and the output impedance $Z_{\text{out}}(s)$, it follows that, provided the previously derived conditions (2.17) and (2.18) are satisfied, these characteristics remain only marginally affected by the presence of the input filter. As a result, the intrinsic dynamic performance of the converter is effectively preserved.

In practical implementations, the undamped LC input filter exhibits a resonant behavior whose interaction with the converter may lead to instability and violate the conditions of the EET required to ensure negligible impact on system performance. For this reason, the introduction of damping is an essential design step to ensure that the filter behaves as a well-controlled passive subsystem while preserving the validity of the impedance-based design inequalities.

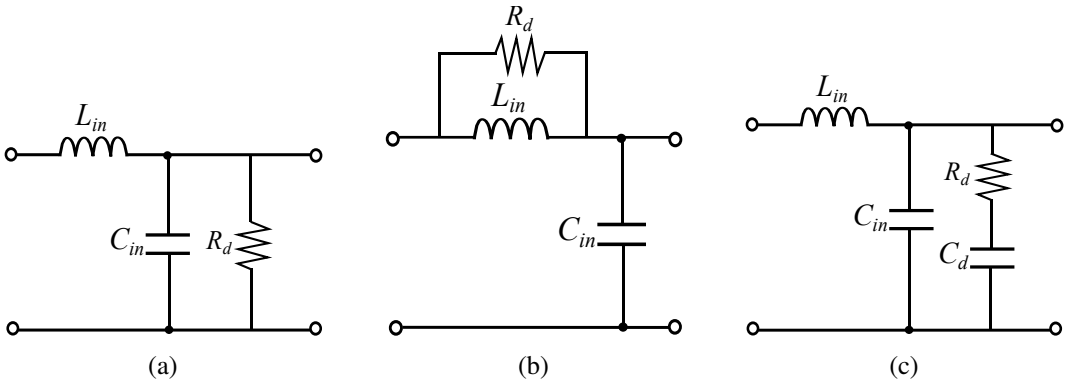


Fig. 2.6 Different damping strategies on LC input filter, with (a) a single resistor in parallel to filter capacitance, (b) a single resistor in parallel to filter inductance, and (c) a DC blocking capacitor in series to R_d.

Several damping strategies can be adopted to achieve this objective. A straightforward approach to suppressing the resonance of the LC input filter consists in introducing a damping resistor R_d in parallel with the filter capacitor C_{in}, as illustrated in Fig. 2.6(a). In this configuration, the resonant peak of the filter impedance is effectively constrained by the resistive element, since the maximum value of the filter output impedance is limited by the damping resistance itself. As a consequence, compliance with the impedance-based stability conditions requires that this maximum impedance remain sufficiently lower than both the null-condition and driving-point impedance asymptotes of the converter. This requirement can be expressed in the form [22]

$$R_d \ll |Z_n(j\omega)|, \qquad R_d \ll |Z_d(j\omega)|. \tag{2.19}$$

For the buck converter under consideration, the low-frequency asymptotes of $Z_n(j\omega)$ and $Z_d(j\omega)$ are both proportional to the load resistance reflected at the

converter input, which leads to the conservative design constraint

$$R_d \ll \frac{R_L}{D^2}. \tag{2.20}$$

Although this condition ensures effective limitation of the resonance peak, it introduces a significant drawback. Since the damping resistor is connected directly across the filter capacitor, it is continuously subjected to the DC input voltage V_S. Consequently, the resistor dissipates a power proportional to V_S^2/R_d, which increases rapidly as smaller resistance values are selected to satisfy the impedance constraints. For the values of R_d required to achieve adequate damping, the resulting power dissipation may exceed the power delivered to the load, making this solution impractical for efficient power converter designs.

To overcome the issue of excessive DC power loss, an alternative configuration places the damping resistor R_d in parallel with the filter inductor L_{in}, as shown in Fig. 2.6(b). In this structure, the steady-state voltage across the inductor is ideally zero, and therefore no DC power is dissipated in the damping resistance. While this solution eliminates DC losses, it introduces a different limitation. The resulting filter transfer function exhibits a zero at high frequency, which modifies the asymptotic attenuation behavior of the filter. In particular, the high-frequency roll-off is reduced from $-40\,\mathrm{dB/dec}$ to $-20\,\mathrm{dB/dec}$, effectively degrading the second-order filtering action provided by the LC network.

A more effective solution is obtained by introducing a DC-blocking capacitor C_d in series with the damping resistor R_d, and connecting the resulting branch in parallel with the filter capacitor C_{in}, as represented in Fig. 2.6(c). In this configuration, DC current is effectively prevented from flowing through the damping resistor, thereby eliminating DC power dissipation. At frequencies near the LC resonance, the impedance of the series R_d–C_d branch is dominated by the resistive component, provided that C_d is sufficiently large. Under this condition, the intrinsic second-order attenuation characteristic of the LC filter is preserved, together with its intended frequency-domain behavior. This approach therefore combines effective resonance damping with minimal impact on efficiency and filtering performance, and represents a practical compromise for EMI input filter design. The design problem is therefore reduced to the appropriate selection of the damping resistance R_d and the blocking

capacitance C_d. In practical EMI filter design, a commonly adopted design guideline is given by

$$R_d \approx \sqrt{\frac{L_{in}}{C_{in}}}, \tag{2.21}$$

and

$$C_d > 5C_{in}. \tag{2.22}$$

These relationships ensure that the damping branch behaves predominantly as a resistive element around resonance, thereby suppressing impedance peaking while preserving the second-order attenuation characteristics of the LC filter.

Although these criteria provide a straightforward and practical starting point, they do not explicitly guarantee an optimal selection of the component values. In particular, the resulting design may require excessively large values of the blocking capacitance C_d, leading to undesired penalties in terms of component size, cost, and implementation feasibility. To overcome these limitations and determine the optimal values of the damping network components C_d and R_d, an impedance-based optimization approach originally proposed by Middlebrook is adopted [23]. Thereby, the optimal damping condition is obtained by directly minimizing the peak of the filter output impedance $Z_{\text{out,filter}}(s)$.

The procedure is based on evaluating the sensitivity of the output impedance magnitude with respect to the filter quality factor. By enforcing a zero-sensitivity condition, the frequency at which the maximum impedance peaking occurs is identified as

$$f_{\text{opt}} = f_f \sqrt{\frac{2}{2+n}}, \tag{2.23}$$

where f_f, shown in Fig 2.5, denotes the natural resonant frequency of the undamped LC section equal to $f_f = \frac{1}{2\pi\sqrt{L_{\text{in}}C_{\text{in}}}}$, and n represents the ratio between the damping capacitance and the input filter capacitance. The output impedance is then evaluated at the corresponding angular frequency $\omega_{\text{opt}} = 2\pi f_{\text{opt}}$, and minimized with respect to the quality factor. This optimization yields closed-form expressions for the optimal filter quality factor Q_{opt} and for the parameter n in the considered operating

conditions [24, 25]:

$$n = \frac{R_{0f}\left(R_{0f} + \sqrt{R_{0f}^2 + 4(Z_{\text{target}})^2}\right)}{(Z_{\text{target}})^2}, \tag{2.24}$$

$$Q_{\text{opt}} = \sqrt{\frac{(4+3n)(2+n)}{2n^2(4+n)}}, \tag{2.25}$$

where, $R_{0f} = \sqrt{L_{\text{in}}/C_{\text{in}}}$, while the quantity Z_{target} defines the target impedance, which sets an upper bound on the allowable value of the filter output impedance, ensuring compliance with impedance-based stability constraints.

Finally, once the optimal values of n and Q_{opt} have been determined, the damping network components are obtained as

$$C_d = nC_{in}, \qquad R_d = R_{0f}Q_{\text{opt}}. \tag{2.26}$$

This optimized approach ensures a minimization of the peak filter output impedance, thereby enhancing robustness with respect to both EMI compliance and stability requirements, while avoiding unnecessary oversizing of the damping components.

The analysis presented in this section shows that the design of the EMI input filter for a buck converter requires a unified approach that simultaneously addresses conducted emission attenuation, impedance-based stability, and preservation of dynamic performance. By enforcing appropriate impedance constraints and employing analytical criteria, stable operation can be ensured while retaining the fundamental small-signal characteristics of the converter. Thus, the introduction of damping emerges as a fundamental design requirement. By ensuring controlled resonant behavior of the input filter, adequate damping simultaneously preserves the dynamic performance of the converter, and guarantees stable operation of the overall converter–filter system.

2.2 Optimization of damping element for DC-DC converter with ZVS

The complete LC input filter design flow developed in the previous sections is now applied to DC–DC converters employing the Quasi-Square-Wave Zero-Voltage-Switching (QSW-ZVS) technique. The resulting filter structure and damping requirements are systematically derived and compared with those obtained for conventional hard-switched converters, with the aim of highlighting the impact of soft-switching operation on the selection of the damping elements and on the overall filter behavior.

Conventional hard-switching DC–DC converters are widely adopted owing to their architectural simplicity, straightforward design procedures, and cost effectiveness. However, their operating principle is inherently associated with significant switching losses, which limit achievable power conversion efficiency. To address this limitation, a variety of soft-switching techniques have been developed and are now well established in DC–DC converter applications as effective means for reducing switching losses, improving overall efficiency, and shaping the switching waveforms [26]. Among these techniques, QSW-ZVS enables to achieve ZVS without introducing additional circuit elements in the power stage of the converter [27, 28]. This behavior is achieved by exploiting the intrinsic parasitic capacitances of the switching devices together with the main filter inductor already present in conventional hard-switched topologies [29–31]. As a result, QSW-ZVS provides a minimal-overhead solution for loss reduction while preserving the fundamental structure of the converter. An additional and non-negligible benefit of soft-switching operation is the reduction of EMI generated by the converter. By lowering the effective voltage and current slew rates during switching transitions, QSW-ZVS mitigates the high dv/dt and di/dt components that are characteristic of traditional hard-switched converters, leading to reduced conducted emission levels [32, 33].

Nevertheless, the introduction of a ZVS mechanism alters the converter dynamic behavior and modifies its averaged small-signal characteristics [34, 35]. Accordingly, in this chapter, the enhanced averaged small-signal model proposed in [36] is adopted to capture the impact of the QSW-ZVS operating mode on the interaction between the converter and the EMI input filter. Building upon this model, the

implications of soft-switching operation on filter synthesis, damping design, and impedance-based stability constraints are investigated and compared with those of conventional hard-switched DC–DC converters.

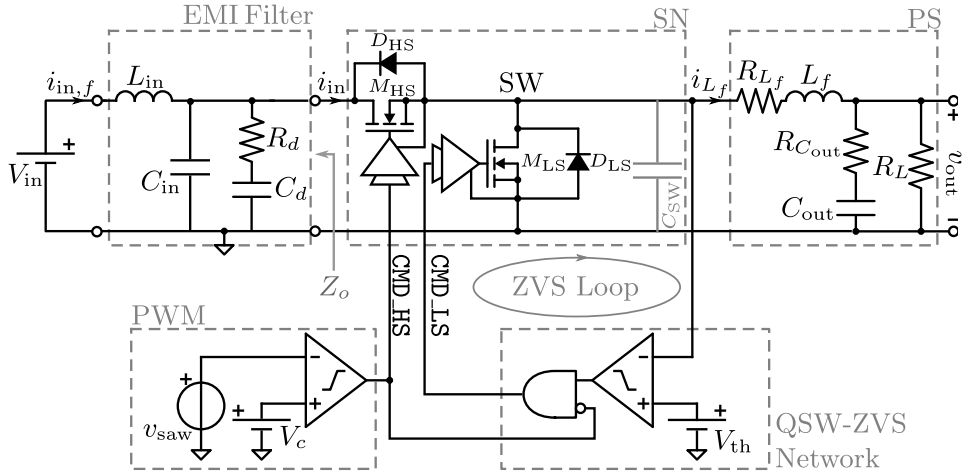


Fig. 2.7 Architecture of the QSW-ZVS DC-DC buck converter with EMI filter considered in this paper.

Averaged small-signal models are of paramount importance in the analysis and design of switching DC-DC converters. They permit to assess the dynamic behavior of the converters by modeling them as linear time-invariant systems. In the design of passive EMI filters, averaged small-signal models allow to evaluate the interaction between the converter and the EMI filter when they are interconnected. In practice, this requires to compute key TFs from the complete small-signal model of the converter [37–39].

The QSW-ZVS DC-DC Buck converter considered is shown in Fig. 2.7. The complete scheme includes the Power Stage (PS), the Switching Network (SN), the Pulse-Width Modulator (PWM) stage, the QSW-ZVS network and the passive EMI filter. The SN is implemented as a synchronous half-bridge comprising the Low-Side LS and High-Side (HS) power MOSFETs, i.e., M_{LS} and M_{HS}, together with their body diodes, i.e., D_{LS} and D_{HS}. The ON-state resistances of the LS and HS power MOSFETs are $R_{\mathrm{LS_{on}}}$ and $R_{\mathrm{HS_{on}}}$, respectively. The overall parasitic capacitance on the `SW` node is modeled with a linear capacitor C_{SW}. The SN is connected to the PS of the converter. The latter includes the inductor L_f and the output capacitor C_{out}, along with their Equivalent Series Resistances (ESRs), i.e., R_{L_f} and $R_{C_{\mathrm{out}}}$, respectively. A

fixed resistor R_L is connected to the output port of the converter to set the static load current level $I_{\text{out}} = V_{\text{out}}/R_L$, where V_{out} is the DC output voltage value. The power MOSFETs M_{LS} and M_{HS} are driven by the sawtooth-based PWM stage and the QSW-ZVS network, that synthesize the logic driving signals `CMD_HS` and `CMD_LS`. The PWM stage compares the sawtooth-voltage v_{saw} and the control voltage V_c, generating `CMD_HS`. The frequency of the signal v_{saw} is equal to $F_{\text{sw}} = 1/T_{\text{sw}}$, while its amplitude is V_{pk}. The QSW-ZVS network senses the voltage on the SW node and compares it with the reference voltage V_{ref} to detect the optimal turn-ON time instant for M_{LS}, thereby implementing a break-before-make mechanism to generate `CMD_LS`.

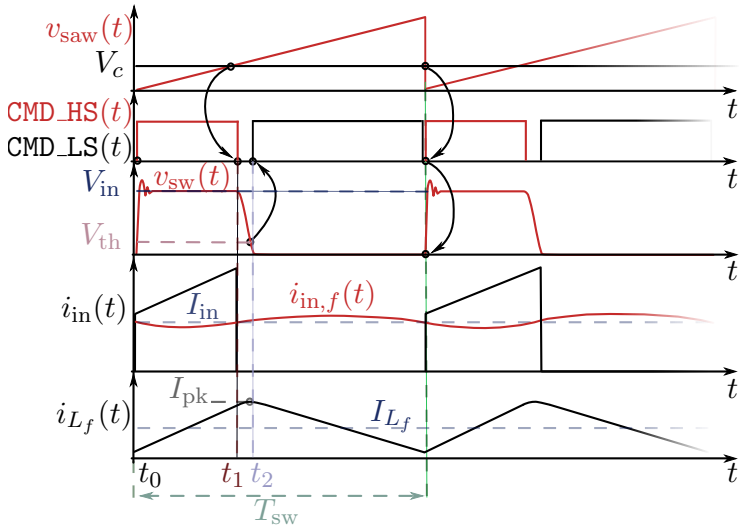


Fig. 2.8 Main voltage and current waveforms in QSW-ZVS operation of the converter in Fig. 2.7.

The operation of the converter in steady-state is shown in Fig. 2.8. At the beginning, i.e., when $t = t_0$, $V_c > v_{\text{saw}}$, `CMD_HS` is asserted and `CMD_LS` is deasserted. In turn, v_{SW} equals to V_{in} and the current flowing through L_f, viz., i_{L_f}, increases. When $t = t_1$, $V_c < v_{\text{saw}}$ and the signal `CMD_HS` becomes de-asserted. The quasi-constant current $i_{L_f} \approx I_{\text{pk}}$ discharges the parasitic capacitance C_{SW}, whose terminal voltage in $t = t_1$ coincides with v_{SW}. An estimate of the current I_{pk} is given by the small-ripple approximation and inductor volt-second balance [39] as

$$I_{\text{pk}} = I_{L_f} + \frac{V_{\text{in}} - V_{\text{out}}}{2L_f} T_{\text{on},0} = I_{L_f} + \frac{V_{\text{in}} - V_{\text{out}}}{2L_f F_{\text{sw}}} D_0, \tag{2.27}$$

where $T_{\text{on},0} = t_1 - t_0$ is the ON time of the driving signal CMD_HS and $D_0 = T_{\text{on},0}/T_{\text{sw}}$ is the correspondent duty-cycle. For $t > t_0$, the voltage v_{SW} starts decreasing, reaching the level $v_{\text{SW}} \approx V_{\text{th}} \ll V_{\text{in}}$ when $t = t_2$. Here, CMD_LS is asserted, thus turning-ON M_{LS} with low drain-source voltage and hence implementing ZVS for the LS MOSFET. Therefore, it should be noted that the action of the QSW-ZVS network is to introduce an adaptive dead-time interval $T_d := t_2 - t_1$ after the HS MOSFET is turned-OFF. The length of T_d is adaptively set based on the converter operating conditions, and an estimate of this interval is obtained by assuming a linear discharge of C_{SW} as $T_d = C_{\text{SW}} {}^{V_{\text{in}}}/_{I_{\text{pk}}}$. The EMI filter prevents that the pulsating input current i_{in} propagates back to the DC input voltage source. Indeed, the filtered current signal $i_{\text{in,f}}$ features a low-amplitude ripple signal superimposed on the DC input current component $I_{\text{in}} = D_0 I_{L_f}$.

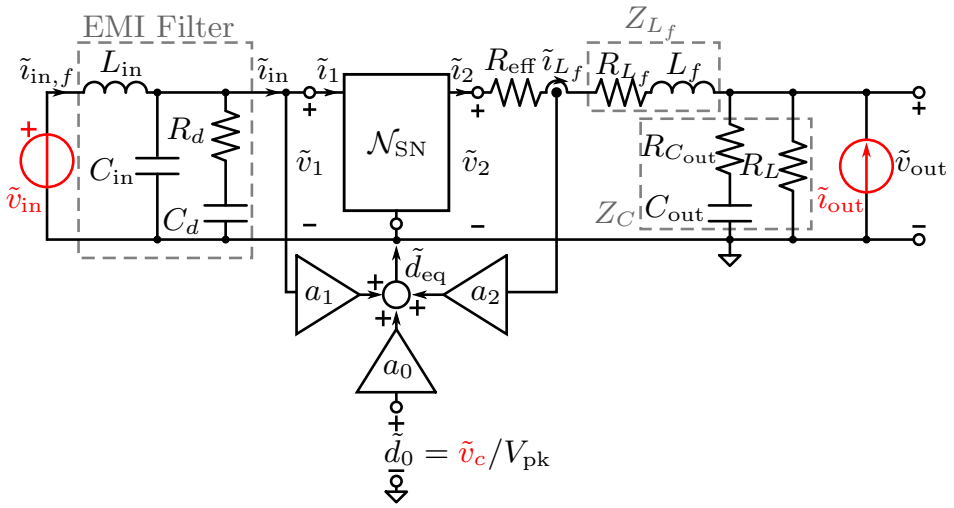


Fig. 2.9 The averaged small-signal model of the considered QSW-ZVS DC-DC Buck converter and the passive EMI filter.

The equivalent averaged small-signal model for converter herein considered is proposed in Fig. 2.9. From an high-level perspective, it embeds the equivalent small-signal model presented in [36], the PWM stage and the EMI filter stage. The correspondence between the small-signal model and the large-signal circuit is evident. The signal $\tilde{v}_{\text{in}}$ represents the line-voltage perturbation, that propagates through the EMI filter. The control voltage perturbation $\tilde{v}_c$ translates into a duty-ratio perturbation $\tilde{d}_0$ through the TF of the PWM stage, i.e., $1/V_{\text{pk}}$. The output current

perturbation $\tilde{\imath}_{\text{out}}$ is applied to the output port of the converter, and it models the load-current variations. The two-port network $\mathscr{N}_{\text{SN}}$ models the behavior of the SN. The relationship between its input and output is derived by applying the standard circuit averaging technique based on the terminal waveforms of the SN shown in Fig. 2.8. At this stage, by neglecting the R_{eff}-induced ohmic losses, this yields

$$\mathscr{N}_{\text{SN}}: \begin{bmatrix} \tilde{v}_2 \\ \tilde{\imath}_1 \end{bmatrix} = \begin{bmatrix} D_{\text{eq}} & 0 \\ 0 & D_0 \end{bmatrix} \begin{bmatrix} \tilde{v}_1 \\ \tilde{\imath}_2 \end{bmatrix} + \underbrace{\begin{bmatrix} V_{\text{in}} & 0 \\ 0 & I_{L_f} \end{bmatrix} \begin{bmatrix} \tilde{d}_{\text{eq}} \\ \tilde{d}_0 \end{bmatrix}}_{\text{Ext. Control}}. \tag{2.28}$$

Then, an equivalent AC-resistance R_{eff} is introduced at the output port of the $\mathscr{N}_{\text{SN}}$ based on [21, 40], as shown in Fig. 2.9. The gain stages a_0, a_1 and a_2 model the effect of the QSW-ZVS network. Their analytical expressions are summarized in Table 2.1, while for additional details on the mathematical derivation process the reader is referred to [36, 39]. Thus, the QSW-ZVS network modulates the external duty-cycle perturbation $\tilde{d}_0$ as

$$\tilde{d}_{\text{eq}} = a_0\,\tilde{d}_0 \; + a_1\,\tilde{v}_1 + a_2\,\tilde{\imath}_{L_f}, \tag{2.29}$$

where $\tilde{v}_1$ is the small-signal voltage perturbation applied at the input port of the converter and $\tilde{\imath}_{L_f}$ is the small-signal variation of the inductor current. Also, it is worth noting that the averaged small-signal model in Fig. 2.9 can be used to cover the scenario in which the QSW-ZVS network is disabled by simply imposing $a_0 = 1$, $a_1 = a_2 = 0$ and replacing D_{eq} with D_0. Here, in fact, $T_d = 0$ and `CMD_LS` is asserted as soon as `CMD_HS` is deasserted. In consequence, $\tilde{d}_{\text{eq}} = \tilde{d}_0$.

To better empathize the impact of the EMI filter on the small-signal dynamics of the converter, an high-level view of the small-signal model shown in Fig. 2.9 is proposed in Fig. 2.10. In the figure, the EMI filter and the small-signal input perturbation $\tilde{v}_{\text{in}}$ shown in Fig. 2.9 are replaced by their Thévenin equivalent. The equivalent voltage source is $H_f \cdot \tilde{v}_{\text{in}}$, where

$$H_f(s) = \frac{\frac{1}{sC_{\text{in}}} \parallel (R_d + \frac{1}{sC_d})}{sL_{\text{in}} + \left(\frac{1}{sC_{\text{in}}} \parallel \left(R_d + \frac{1}{sC_d}\right)\right)}, \tag{2.30}$$

Table 2.1 Parameters and coefficients of the small-signal circuit model in Fig. 2.9.

Parameter	**Expression**
e_0	$V_{\text{in}} - (R_{\text{HS}_{\text{on}}} I_{\text{L}_{\text{f}}} + R_{\text{LS}_{\text{on}}} I_{\text{L}_{\text{f}}})$
D_{eq}	$D_0 + T_d/(2T_{\text{sw}})$
R_{eff}	$R_{\text{HS}_{\text{on}}} D_{\text{eq}} + R_{\text{LS}_{\text{on}}}(1 - D_{\text{eq}})$
a_0	$1 - C_{\text{SW}} V_{\text{in}}(V_{\text{in}} - V_{\text{out}})/(4L_f I_{\text{pk}}^2)$
a_1	$C_{\text{SW}}/(2T_{\text{sw}} I_{\text{pk}})$
a_2	$-C_{\text{SW}} V_{\text{in}}/(2T_{\text{sw}} I_{\text{pk}}^2)$

whilst the equivalent output impedance is computed as

$$Z_o(s) = sL_f \parallel \frac{1}{sC_{\text{in}}} \parallel \left(\frac{1}{sC_d} + R_d\right), \tag{2.31}$$

where s is the complex Laplace variable and $\parallel$ is the parallel operator.

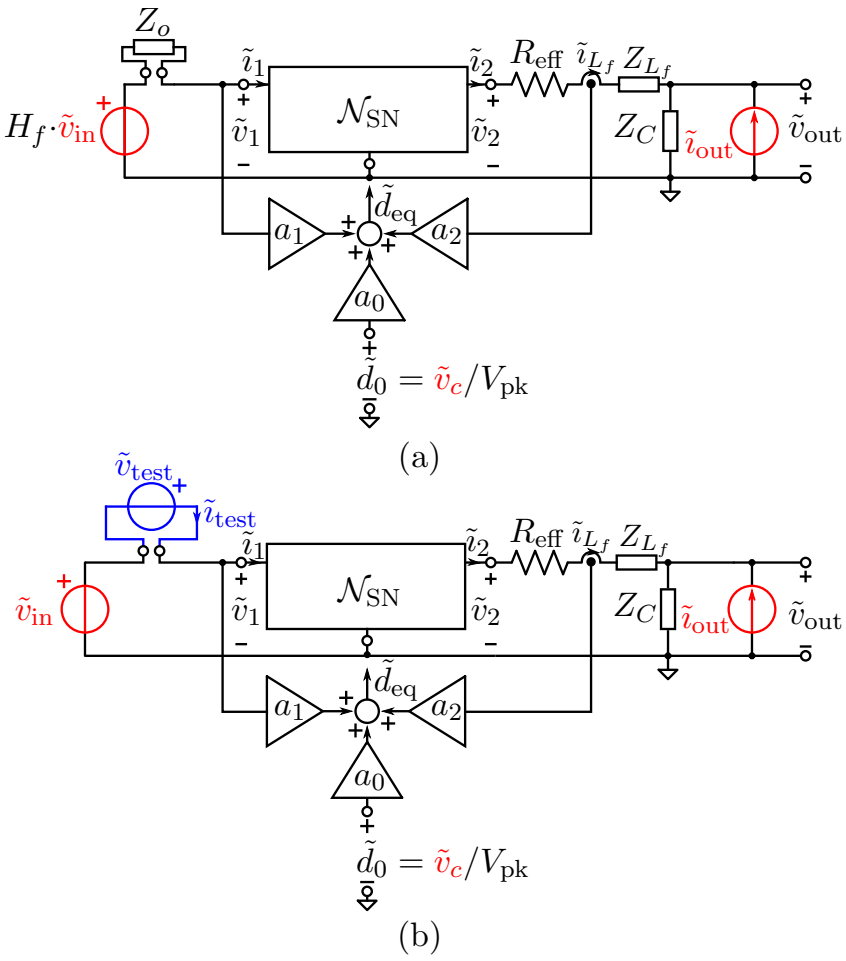


Fig. 2.10 High-level view of the averaged small-signal model shown in Fig. 2.9. (a) The EMI filter is modeled as an extra element in the small-signal representation of Fig. 2.9; (b) reference circuit model adopted for the computation of the impedances in (2.38).

Furthermore, the $\mathcal{N}_{\text{SN}}$ block models the SN. The high-level representation in Fig. 2.10 provides a framework to derive any TF of the converter both when the input EMI filter is introduced/removed and by enabling/disabling the action of the QSW-ZVS network.

In practice, the control-to-output TF $G_{\text{vc}}(s)$, the line-to-output TF $G_{\text{vg}}(s)$, and the output impedance TF $Z_{\text{out}}(s)$ are of major interest for design-oriented purposes. To maintain a clear exposition, we start by deriving these TFs assuming that the EMI filter is not present. This scenario is illustrated in Fig. 2.10, where $Z_o = 0$ and $H_f = 1$ (and thus, $\tilde{v}_1 = \tilde{v}_{\text{in}}$). Also, here we set $\tilde{v}_{\text{test}} = 0$, where $\tilde{v}_{\text{test}}$ is an external voltage excitation whose purpose will be clarified shortly. At this stage, the $\mathcal{N}_{\text{SN}}$ block is

represented by the equivalent circuit model in Fig. 2.9. Through simple algebraic manipulations, the control-to-output TF is derived as

$$G_{\mathrm{vc}}(s)|_{Z_o(s)=0} = \frac{\tilde{v}_{\mathrm{out}}(s)}{\tilde{v}_c(s)} = k_{\mathrm{vc}} \frac{Z_2(s)}{Z_1(s)+Z_2(s)}, \tag{2.32}$$

where k_{vc}, $Z_1(s)$ and $Z_2(s)$ are defined in Table 2.2. Similarly, the line-to-output TF is derived as

$$G_{\mathrm{vg}}(s)|_{Z_o(s)=0} = \frac{\tilde{v}_{\mathrm{out}}(s)}{\tilde{v}_{\mathrm{in}}(s)} = k_{\mathrm{vg}} \frac{Z_2(s)}{Z_1(s)+Z_2(s)}. \tag{2.33}$$

where k_{vg} is defined in Table 2.2. Finally, the output impedance TF is given by

$$Z_{\mathrm{out}}(s)\Big|_{Z_o(s)=0} = \frac{\tilde{v}_{\mathrm{out}}(s)}{\tilde{\imath}_{\mathrm{out}}(s)} = Z_1(s) \parallel Z_2(s). \tag{2.34}$$

Table 2.2 Parameters of the main TFs of the small-signal circuit model in Fig. 2.9.

	Trad	**ZVS**
k_{vc}	e_0/V_{pk}	$a_0 \cdot (e_0/V_{\mathrm{pk}})$
k_{vg}	D_0	$D_{\mathrm{eq}} + a_1 e_0$
$Z_1(s)$	$sL_f + R_{\mathrm{eff}} + R_{L_f}$	$sL_f + R_{\mathrm{eff}} + R_{L_f} - a_2 e_0$
$Z_2(s)$	$\left(\frac{1}{sC_{\mathrm{out}}} + R_{C_{\mathrm{out}}}\right) \parallel R_L$	$\left(\frac{1}{sC_{\mathrm{out}}} + R_{C_{\mathrm{out}}}\right) \parallel R_L$

At this stage, the EET presented in the previous section is now applied to quantitatively assess the effect introduced by the input EMI filter.

Therefore, the main results in (2.32), (2.33), and (2.34) are preserved, with the effect of the EMI filter included in the additional correction factor. The new control-to-output TF of the converter is thus given by

$$G_{\mathrm{vc}}(s) = G_{\mathrm{vc}}(s)|_{Z_o=0} \cdot \frac{1+Z_o(s)/Z_n(s)}{1+Z_o(s)/Z_d(s)}, \tag{2.35}$$

the line-to-output transfer function becomes

$$G_{\mathrm{vg}}(s) = H_f(s) \cdot G_{\mathrm{vg}}(s)|_{Z_o=0} \cdot \frac{1 + Z_o(s)/Z_g(s)}{1 + Z_o(s)/Z_d(s)} \tag{2.36}$$

and the new output impedance in the presence of the filter is expressed as

$$Z_{\mathrm{out}}(s) = Z_{\mathrm{out}}(s)|_{Z_o=0} \cdot \frac{1 + Z_o(s)/Z_e(s)}{1 + Z_o(s)/Z_d(s)}. \tag{2.37}$$

The quantities $Z_d(s)$, $Z_n(s)$, $Z_g(s)$ and $Z_e(s)$ are found as explained in Section 2.1 by measuring impedances at the port where the added circuit element is introduced. Referring to Fig. 2.10, these impedances are measured at the port where Z_o is connected to the rest of the small-signal model and are defined as

$$\begin{aligned} Z_d(s) &= \left.\frac{\tilde{v}_{\mathrm{test}}(s)}{\tilde{\imath}_{\mathrm{test}}(s)}\right|_{\substack{\tilde{d}_0(s)=0 \\ \tilde{v}_{\mathrm{in}}(s)=0 \\ \tilde{\imath}_{\mathrm{out}}(s)=0}}, \quad Z_n(s) = \left.\frac{\tilde{v}_{\mathrm{test}}(s)}{\tilde{\imath}_{\mathrm{test}}(s)}\right|_{\substack{\tilde{v}_{\mathrm{in}}(s)=0 \\ \tilde{\imath}_{\mathrm{out}}(s)=0 \\ \tilde{v}_{\mathrm{out}}(s)\to 0}}, \\ Z_e(s) &= \left.\frac{\tilde{v}_{\mathrm{test}}(s)}{\tilde{\imath}_{\mathrm{test}}(s)}\right|_{\substack{\tilde{v}_{\mathrm{in}}(s)=0 \\ \tilde{d}_0(s)=0 \\ \tilde{v}_{\mathrm{out}}(s)\to 0}} \text{ and } Z_g(s) = \left.\frac{\tilde{v}_{\mathrm{test}}(s)}{\tilde{\imath}_{\mathrm{test}}(s)}\right|_{\substack{\tilde{d}_0(s)=0 \\ \tilde{\imath}_{\mathrm{out}}(s)=0 \\ \tilde{v}_{\mathrm{out}}(s)\to 0}}, \end{aligned} \tag{2.38}$$

where $\tilde{v}_{\mathrm{test}}$ is applied at the Z_o port, while $\tilde{\imath}_{\mathrm{test}}$ is the corresponding current response. The notation $\tilde{v}_{\mathrm{out}} \to 0$ is adopted to indicate that the active input stimulus (i.e., the test voltage $\tilde{v}_{\mathrm{test}}$ and the independent input perturbations $\tilde{d}_0$, $\tilde{\imath}_{\mathrm{out}}$ and $\tilde{v}_{\mathrm{in}}$ for Z_n, Z_e and Z_g, respectively) are tuned so that $\tilde{v}_{\mathrm{out}}$ is null. Based on (2.38), the model in Fig. 2.10 and through simple algebraic manipulations the analytical expressions in Table 2.3 are derived.

Table 2.3 Impedances derived with EET for traditional and QSW-ZVS operation modes.

	Trad	**ZVS**
$Z_d(s)$	$\frac{Z_1^{\text{Trad}}(s)+Z_2^{\text{Trad}}(s)}{D_0^2}$	$\frac{Z_1^{\text{ZVS}}(s)+Z_2^{\text{ZVS}}(s)}{D_0(D_{\text{eq}}+e_0a_1)}$
$Z_e(s)$	$\frac{Z_1^{\text{Trad}}(s)}{D_0^2}$	$\frac{Z_1^{\text{ZVS}}(s)}{D_0(D_{\text{eq}}+e_0a_1)}$
$Z_n(s)$	$-\frac{R_L}{D_0^2}$	$-\frac{e_0a_0}{I_{L_f}(D_{\text{eq}}+e_0a_1)}$
$Z_g(s)$	$\rightarrow +\infty$	$\rightarrow +\infty$

The derived quantities define the maximum allowable impedance levels that the filter output impedance Z_o must not exceed in order to satisfy the EET constraints expressed in (2.17), (2.18). Under these conditions, the introduction of the EMI input filter does not significantly alter the main small-signal transfer functions of the converter. In consequence, they also permit to guarantee closed-loop system stability if the control network is added *a posteriori*. Indeed, practical design criteria for the control network are typically established to achieve adequate stability margins and dynamic performances relying on the main TFs of the converter. Since these TFs are not affected by the presence of the EMI filter, no degradation in performance or stability margins can occur.

From a practical filter design perspective, selecting f_c according to (2.5) leads to a scenario in which the minimum value of $|Z_d(j\omega)|$ constitutes the key design parameter, since under typical operating conditions, it represents the lowest impedance derived from the EET that $Z_o(s)$ must not exceed [41]. In order to comply with these design criteria, $|Z_o(j\omega)|$ needs to be set with a margin m_{dB} typically ranging from 6 dB to 12 dB below the minimum of the EET impedance levels.

Consequently, by focusing on $Z_d(s)$, the expression can also be written in the following form:

$$Z_d(s) = R_0 \frac{\left(1+\frac{s}{\omega_0 Q}+\frac{s^2}{\omega_0^2}\right)}{\left(1+\frac{s}{\omega_1}\right)} \tag{2.39}$$

where the corresponding parameters are derived in Tables 2.4 and 2.5 for both the traditional and QSW-ZVS modes.

Table 2.4 Parameters in the expression of Z_d for traditional operation mode.

Parameter	**Trad**
R_0	$\frac{R_{\mathrm{L}}+R_{\mathrm{L_f}}+R_{\mathrm{eff}}}{D_0^2}$
ω_0	$\sqrt{\frac{R_{\mathrm{eff}}+R_{\mathrm{L_f}}+R_{\mathrm{L}}}{L_{\mathrm{f}}C_{\mathrm{out}}(R_{C_{\mathrm{out}}}+R_{\mathrm{L}})}}$
Q	$\frac{\sqrt{L_{\mathrm{f}}C_{\mathrm{out}}(R_{\mathrm{L}}+R_{C_{\mathrm{out}}})(R_{\mathrm{eff}}+R_{\mathrm{L_f}}+R_{\mathrm{L}})}}{L_{\mathrm{f}}+C_{\mathrm{out}}[R_{\mathrm{L}}(R_{C_{\mathrm{out}}}+R_{\mathrm{L_f}}+R_{\mathrm{eff}})+R_{C_{\mathrm{out}}}(R_{\mathrm{L_f}}+R_{\mathrm{eff}})]}$
ω_1	$\frac{1}{R_{\mathrm{L}}C_{\mathrm{out}}}$

Table 2.5 Parameters in the expression of Z_d for QSW-ZVS operation mode.

Parameter	**ZVS**
R_0	$\frac{R_{\mathrm{L}}+R_{\mathrm{L_f}}+R_{\mathrm{eff}}-e_0a_2}{D_0(D_{\mathrm{eq}}+e_0a_1)}$
ω_0	$\sqrt{\frac{R_{\mathrm{eff}}+R_{\mathrm{L_f}}+R_{\mathrm{L}}-e_0a_2}{L_{\mathrm{f}}C_{\mathrm{out}}(R_{C_{\mathrm{out}}}+R_{\mathrm{L}})}}$
Q	$\frac{\sqrt{L_{\mathrm{f}}C_{\mathrm{out}}(R_{\mathrm{L}}+R_{C_{\mathrm{out}}})(R_{\mathrm{eff}}+R_{\mathrm{L_f}}+R_{\mathrm{L}}-e_0a_2)}}{L_{\mathrm{f}}+C_{\mathrm{out}}[R_{\mathrm{L}}(R_{C_{\mathrm{out}}}+R_{\mathrm{L_f}}+R_{\mathrm{eff}}-e_0a_2)+R_{C_{\mathrm{out}}}(R_{\mathrm{L_f}}+R_{\mathrm{eff}})]}$
ω_1	$\frac{1}{R_{\mathrm{L}}C_{\mathrm{out}}}$

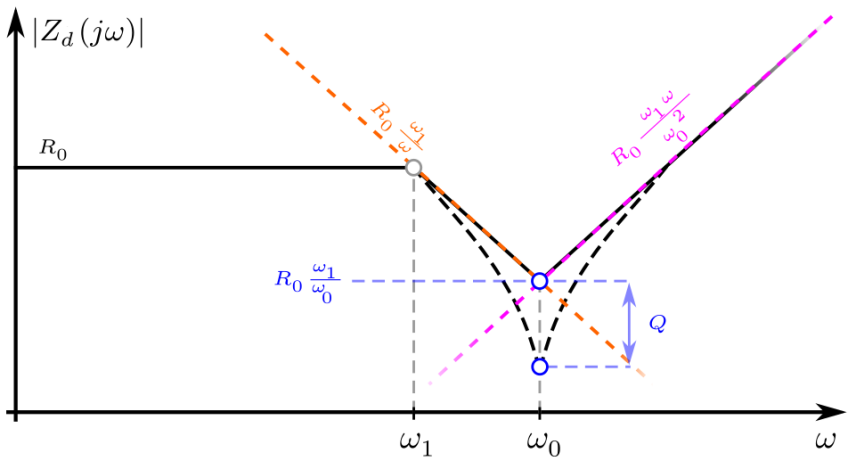


Fig. 2.11 Asymptotic construction of Bode plot of $|Z_d(j\omega)|$.

Studying the asymptotic behavior of $|Z_d(j\omega)|$ represented in the Bode plot of Fig. 2.11, it can be noted that the DC value in the traditional and QSW-ZVS mode is expressed as R_0. The response is then dominated by the first pole, which has an angular frequency equal to ω_1, according to the corresponding case. By equating the two asymptotes the intercept point occurs at $\omega = \omega_0$. With a first approximate analysis, the value at the intersection can be estimated by substituting ω_0 into the angular frequency variable in the expressions of the asymptotes, the resulting value being reported in Fig. 2.11. Including the effect of the quality factor Q, the value becomes equal to $R_0\omega_1/(Q\omega_0)$. A rigorous calculation, in turn, is carried out by substituting $\omega = \omega_0$ into the expression of $Z_d(s)$ in 2.39 and computing its magnitude, which provides the exact value of the minimum impedance relevant for the filter design:

$$|Z_d(j\omega_0)| = \frac{R_0}{Q}\sqrt{\frac{1}{1+(\omega_0/\omega_1)^2}}. \tag{2.40}$$

Consequently, the values of the damping components C_d and R_d can be calculated from equations (2.25) and (2.26), by enforcing the target impedance Z_{target} (i.e. the upper limit for the maximum allowable value of the filter output impedance) as:

$$Z_{\text{target}} = 10^{\frac{|Z_d(j\omega_0)|_{\text{dB}} - m_{\text{dB}}}{20}}. \tag{2.41}$$

To illustrate the application of the proposed methodology, a Buck converter characterized by the main parameter values listed in Table 2.6 is considered. Across its operating range, three illustrative cases, spanning the minimum, average, and maximum conditions of V_{in} and R_L (referred to as Case I, Case II, and Case III) are reported in Table 2.7, along with the corresponding C_{sw} values.

Table 2.6 Buck converter component values.

Parameter	**Value**
Inductor L_{f}	8.2 µH
Inductor ESR $R_{\text{L}_{\text{f}}}$	7.5 mΩ
Output capacitor C_{out}	240 µF
Capacitor ESR $R_{C_{\text{out}}}$	1 mΩ
High-side switch $R_{\text{HS}_{\text{on}}}$	1 mΩ
Low-side switch $R_{\text{LS}_{\text{on}}}$	1 mΩ
Switching frequency F_{sw}	1 MHz
Output voltage V_{out}	5 V

Table 2.7 Operating cases and corresponding parameter values.

	V_{in}	R_{L}	C_{SW}
Case I	20 V	0.33 Ω	4.1 nF
Case II	35 V	1.84 Ω	2.5 nF
Case III	45 V	3.35 Ω	3.19 nF

Based on filter design considerations outlined above and the optimal damping selection for the three considered cases, the EMI filter is implemented to satisfy the required EMI reduction for both the conventional converter and the QSW-ZVS operating mode. A target attenuation $\text{Att}_{\text{dB}} = 96\,\text{dB}$ is imposed, leading to the selection of a cutoff frequency approximately equal to $f_c \approx 3.8\,\text{kHz}$, an inductance $L_{\text{in}} = 12\,\mu\text{H}$, and a capacitance $C_{\text{in}} = 140\,\mu\text{F}$. To ensure that the filter output impedance

remains below the respective minimum of $Z_d(s)$ with a margin $m_{\mathrm{dB}} = 10\,\mathrm{dB}$, the corresponding damping elements are computed and reported in Table 2.8.

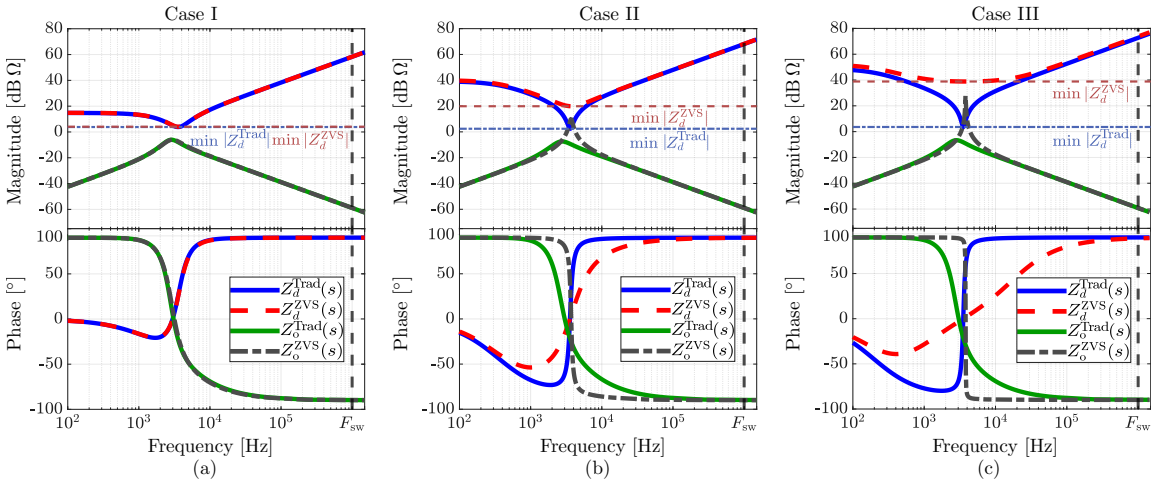


Fig. 2.12 Comparison of $Z_o(s)$ and $Z_d(s)$ with minimum impedance levels for damping network design for traditional and QSW-ZVS modes in Table 2.7. (a) Case I, (b) case II and (c) Case III.

The derived filters output impedance curves —$Z_o^{\mathrm{Trad}}(s)$ for the traditional mode and $Z_o^{\mathrm{ZVS}}(s)$ for QSW-ZVS operation— along with the evaluated $Z_d(s)$, are illustrated in Fig. 2.12. The resulting relative reduction of the damping capacitance in QSW-ZVS mode, quantified for the three conditions in Table 2.8, demonstrates an overall improvement compared to the traditional case. Specifically, when the values of R_L and V_{in} are in the average and maximum conditions (i.e., Case II and III), the requirement for a lower Z_{target}, related to a lower magnitude of the minimum of $Z_d(s)$, also depicted in Fig. 2.12, becomes more stringent for the conventional operating mode. This necessitates a lower filter output impedance, which consequently results in a larger damping capacitance.

Table 2.8 Damping network component values and size reduction comparison between capacitance in traditional and QSW-ZVS mode.

	$C_d{}^{\text{Trad}}$	$R_d{}^{\text{Trad}}$	$C_d{}^{\text{ZVS}}$	$R_d{}^{\text{ZVS}}$	$C_d{}^{\text{ZVS}}$ **% Reduction**
Case I	223.7 µF	310 mΩ	214.6 µF	320 mΩ	4.07%
Case II	276.7 µF	270 mΩ	27.6 µF	1.6 Ω	90.03%
Case III	231.4 µF	300 mΩ	2.6 µF	15.7 Ω	98.88%

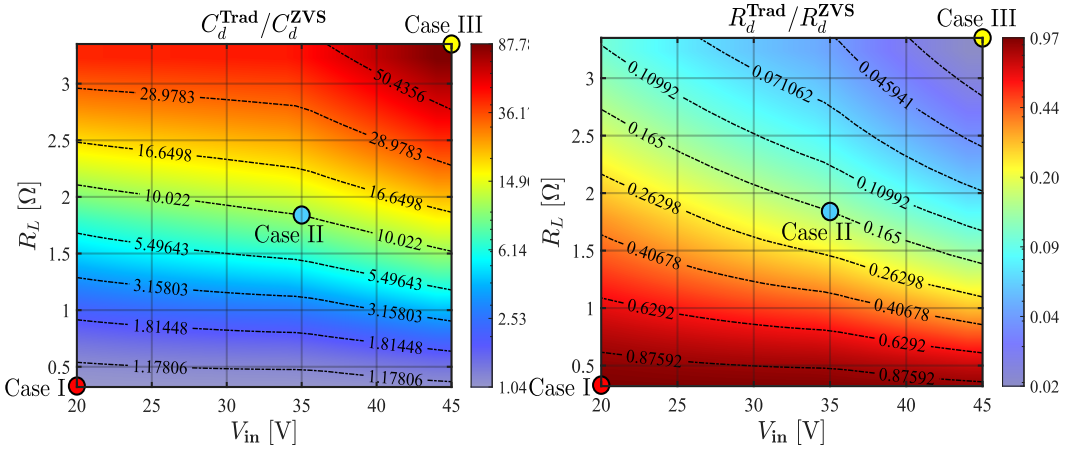


Fig. 2.13 Ratio of the values of the damping elements over the entire operating range of the Buck converter computed according to the developed criteria. (a) Capacitance C_d^{Trad} and C_d^{ZVS} and (b) resistances R_d^{Trad} and R_d^{ZVS}. Case I, II and III in Table 2.7 are highlighted by red, blue and yellow markers, respectively.

By extending this analysis over the entire range of R_L and V_{in} values, the results represented in Fig. 2.13 are obtained. From the ratio of the corresponding damping capacitances and resistances for the traditional and QSW-ZVS mode, it can be observed that as R_L and V_{in} values increase, C_d^{Trad} becomes larger than C_d^{ZVS}, whereas the resistances follow the opposite trend, reaching the minimum difference between traditional and QSW-ZVS case at high values of R_L and V_{in}. However, considering practical implementation, the damping resistance has a negligible impact, since a larger damping capacitance dominates size and cost. This can be observed by selecting real components for the damping network, as reported in table 2.9, which illustrates the variation in capacitance size between the conventional and QSW-ZVS cases. As for the damping resistances, they are specified with identical footprints, ensuring that their physical dimensions can be considered effectively equivalent in

Table 2.9 Selected components with physical dimensions of damping network capacitors.

Element	Value	Real component	Dim(mm)	Volume (mm^3)
Case I				
C_d^{Trad}	220 µF	Wurth Elektronik 865060657012	∅10×10.5	824.7
C_d^{ZVS}	220 µF	Wurth Elektronik 865060657012	∅10×10.5	824.7
Case II				
C_d^{Trad}	270 µF	Panasonic EEE-FN1H271UP	∅10×10.2	801.1
C_d^{ZVS}	27 µF	Wurth Elektronik 865080645009	∅6.3×7.7	240
Case III				
C_d^{Trad}	220 µF	Wurth Elektronik 865060657012	∅10×10.5	824.7
C_d^{ZVS}	2.2 µF	MURATA GCJ21BD71H225KE02L	2.0×1.25×1.25	3.13

all cases. Therefore, within the considered conditions, the design without QSW-ZVS becomes more critical due to the increased capacitance values.

The same principles can be extended to cascaded filter sections or other filter topologies, provided that the resulting $Z_{\text{o}}(s)$ is appropriately considered. In all cases, the filter output impedance should remain below the minimum of the impedances derived with the EET. Notably, the difference between the minimum values of $Z_{\text{d}}^{\text{Trad}}(s)$ and $Z_{\text{d}}^{\text{ZVS}}(s)$ provides an additional design margin for the filter output impedance, enabling a more flexible selection of damping components in the QSW-ZVS configuration.

To validate the proposed small-signal model and the design methodology, the LC filter developed for the QSW-ZVS case is also applied to the conventional operating mode under the same three cases previously analyzed, allowing the assessment of its impact on the converter TFs. Extensive simulations are then carried out using SIMPLIS circuit simulator.

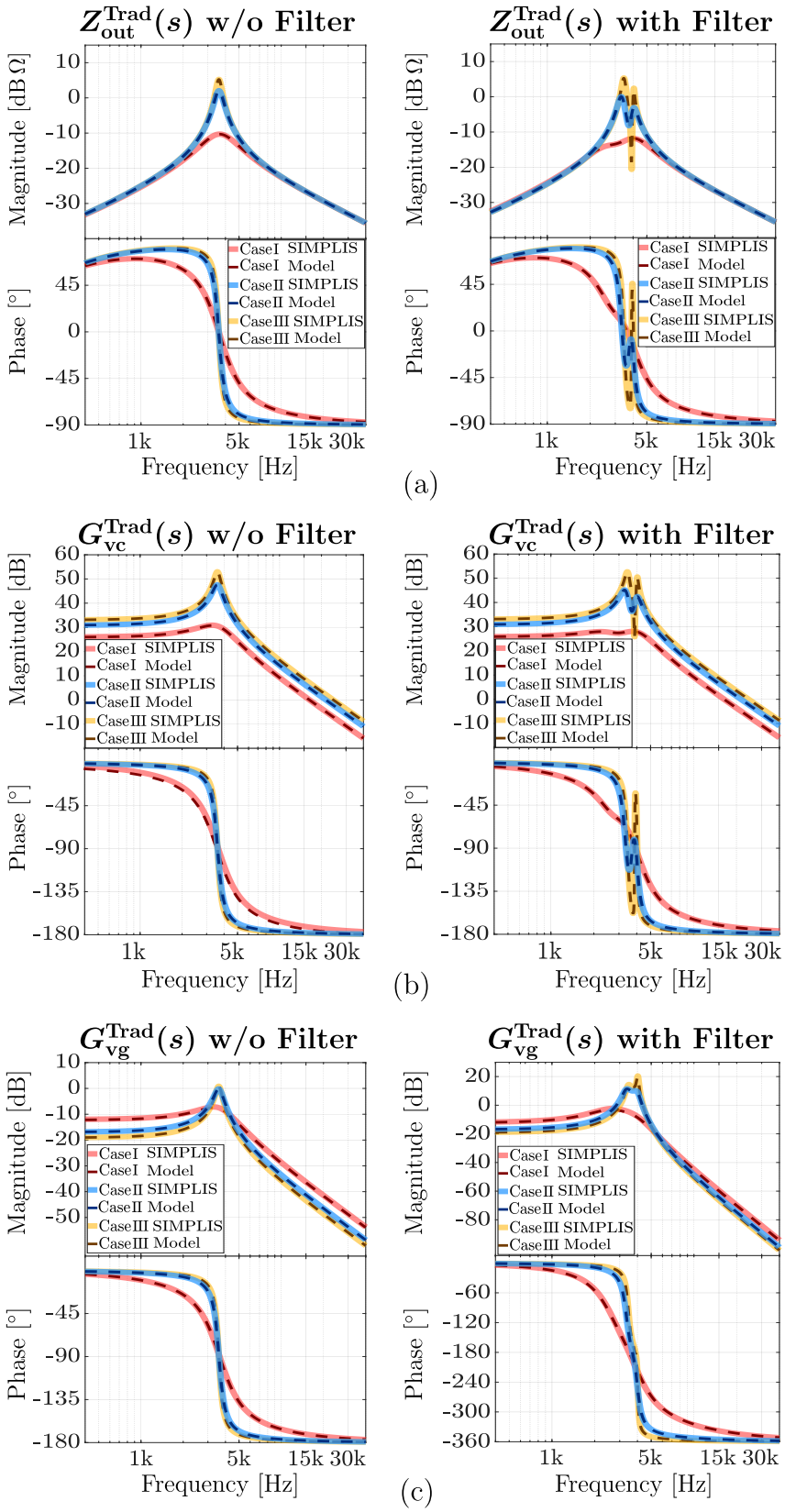


Fig. 2.14 TFs comparison without and with the EMI filter for both traditional and QSW-ZVS designs: (a) output impedance $Z_{out}(s)$, (b) control-to-output transfer function $G_{vc}(s)$, and (c) line-to-output transfer function $G_{vg}(s)$.

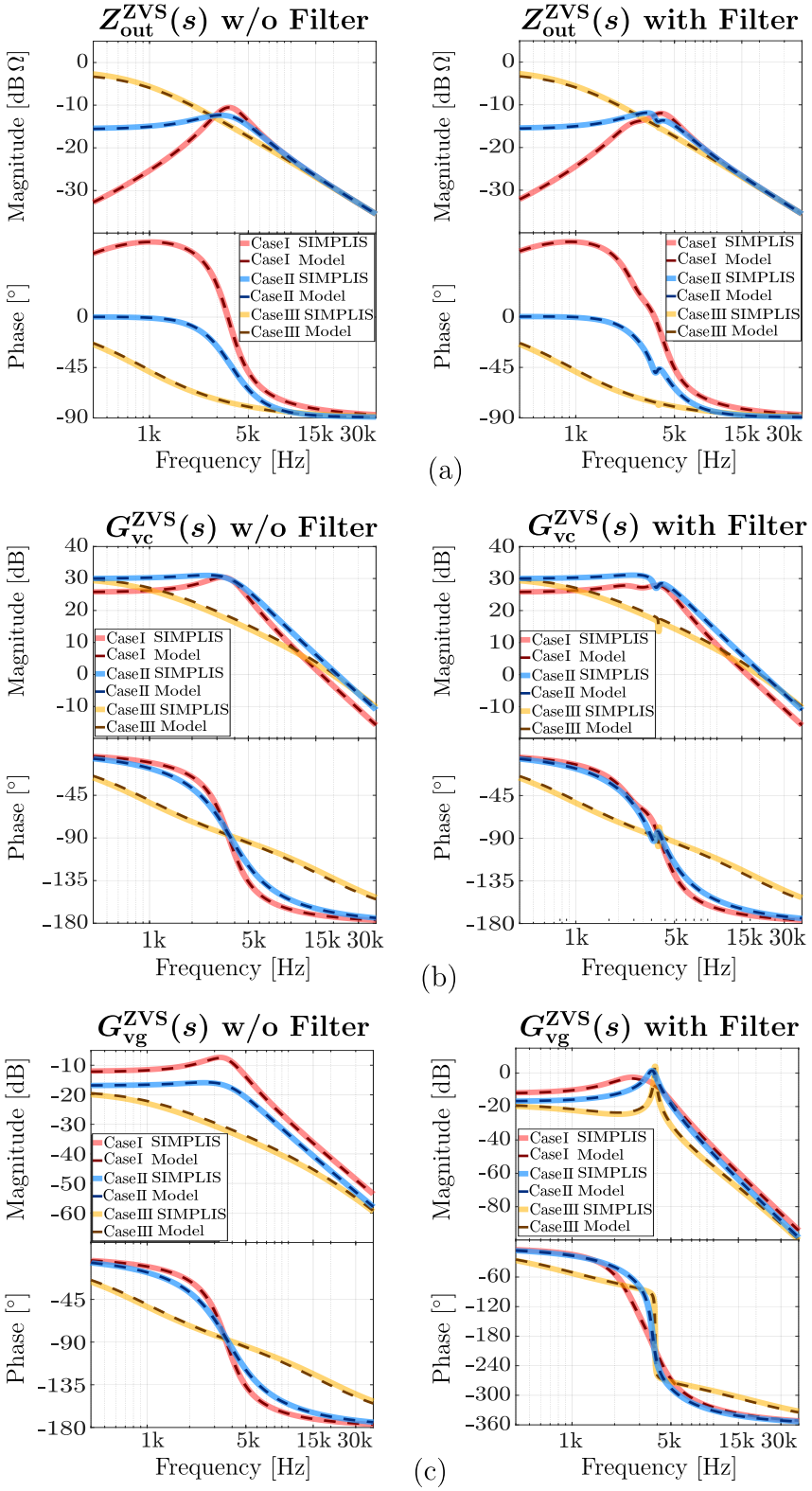


Fig. 2.15 TFs comparison without and with the EMI filter for both traditional and QSW-ZVS designs: (a) output impedance $Z_{\text{out}}(s)$, (b) control-to-output transfer function $G_{\text{vc}}(s)$, and (c) line-to-output transfer function $G_{\text{vg}}(s)$.

The resulting TFs obtained from the analytical model and from simulations show strong agreement for both traditional and QSW-ZVS designs, as illustrated in Fig. 2.14 and 2.15, thereby validating the accuracy of the small-signal model. The TFs $Z_{\text{out}}(s)$, $G_{\text{vc}}(s)$ and $G_{\text{vg}}(s)$ obtained both with and without the EMI filter further demonstrate that the filter designed for the QSW-ZVS case preserves the original converter behavior, in contrast, when QSW-ZVS is absent, the EET conditions are no longer satisfied, resulting in a modified system response.

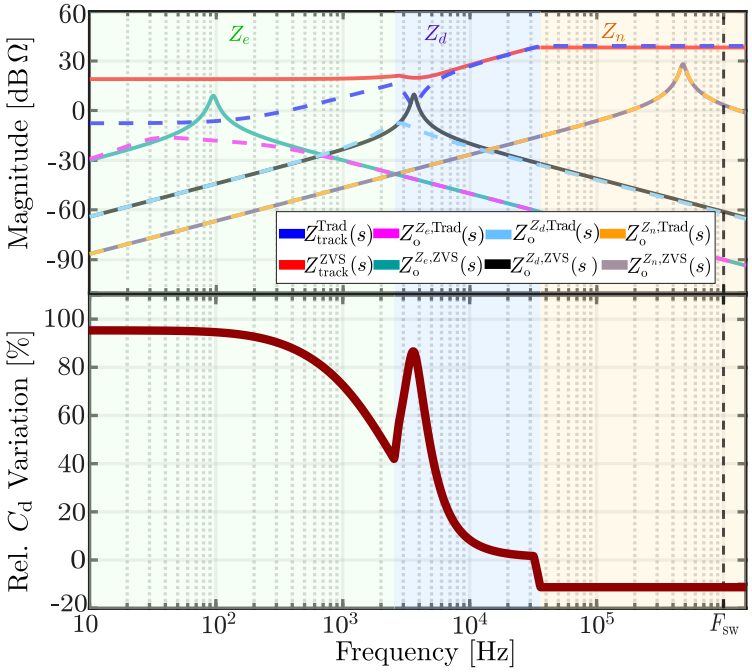


Fig. 2.16 EMI filter output impedances with different f_c designed to be constrained below the respective tracking lines, for traditional and QSW-ZVS mode. The bottom panel illustrates the relative variation of C_d^{ZVS} with respect to traditional case across the frequency.

To complete the study of C_d in the two operating modes, its frequency behavior is analyzed considering the case with intermediate values of R_L and V_{in} as a representative example (i.e. Case II). The filter cutoff frequency is swept over a range of frequencies, thereby covering the filter design cases corresponding to different Att_{dB} requirements, and the relative variation of the damping capacitance in QSW-ZVS condition with respect to the conventional case is evaluated, as depicted in Fig. 2.16. A tracking line $Z_{\text{track}}^{\text{Trad}}(s)$ for conventional converter and $Z_{\text{track}}^{\text{ZVS}}(s)$ for QSW-ZVS mode, representing the minimum value among Z_n(s), $Z_d(s)$ and $Z_e(s)$, is

reported in the plot as a dashed blue line for the conventional case and as a solid red for the QSW-ZVS one. Depending on the frequency interval in which f_c lies, the behavior is dominated by a different impedance derived with the EET. Specifically, in the first region, with a green background, the $Z_e(s)$ term is predominant, in the second one highlighted in blue, $Z_d(s)$ becomes critical for the filter design, and in the last orange section, the behavior is governed by $Z_n(s)$. In each of these areas, an illustrative example of the filter output impedance is identified as $Z_o^{Z_e}(s)$, $Z_o^{Z_d}(s)$ and $Z_o^{Z_n}(s)$ depending on the dominant impedance along the tracking line to which it is constrained, either under the QSW-ZVS or conventional condition. By computing the relative percentage variation of C_d^{ZVS} compared to traditional case, the curve in the lower portion of the plot is obtained. The maximum reduction of C_d^{ZVS} with respect to the conventional case occurs when the filter is centered at low frequencies, where the tracking line is dominated by $Z_e(s)$, and when it falls below the minimum of $Z_d(s)$. As the frequency increases and the $Z_n(s)$ curve becomes predominant, the overall trend slightly changes, since $Z_n^{\text{ZVS}}(s)$ exhibits a lower magnitude compared to the traditional case. Focusing on the central frequency region, which represents the practical range of interest for typical attenuation requirements, the QSW-ZVS technique is consistently advantageous for the design of a smaller and more compact EMI filter, as it requires a lower value of damping capacitor.

Therefore, through the application of the EET, the effects of the EMI filter on converter TFs are analyzed. The approach determines appropriate damping network components values across different operating points. By comparing the required damping capacitance under different operating conditions and as a function of frequency for both the QSW-ZVS and conventional cases, it is demonstrated that the application of the QSW-ZVS technique enables a more compact EMI filter design through a reduction in the required damping capacitance.

Chapter 3

Overview of EM simulators software and performed analysis

This chapter provides a comprehensive overview of the main commercial multiphysics EM simulation tools employed in electronic applications. The most widely adopted software suites—namely Ansys, Keysight PathWave, Cadence Design Systems, COMSOL Multiphysics, CST Studio Suite, and Altair—are reviewed and compared with respect to their numerical formulations, modeling capabilities, and typical application domains.

Depending on the electrical size of the structure, the frequency content of the signals, and the dominant physical phenomena, different electromagnetic formulations and numerical techniques may be required. The choice of solver must be guided by a clear understanding of the underlying assumptions and applicability of the available methods.

By presenting a structured comparison of simulation tools within this theoretical context, this chapter aims to provide a unified perspective on the range of options available to the designer. This overview supports the identification of appropriate tools for the electromagnetic analysis of electronic systems and to motivate the methodological choices adopted in the subsequent chapters of this work.

3.1 Analysis Workflow

Although different EM solvers rely on distinct numerical formulations and implementation strategies, which will be discussed in detail throughout this chapter, the overall simulation workflow follows the same fundamental principles introduced in Section 1.3.2. This workflow comprises the following four main stages.

- **Definition of the physical model**: generation of the electromagnetic model of the structure under investigation, including the definition of geometrical features, material properties, conductor layouts, and layer stack-up. Depending on the design flow, the model may be developed directly within the simulation environment or imported from external electronic and mechanical design tools.

- **Simulation setup**:

  Port Definition: the definition of the simulation ports establishes the electrical interfaces between the EM model and the external circuit used to excite and characterize the structure. Ports specify the locations at which voltages and currents are applied or extracted and therefore play a fundamental role in determining the electrical quantities obtained from the EM simulation. Depending on the considered application and on the physical structure under investigation, different types of ports can be employed. In particular, ports can be defined as single-ended or differential. A single-ended port describes an excitation with respect to a reference or return conductor, whereas a differential port defines the excitation between two conductors and is therefore suitable for structures in which the current flows between a pair of terminals.

  Boundary Conditions: these conditions define the electromagnetic constraints imposed on the physical structure or, when required by the numerical formulation, on the boundaries of the computational domain. Their role and implementation depend on the adopted numerical method. In volume-based approaches, where a finite computational domain is used to represent the surrounding space, suitable boundary conditions may be required to truncate the domain while reproducing the intended electromagnetic environment. These may include absorbing or radiation-type conditions for open-region problems, or symmetry and periodic conditions

when the corresponding properties can be exploited to reduce the computational domain.

Excitation and Solver Settings: they defines how the electromagnetic problem is driven and how the electrical quantities are exchanged between the EM model and the external circuit. Depending on the adopted solver and on the physical structure under investigation, different excitation schemes can be employed. For example, voltage or current sources can be used to represent localized circuit excitations, while lumped ports can be used to define a localized electrical interface between conductors. For transmission-line structures, wave ports can instead be employed to define the cross-section through which electromagnetic modes propagate into or out of the computational domain.

Frequency Range and Sampling: the frequency range of the simulation must be selected according to the physical phenomena that the EM model is intended to capture. The upper frequency limit should extend beyond the highest relevant frequency associated with the phenomena of interest. In switching power converters, for example, the relevant frequency range is not limited to the switching frequency, since the rapid voltage and current transitions occurring during switching introduce significant high-frequency spectral components. In particular, the frequency content of the voltage waveform at the switch-node, indicated in Fig. 1.1, is strongly related to the rise and fall times of the switching transitions.

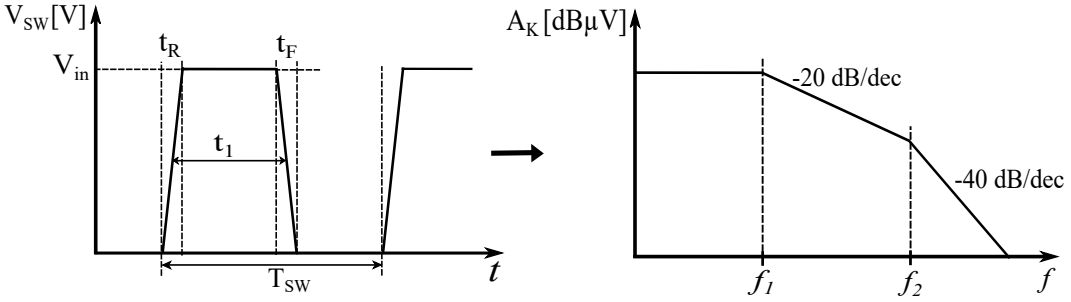


Fig. 3.1 Time domain waveform of switching node voltage of buck converter and its spectral envelope.

This behavior can be illustrated by considering a simplified trapezoidal representation of the switch-node voltage in the time domain and its corresponding harmonic spectral envelope, as shown in Fig. 3.1. The waveform is characterized by the

pulse width t_1, measured between the midpoints of the rising and falling edges, the switching period T_{SW}, the duty cycle

$$D = \frac{t_1}{T_{\mathrm{SW}}}, \tag{3.1}$$

and the rise and fall times t_R and t_F, respectively. Under the assumption of equal rise and fall times, i.e., $t_R = t_F$, the amplitude of the k-th harmonic can be expressed as [42]

$$A_k = 2DV_{\mathrm{in}} \left| \frac{\sin(k\pi D)}{k\pi D} \right| \left| \frac{\sin\left(k\pi \frac{t_R}{T_{\mathrm{SW}}}\right)}{k\pi \frac{t_R}{T_{\mathrm{SW}}}} \right|. \tag{3.2}$$

Furthermore, the parasitic inductances and capacitances of the physical interconnections can modify the switching transitions and introduce resonant behavior. The fast voltage and current edges can excite these parasitic resonances, resulting in high-frequency ringing superimposed on the switching waveforms and consequently in additional spectral components around the corresponding resonant frequencies. The frequency sampling must be selected to provide sufficient resolution of the frequency-dependent behavior. The frequency points can be distributed linearly or logarithmically, depending on the application. A logarithmic distribution is generally convenient when the analysis spans several decades, whereas a finer or locally refined sampling may be required in frequency regions characterized by resonances or rapid variations of the quantities. The number and distribution of frequency points therefore represent a trade-off between the resolution of the extracted frequency response and the computational cost of the simulation.

- **EM simulation**: the electromagnetic behavior of the structure is evaluated through the numerical solution of Maxwell's equations. To this end, the physical model is discretized using a suitable mesh, and the resulting mathematical problem is solved according to the formulation adopted by the selected EM solver. The main numerical methods and solution procedures are presented in the following sections of this chapter.

- **Post-processing of results**: the final stage of the workflow consists of extracting the quantities of interest from the numerical solution and processing them accord-

ing to the objectives of the analysis. Depending on the application, the simulation results may include field distributions, port voltages and currents, scattering parameters, and impedance or admittance matrices. For the analyses considered in this work, the ultimate goal of the post-processing stage is to obtain a broadband model that represents the parasitic elements of the physical structure and can be used outside the EM simulation environment for circuit-level analysis. In particular, the extracted S-, Z-, or Y-parameter matrices must be converted into a suitable equivalent circuit model compatible with circuit simulation tools such as HSPICE, PSpice, Spectre, Simplis and so on. The transformation and fitting process of the extracted frequency-domain data into a circuit-compatible representation are described in detail in the next chapter in Section 4.1.4, 4.2.3 and 4.3.

3.2 Classification of EM simulator capability

Commercial EM simulation tools adopt a wide spectrum of numerical methodologies and modeling strategies to analyze devices and structures operating over diverse frequency ranges and spatial scales. The predictive accuracy and computational efficiency of a given EM solver are primarily dictated by its underlying assumptions, numerical formulations, discretization strategies, and the extent to which relevant physical phenomena are captured. Consequently, the selection of an appropriate EM simulator requires a comprehensive understanding of its intrinsic capabilities and limitations in relation to the problem under investigation.

To enable a systematic comparison among different EM simulators, a structured classification can be introduced based on the fundamental characteristics that influence their level of physical accuracy and computational performance. In particular, EM solvers can be categorized according to:

- the numerical methods employed to solve Maxwell's equations, including integral-equation, differential-equation, and hybrid formulations;
- the geometrical representation and discretization strategies, encompassing surface-based, volume-based meshing and the level of geometric detail that can be accurately captured;

- the range of EM effects and multiphysics interactions included in the analysis, as well as the corresponding validity domain in terms of frequency range and underlying physical assumptions, which determine the applicability of the solver to specific operating regimes and the extent to which relevant phenomena can be accurately captured.

This classification provides a structured basis for evaluating and comparing different simulation tools. It enables the identification of the most suitable approach for a specific application, ensuring alignment between the solver theoretical formulation and the physical characteristics of the device, and the operational frequency range, together with the required level of predictive accuracy.

3.2.1 Numerical Methods

The selection of an appropriate EM numerical method strongly depends on the electrical size of the structure, the complexity of the material composition, and the dominant physical phenomena in the operating frequency range of interest. EM simulation software which uses integral-equation solving techniques, the methods of moments (MoM) and multilevel fast multipole method (MLFMM) are commonly used. Typically, the numerical methods that use differential-equation (DE) solving techniques include the finite-difference time-domain (FDTD), finite-element-method (FEM), and transmission-line-matrix (TLM) methods. In contrast, asymptotic techniques include physical optics (PO), geometric optics (GO), and the uniform theory of diffraction (UTD) [43–52].

In power electronic systems, and in particular for DC-DC converters integrating PCBs and semiconductor packages, the electromagnetic problem typically falls within the regime highlighted in blue in Fig. 3.2. In this operating region, the principal numerical methods adopted for accurate modeling and analysis are the Method of Moments and the Finite Element Method.

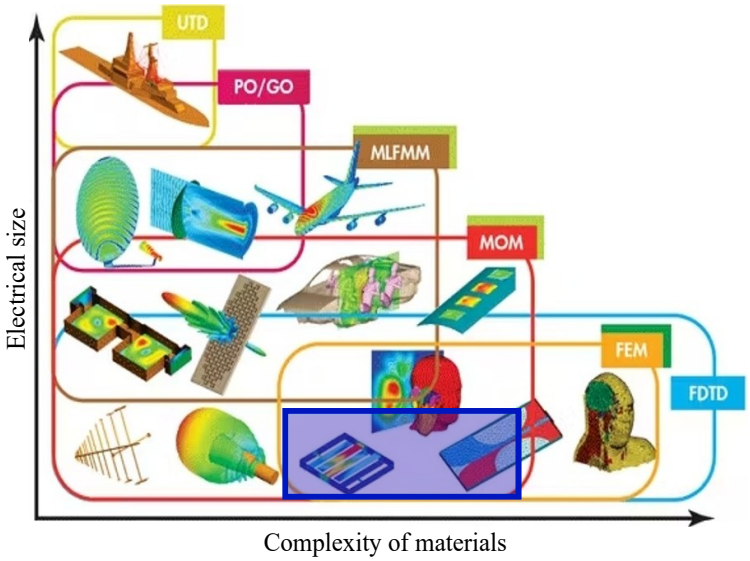


Fig. 3.2 Classification of different main numerical methods adopted by EM simulators, highlighting in blue the region of applicability relevant to DC-DC converters. Adapted from the FEKO User Manual Image [53].

From a mathematical perspective, numerical EM methods differ in the formulation adopted to solve Maxwell's equations.

Maxwell's equations constitute the starting point for all classical EM field formulations and describe the relationships between the fundamental field quantities: the electric field **E**, the magnetic field **H**, the electric flux density **D**, the magnetic flux density **B**, the current density **J**, and the charge density ρ.

The electric field **E** and magnetic field **H** represent the fundamental vector fields describing EM interaction, while **D** and **B** represent the corresponding flux densities in media.

These equations can be obtained starting from Faraday's law of induction:

$$\nabla \times \mathbf{E} = -\frac{\partial \mathbf{B}}{\partial t} \tag{3.3}$$

where the negative sign expresses Lenz's law, indicating that the induced electric field opposes the variation of the magnetic flux density **B**.

The magnetic field behavior is described by the Ampère–Maxwell law:

$$\nabla \times \mathbf{H} = \mathbf{J} + \frac{\partial \mathbf{D}}{\partial t} \tag{3.4}$$

Gauss's law for the electric field relates the electric flux density $\mathbf{D}$ to the charge density ρ:

$$\nabla \cdot \mathbf{D} = \rho \tag{3.5}$$

while Gauss's law for magnetism states:

$$\nabla \cdot \mathbf{B} = 0 \tag{3.6}$$

The operator ∇ denotes the vector differential operator, also known as the nabla operator, defined as

$$\nabla = \left(\frac{\partial}{\partial x}, \frac{\partial}{\partial y}, \frac{\partial}{\partial z} \right)$$

The curl operator $\nabla \times (\cdot)$ describes the local rotational behavior of a vector field and is associated with circulation phenomena.

The divergence operator $\nabla \cdot (\cdot)$ describes the net flux of a vector field flowing out of an infinitesimal volume. In particular, the divergence of the electric flux density $\mathbf{D}$ is associated with electric charge density, while the divergence-free condition of the magnetic flux density (i.e. $\nabla \cdot \mathbf{B} = 0$) reflects the absence of magnetic monopoles.

The gradient operator $\nabla(\cdot)$, applied to a scalar field, produces a vector field pointing in the direction of maximum spatial variation.

The operator $\frac{\partial}{\partial t}$ represents temporal variation.

The above Equations (3.3)–(3.6), are completed by the constitutive relations, which describe the EM response of materials. For linear, isotropic, and homogeneous media, the constitutive relations between the field quantities are expressed as:

$$\mathbf{B} = \mu \mathbf{H}, \qquad \mathbf{D} = \varepsilon \mathbf{E} \tag{3.7}$$

where ε is the absolute permittivity of the medium [F/m] and μ is the absolute permeability [H/m]. In the particular case of vacuum (or free space), these quantities reduce to the fundamental physical constants ε_0 and μ_0, representing the permittivity and permeability of free space, respectively.

Finally, conduction phenomena in lossy materials are described by Ohm's law in differential form:

$$\mathbf{J} = \sigma \mathbf{E} \tag{3.8}$$

where σ denotes the electrical conductivity of the material [S/m].

For many electromagnetic simulation problems, it is convenient to reformulate Maxwell's equations in the frequency domain by assuming a time-harmonic dependence of the form $e^{j\omega t}$. Under this assumption:

$$\frac{\partial}{\partial t} \rightarrow j\omega$$

leading to:

$$\nabla \times \mathbf{E} = -j\omega \mathbf{B} \tag{3.9}$$

$$\nabla \times \mathbf{H} = \mathbf{J} + j\omega \mathbf{D} \tag{3.10}$$

$$\nabla \cdot \mathbf{D} = \rho \tag{3.11}$$

$$\nabla \cdot \mathbf{B} = 0 \tag{3.12}$$

In the frequency-domain representation, the total current density can be expressed as the sum of the conduction and displacement current contributions:

$$\mathbf{J}_{\text{tot}} = \sigma \mathbf{E} + j\omega\varepsilon \mathbf{E} = (\sigma + j\omega\varepsilon)\mathbf{E}. \tag{3.13}$$

In the following, the fundamental principles of MoM and FEM are discussed, with the objective of highlighting their respective modeling capabilities, numerical

characteristics, and inherent limitations. This overview provides the necessary background to understand how these techniques are implemented in practical EM simulators and how their theoretical foundations directly influence their applicability to specific classes of problems.

Method of Moments

The Method of Moments is a numerical technique based on the integral formulation of Maxwell's equations. The fundamental idea is that the scattered electromagnetic fields can be expressed in terms of equivalent surface currents through the dyadic Green's function of the background medium, where the Green's function represents the field response at a given observation point due to an elementary source located elsewhere in space.

The total electric field $\mathbf{E}^{tot}$ is commonly expressed as the superposition of a known incident field $\mathbf{E}^{inc}$ and an unknown scattered field $\mathbf{E}^{scat}$ generated by the induced currents on the structure:

$$\mathbf{E}^{tot}(\mathbf{r}) = \mathbf{E}^{inc}(\mathbf{r}) + \mathbf{E}^{scat}(\mathbf{r}). \tag{3.14}$$

For perfectly conducting surfaces, the boundary condition imposes that the tangential component of the total electric field vanishes:

$$\hat{\mathbf{n}} \times \mathbf{E}^{tot} = 0 \tag{3.15}$$

where $\hat{\mathbf{n}}$ is the unit normal vector to the surface.

The scattered electric field produced by a surface current density $\mathbf{J}(\mathbf{r}')$ can be expressed in integral form as

$$\mathbf{E}^{scat}(\mathbf{r}) = \int_S \mathbf{G}(\mathbf{r}, \mathbf{r}') \cdot \mathbf{J}(\mathbf{r}') \, \mathrm{d}S', \tag{3.16}$$

where $\mathbf{r}$ denotes the observation point, while $\mathbf{r}'$ represents the source point on the surface S, and $\mathbf{G}(\mathbf{r}, \mathbf{r}')$ denotes the Green's function of the background medium.

The surface current density $\mathbf{J}(\mathbf{r})$ is an unknown quantity and is approximated by expanding it in terms of a finite set of known basis functions:

$$\mathbf{J}(\mathbf{r}) \approx \sum_{n=1}^{N} I_n \mathbf{f}_n(\mathbf{r}), \tag{3.17}$$

where $\mathbf{f}_n(\mathbf{r})$ are the chosen basis functions and I_n are the unknown expansion coefficients. This expansion reduces the continuous unknown current distribution to a finite number of degrees of freedom.

Substituting the current expansion into the integral equation yields a residual error, since the approximate solution cannot satisfy the equation exactly at every point on the surface. The MoM enforces that this residual be orthogonal to a set of testing functions $\mathbf{w}_m(\mathbf{r})$, leading to a weighted integral formulation of the problem.

In the Galerkin approach, which is commonly adopted in EM applications, the testing functions are chosen to be identical to the basis functions:

$$\mathbf{w}_m(\mathbf{r}) = \mathbf{f}_m(\mathbf{r}). \tag{3.18}$$

Applying this testing procedure transforms the continuous operator equation into a discrete system of linear equations:

$$\mathbf{ZI} = \mathbf{V}, \tag{3.19}$$

where $\mathbf{Z}$ is the impedance matrix, $\mathbf{I}$ is the vector of unknown expansion coefficients, and $\mathbf{V}$ is the excitation vector associated with the incident field.

The elements of the impedance matrix arise from the interaction between the basis function $\mathbf{f}_n$, representing a source current distribution, and the testing function $\mathbf{f}_m$, representing the observation of the resulting field. They are defined as

$$Z_{mn} = \int_S \int_S \mathbf{f}_m(\mathbf{r}) \cdot \mathbf{G}(\mathbf{r}, \mathbf{r}') \cdot \mathbf{f}_n(\mathbf{r}') \, \mathrm{d}S \, \mathrm{d}S'. \tag{3.20}$$

Once the system is solved for the unknown coefficients I_n, the surface current distribution on the structure is fully determined. The EM fields and relevant quantities, such as port parameters and equivalent circuit models, can then be computed.

Owing to its surface-based discretization and current-oriented formulation, the Method of Moments is particularly well suited for the EM analysis of planar and layered structures. By discretizing only conductor surfaces, rather than the entire computational volume, MoM significantly reduces the number of unknowns compared to volumetric methods. This characteristic makes it especially effective for PCB-level modeling, where conductive traces, reference planes, vias, and multilayer stackups can be accurately represented using analytical or layered Green's functions.

A direct consequence of the integral-equation formulation adopted by MoM is the global EM coupling among all discretized elements. Each basis function interacts with every other through the Green's function of the background medium, leading to a fully populated (dense) impedance matrix. This global coupling results in memory requirements that scale quadratically with the number of unknowns $\mathcal{O}(N^2)$, while the computational complexity of direct solution techniques can approach cubic scaling $\mathcal{O}(N^3)$. These characteristics impose practical limitations on problem size and make MoM computationally demanding for large or highly detailed models.

In addition, the reliance on analytical or semi-analytical Green's functions makes MoM most efficient for environments that can be approximated as homogeneous or stratified media. While this assumption is well satisfied for PCB and interconnect analysis, it reduces the efficiency of the method when applied to structures featuring complex three-dimensional geometries and strongly inhomogeneous material distributions, such as those encountered in detailed semiconductor package modeling.

Finite Element Method

The Finite Element Method instead, is a numerical technique based on the differential formulation of Maxwell's equations, in which the EM problem is solved by directly computing the field quantities within a finite computational domain [54, 55]. Unlike integral-equation-based methods, FEM operates on the local form of Maxwell's equations and therefore requires discretization of the entire solution volume.

Starting from Maxwell's equations in the frequency domain and assuming linear, isotropic, and time-invariant media, the EM problem can be formulated in terms of

the electric field $\mathbf{E}$ as the vector wave equation

$$\nabla \times \left(\mu^{-1}\nabla \times \mathbf{E}\right) - \omega^2 \varepsilon \mathbf{E} = -j\omega \mathbf{J}. \tag{3.21}$$

This equation constitutes the differential form of the EM boundary value problem.

Since most practical EM problems are defined over unbounded regions, the computational domain is truncated by introducing artificial boundaries. These boundaries are typically terminated using absorbing boundary conditions or perfectly matched layers (PMLs) in order to emulate open-region radiation and minimize spurious reflections.

To apply the Finite Element Method, the strong formulation is converted into a weak form. Let $\mathbf{W}$ be a suitable vector test function belonging to the same functional space as the solution. Multiplying the governing equation by $\mathbf{W}$ and integrating over the computational domain V yields

$$\int_V \mathbf{W} \cdot \left[\nabla \times \left(\mu^{-1}\nabla \times \mathbf{E}\right) - \omega^2 \varepsilon \mathbf{E}\right] \mathrm{d}V = -j\omega \int_V \mathbf{W} \cdot \mathbf{J}\, \mathrm{d}V. \tag{3.22}$$

By applying vector identities and integration by parts, the weak form can be expressed as

$$\int_V (\nabla \times \mathbf{W}) \cdot \mu^{-1} (\nabla \times \mathbf{E})\, \mathrm{d}V - \omega^2 \int_V \mathbf{W} \cdot \varepsilon \mathbf{E}\, \mathrm{d}V = -j\omega \int_V \mathbf{W} \cdot \mathbf{J}\, \mathrm{d}V, \tag{3.23}$$

where boundary terms either vanish or are incorporated through the imposed boundary conditions. This variational formulation ensures numerical stability and constitutes the mathematical foundation of the FEM approach.

The computational domain V is discretized into a finite number of non-overlapping elements, typically tetrahedra in three-dimensional electromagnetic problems. The electric field is approximated within the domain as a finite expansion

$$\mathbf{E}(\mathbf{r}) \approx \sum_{n=1}^{N} e_n \mathbf{N}_n(\mathbf{r}), \tag{3.24}$$

where $\mathbf{N}_n(\mathbf{r})$ are vector basis functions and e_n are the unknown expansion coefficients.

In EM FEM formulations, edge-based vector basis functions (Nédélec elements) are employed. These functions enforce tangential field continuity across element boundaries and prevent the appearance of nonphysical spurious solutions. Applying the Galerkin method, the test functions are chosen to coincide with the basis functions,

$$\mathbf{W}_m(\mathbf{r}) = \mathbf{N}_m(\mathbf{r}), \tag{3.25}$$

leading to a discrete system of algebraic equations.

The FEM discretization results in the linear system

$$\mathbf{Ke} = \mathbf{f}, \tag{3.26}$$

where $\mathbf{e}$ is the vector of unknown field coefficients. The system matrix $\mathbf{K}$ is given by

$$K_{mn} = \int_V (\nabla \times \mathbf{N}_m) \cdot \mu^{-1} (\nabla \times \mathbf{N}_n) \, \mathrm{d}V - \omega^2 \int_V \mathbf{N}_m \cdot \varepsilon \mathbf{N}_n \, \mathrm{d}V, \tag{3.27}$$

while the excitation vector $\mathbf{f}$ is defined as

$$f_m = -j\omega \int_V \mathbf{N}_m \cdot \mathbf{J} \, \mathrm{d}V. \tag{3.28}$$

Owing to the locality of the basis functions, the resulting system matrix is sparse, since each basis function interacts only with neighboring elements. This sparsity enables the efficient use of direct or iterative sparse solvers and represents a major computational advantage of the FEM approach.

The Finite Element Method is particularly well suited for the analysis of problems involving arbitrary three-dimensional geometries and strongly inhomogeneous material distributions. This makes FEM especially effective for package-level and device-level modeling, where structures such as bond wires, solder bumps, vias, and complex dielectric regions must be represented with high geometric fidelity.

However, the volumetric discretization inherently leads to a large number of unknowns, especially when electrically large air regions or fine geometrical details are present. As a result, FEM simulations can become computationally demanding for large scale problems or broadband analyses, highlighting the complementary roles of FEM and surface-based methods within EM simulation workflows.

3.2.2 Geometrical representation

EM simulation tools can also be classified according to the geometrical representation adopted in the numerical formulation, which directly impacts both the modeling accuracy and the associated computational cost:

- 2D solvers assume invariance of the electromagnetic fields along one spatial direction, reducing the problem to the analysis of a two-dimensional cross-section, typically in the transverse plane. This approach is commonly used for the characterization of transmission line structures, such as microstrip or stripline configurations, where the fields can be accurately approximated from the cross-sectional geometry. Since the problem is reduced to two dimensions, the computational cost in terms of memory and simulation time is significantly lower. However, this simplification neglects variations and current flow along the third dimension, limiting its applicability to strictly uniform or quasi-uniform structures.

- 2.5D (planar 3D) solvers extend this approach by considering electromagnetic interactions in all three spatial directions while assuming that the geometry can be represented as a stack of planar conductive layers embedded in stratified dielectric media. In this formulation, conductors are typically modeled as infinitely thin surfaces lying on parallel planes. This approach is particularly well suited for printed circuit boards and integrated interconnect structures, where most of the geometry consists of planar traces distributed across multiple layers. The main advantage of planar solvers lies in their computational efficiency, as only the conductor surfaces are discretized using two-dimensional mesh elements (e.g., triangles or rectangles). However, this formulation introduces limitations in the representation of vertical or fully three-dimensional features. While vias and inter-layer connections can be included, their modeling is often approximate, and detailed current distributions or complex geometrical features cannot be accurately captured. As a result, planar solvers are most effective when the EM behavior is dominated by horizontal structures and inter-layer coupling effects remain moderate.

- Full 3D solvers provide the most general and accurate representation by allowing arbitrary geometries and material distributions in all spatial directions. In this case, the entire computational domain, including conductors, dielectrics, and surrounding air, is discretized using volumetric mesh elements, typically tetrahedra or hexahedra. This enables the accurate modeling of complex structures such as connectors, bond wires, vias with detailed geometry, and non-planar interconnects, as well as the full characterization of electromagnetic coupling in three dimensions.

Using a microstrip structure as an example, a full 3D solver discretizes not only the metallic trace but also the dielectric substrate and the surrounding air region, whereas a planar solver discretizes only the conductor surfaces, accounting for the surrounding media through Green's functions. Despite this difference, both approaches are based on full-wave formulations of Maxwell's equations; therefore, the use of two-dimensional mesh elements in planar solvers does not imply a two-dimensional electromagnetic problem.

In all cases, the discretization strategy plays a critical role in the accuracy and efficiency of the simulation. The geometrical features of the structure, including dimensions, spacing, and material interfaces, determine the required mesh density and, consequently, the number of unknowns and computational cost.

From a computational perspective, planar solvers offer a significant reduction in simulation time and memory usage compared to full 3D approaches. However, as the complexity of the geometry increases—particularly in the presence of strong vertical coupling, complex via structures, or fully three-dimensional current paths—the use of full 3D solvers becomes necessary to ensure accurate results.

3.2.3 Physical Modeling Regime

The selection of an appropriate EM solver also depends on the range of physical phenomena that must be accurately captured during the simulation. In particular, depending on the operating frequency and on the electrical size of the structure relative to the wavelength, EM solvers can be broadly classified into two main categories.

- Quasi-static solvers are based on simplified forms of Maxwell's equations, obtained under the assumption that the temporal variation of the EM fields is sufficiently slow such that wave propagation effects can be neglected. Under this approximation, the EM behavior is treated as locally instantaneous. As a result, quasi-static solvers often exploit a decomposition of the problem into electrostatic and magnetostatic contributions, corresponding respectively to capacitive and inductive effects. This separation is justified when displacement current and conduction current can be treated independently due to the electrical smallness of the structure with respect to the wavelength. The validity of the quasi-static approximation is generally ensured when the characteristic dimension L of the structure is much smaller than the wavelength λ associated with the highest frequency component of interest. Under these conditions, phase variations across the structure are negligible, and propagation and radiation effects can be safely neglected. This class of solvers is particularly effective for low-frequency applications and are widely employed for the extraction of parasitic resistive, inductive, and capacitive parameters in power electronic systems, printed circuit boards, and semiconductor packages. Their primary advantages include reduced computational complexity, efficient handling of electrically small structures, and straightforward integration with circuit-level simulation environments. For these reasons, quasi-static methods are commonly adopted during early-stage design and for system-level analysis in power electronics.

- Full-wave solvers, in contrast, are based on the complete set of Maxwell's equations without simplifying assumptions. These methods fully account for the coupling between electric and magnetic fields and accurately describe wave propagation phenomena. As a result, they are capable of modeling high-frequency effects such as propagation delays, reflections, radiation, dispersion, and resonance phenomena. Full-wave approaches are required when the electrical size of the structure becomes comparable to the wavelength, or when accurate prediction of field distribution, radiation losses, and EM coupling is critical. Although they are computationally more demanding, due to the need to resolve field variations over the entire domain, full-wave solvers provide

a comprehensive and physically consistent description of the EM behavior across a wide frequency range.

In summary, the choice between quasi-static and full-wave EM solvers must be guided by an assessment of the operating frequency range, the electrical size of the structure, and the physical effects of interest, so as to ensure an appropriate balance between modeling accuracy and computational efficiency.

3.2.4 Validity limits of modeling approaches

The applicability of a given EM simulation approach is limited by the assumptions on which it is based. While quasi-static and full-wave solvers represent complementary tools for the analysis of interconnects and structures encountered in power electronic systems, their domains of validity must be carefully evaluated in relation to the operating conditions of the problem under investigation [56–60]. Accordingly, the validity range of the quasi-static approximation is examined, and the limitations associated with the use of full-wave solvers in the low-frequency regime are discussed.

Quasi-static approximation

The quasi-static approximation provides the theoretical basis for simplified EM formulations and establishes the conditions under which electrostatic, magnetostatic, or quasi-static models can be employed instead of the full set of Maxwell's equations [61, 62]. The validity of these approximations depends on the relative time scales associated with the physical mechanisms involved in the electromagnetic response of the system. If the characteristic time scale of the sources is sufficiently large compared to the propagation time across the structure, dynamic wave effects can be neglected and simplified formulations remain accurate. To this purpose, three characteristic times are commonly introduced.

- The *electric charge relaxation time* τ_e represents the time required for free electric charge to decay within a conductive material. It is defined as

$$\tau_e = \frac{\varepsilon}{\sigma}. \tag{3.29}$$

- The *magnetic diffusion time* τ_m characterizes the time required for magnetic fields, and hence the associated current density, to diffuse into a conductor. It can be expressed as

$$\tau_m = \frac{L^2}{D_m}, \tag{3.30}$$

where L is a characteristic spatial dimension of the structure and D_m is the magnetic diffusion coefficient, defined as

$$D_m = \frac{1}{\mu\sigma}. \tag{3.31}$$

- The *electromagnetic propagation time* τ_{em} represents the time required for an electromagnetic wave to propagate over a distance L and is given by

$$\tau_{em} = \frac{L}{c}, \qquad c = \frac{1}{\sqrt{\mu\varepsilon}}, \tag{3.32}$$

where c is the speed of electromagnetic wave propagation in the medium.

Let τ denote the characteristic time scale of variation of the sources, such as currents or voltages. The electromagnetic behavior of the system can be classified by comparing τ with the characteristic times τ_e, τ_m, and τ_{em}. In particular, when the propagation time satisfies $\tau_{em} \ll \tau$, electromagnetic wave effects are negligible and the system can be treated as electrically small. Under this condition, spatial phase variations across the structure are insignificant and retardation effects can be ignored.

In the electro-quasi-static (EQS) regime, magnetic induction effects are neglected. This assumption corresponds to considering that the temporal variation of the magnetic flux density does not significantly contribute to the electric field distribution

$$\frac{\partial \mathbf{B}}{\partial t} \approx 0. \tag{3.33}$$

As a direct consequence of Faraday's law in (3.3), the electric field becomes approximately irrotational:

$$\nabla \times \mathbf{E} \approx 0. \tag{3.34}$$

The validity of the EQS approximation can be assessed by estimating the error introduced by neglecting magnetic induction. The quasi-static electric field can be estimated as

$$E \sim \frac{\rho L}{\varepsilon_0}. \tag{3.35}$$

The neglected magnetic contribution leads to an error field whose relative magnitude scales as

$$\frac{E_{\text{error}}}{E} \sim \frac{\mu_0 \varepsilon_0 L^2}{\tau^2}. \tag{3.36}$$

This ratio becomes negligible if

$$\mu_0 \varepsilon_0 \frac{L^2}{\tau^2} \ll 1, \tag{3.37}$$

which can be rewritten as

$$L \ll \frac{\tau}{\sqrt{\mu_0 \varepsilon_0}} = \lambda, \tag{3.38}$$

where λ is the electromagnetic wavelength associated with the characteristic time τ.

In the magneto-quasi-static (MQS) regime, electric displacement effects are neglected while magnetic induction remains dominant. This corresponds to assuming that the displacement current term in Ampère's law is negligible:

$$\frac{\partial \mathbf{D}}{\partial t} \approx 0. \tag{3.39}$$

Under this assumption, Ampère's law in (3.4) reduces to

$$\nabla \times \mathbf{H} \approx \mathbf{J}. \tag{3.40}$$

By estimating the quasi-static magnetic field as

$$H \sim JL \tag{3.41}$$

and evaluating the contribution of the neglected displacement current, the relative error introduced by this approximation again scales as

$$\frac{H_{\text{error}}}{H} \sim \frac{\mu_0 \varepsilon_0 L^2}{\tau^2}. \tag{3.42}$$

Therefore, the MQS approximation is valid under the same condition

$$\frac{L}{c} \ll \tau. \tag{3.43}$$

The electro-magnetic quasi-static (EMQS) regime represents an intermediate case in which both electric and magnetic fields vary in time and remain mutually coupled, yet EM wave propagation effects are still negligible. In this regime, the fields are determined without accounting for propagation delays by the source distribution at a given time.

It is important to emphasize that the absence of explicit time derivatives in the quasi-static equations does not imply that the sources or fields are time-invariant. Rather, it indicates that, at any given instant, a snapshot of the source distribution uniquely determines the corresponding field distribution at that same instant.

The general condition for the validity of the quasi-static approximation can therefore be expressed as

$$L \ll \lambda, \tag{3.44}$$

meaning that an EM wave can propagate across the characteristic length of the system in a time that is short compared to the time scale of interest. This criterion provides a theoretical justification for the practical limitation of quasi-static solvers and explains their dependence on the electrical size of the structure relative to the wavelength.

Low-frequency breakdown

Full-wave electromagnetic solvers are based on the complete set of Maxwell's equations and are designed to accurately capture high-frequency electromagnetic phenomena, including wave propagation, radiation, and full-field interactions. For

this reason, they represent the preferred modeling approach for electrically large structures and systems operating in radio-frequency and microwave regimes.

However, full-wave solvers also exhibit important limitations when applied to low-frequency or quasi-static problems. In particular, their accuracy and numerical robustness progressively degrade as the operating frequency decreases, leading to the so-called *low-frequency breakdown* problem [63]. In this regime, the numerical solution may become unreliable or severely ill-conditioned, despite the fact that Maxwell's equations remain physically valid.

The physical origin of the low-frequency breakdown can be directly understood by examining Ampère's law in the frequency domain:

$$\nabla \times \mathbf{H} = \mathbf{J} + j\omega\mathbf{D} = (\sigma + j\omega\varepsilon)\mathbf{E}. \tag{3.45}$$

This expression highlights the coexistence of two distinct contributions to the current density: the conduction current $\sigma\mathbf{E}$ and the displacement current $j\omega\varepsilon\mathbf{E}$.

At sufficiently high frequencies, the displacement current is comparable in magnitude to the conduction current, and the full-wave formulation provides a well-balanced description of the electromagnetic fields, accurately capturing propagation, radiation, and coupling effects. As the angular frequency ω decreases, however, the displacement current term becomes progressively smaller:

$$j\omega\varepsilon\mathbf{E} \ll \sigma\mathbf{E} \qquad \text{for } \omega \to 0. \tag{3.46}$$

In the low-frequency limit, Ampère's law therefore degenerates toward its quasi-static form,

$$\nabla \times \mathbf{H} \approx \sigma\mathbf{E}, \tag{3.47}$$

indicating that the physical behavior of the system transitions toward a magneto-quasi-static regime, even though the solver continues to employ a full-wave formulation.

From a numerical standpoint, this imbalance has significant consequences. Following spatial discretization, for instance through the finite element or integral equation method, the electromagnetic problem can be expressed in the generic

algebraic form

$$(\mathbf{K} + j\omega\mathbf{M})\,\mathbf{x} = \mathbf{b}, \tag{3.48}$$

where the matrix $\mathbf{K}$ is associated with curl operators and conduction-related terms, while $\mathbf{M}$ arises from the displacement current contribution. As the frequency decreases, the term $j\omega\mathbf{M}$ vanishes, and the resulting system matrix progressively loses numerical balance. This leads to strong linear dependencies among the unknowns, a rapidly increasing condition number, and a consequent deterioration of numerical stability, which collectively constitute the low-frequency breakdown phenomenon.

Physically, this breakdown reflects the fact that conventional full-wave formulations are inherently optimized to represent propagating electromagnetic fields with balanced electric and magnetic energy. At low frequencies, however, the dominant field behavior is governed by charge accumulation, current continuity, and quasi-static coupling mechanisms, which are only weakly enforced or indirectly represented in standard high-frequency formulations. As a result, the solver struggles to accurately capture the correct balance between irrotational and solenoidal field components.

Due to these limitations, full-wave solvers such as HFSS, while extremely effective for high-frequency analysis, are generally not well suited for DC or low-frequency electromagnetic simulations. Although they remain theoretically valid, their numerical implementation is not optimized to handle quasi-static field behavior efficiently or robustly, making their application to low-frequency power electronic problems impractical.

To overcome the low-frequency breakdown problem, several studies have proposed alternative formulations and numerical strategies specifically designed to preserve stability across a wide frequency range. These approaches typically involve reformulating Maxwell's equations in terms of potentials, separating conductive and dielectric unknowns, or directly manipulating the discretized system matrices through techniques such as block decomposition, constraint enforcement, or mixed field–potential formulations. However, such methods require explicit access to the system matrices, which is generally not provided by commercial electromagnetic solvers. Consequently, while these techniques can be applied to simple or canoni-

cal structures, practical simulations of complex geometries must rely on dedicated quasi-static solvers or hybrid modeling approaches.

Based on these considerations, a commonly adopted guideline is that quasi-static approaches provide accurate results when the characteristic dimension L of the structure satisfies the condition $L < \lambda/10$. In contrast, the use of full-wave solvers becomes necessary when this condition is no longer satisfied and propagation effects become significant. The direct application of full-wave formulations to DC or near-DC conditions is generally inefficient.

3.3 Commercial EM simulator tools

Based on the theoretical classifications discussed in the previous sections, commercial EM simulation tools can be systematically grouped according to the physical regime they model (quasi-static or full-wave), the dimensionality of the geometric representation (2.5D planar or full 3D), and the underlying numerical formulation. This classification is particularly relevant in electronic and power-electronics applications, where the choice of the EM solver must balance modeling accuracy, computational efficiency, and compatibility with circuit-level design workflows. A wide range of commercial EM tools is currently available, each optimized for specific frequency ranges, structure types, and application domains. Rather than providing a simple list, it is therefore useful to position each tool within a unified classification framework that highlights its strengths and limitations.

- Keysight PathWave provides several EM solvers primarily oriented toward RF and microwave applications. ADS (Advanced Design System) integrates a 2.5D Method of Moments (MoM) solver optimized for planar and multilayer structures, such as microstrip and stripline circuits. Although the solver is restricted to planar geometries, it resolves the complete set of Maxwell's equations for such structures and therefore operates as a full-wave planar solver. EMPro, on the other hand, is a general-purpose three-dimensional solver based on the Finite Element Method (FEM), with additional support for transient field simulations using time-domain techniques, making it suitable for broadband and radiating structures.

- The Ansys electromagnetic suite covers both quasi-static and full-wave regimes. Q3D Extractor is a three-dimensional quasi-static solver specifically designed for parasitic extraction in interconnects, PCBs, and semiconductor packages. By combining Boundary Element Methods (BEM) for AC parameters with FEM-based formulations for DC quantities, Q3D efficiently captures electrostatic and magnetostatic effects in electrically small structures. In contrast, HFSS is a full-wave 3D FEM solver that resolves the complete Maxwell equations and accurately models wave propagation, radiation, and resonant phenomena. HFSS also provides time-domain capabilities based on the Discontinuous Galerkin Time-Domain (DGTD) method for transient electromagnetic simulations. SIwave occupies an intermediate position, offering full-wave analysis under a 2.5D planar assumption, and is widely used for signal- and power-integrity analysis of large PCB structures.

- Cadence Design Systems offers a group of EM tools tightly integrated with its EDA environment. AWR AXIEM is a 2.5D MoM full-wave solver dedicated to planar RF structures, while AWR Analyst extends the analysis to full 3D using FEM. Clarity 3D Solver is a large-scale full-wave FEM tool with support for time-domain simulations. Sigrity represents a multi-solver platform rather than a single EM solver: depending on the module, it supports both quasi-static parasitic extraction (primarily for power-integrity and PDN analysis) and 2.5D full-wave modeling for high-speed signal-integrity applications. Consequently, Sigrity spans both quasi-static and full-wave regimes within a unified design environment.

- The Altair electromagnetic suite consists mainly of Flux and FEKO, which target different application domains. Altair Flux is a FEM-based solver focused on low-frequency and quasi-static electromagnetic problems, and is widely used for electric machines, inductors, transformers, and power magnetic components. It is particularly suited for EQS, MQS, and EMQS analyses. Altair FEKO, in contrast, is a general-purpose full-wave solver supporting MoM, FEM, and hybrid techniques, and is primarily employed for antennas, scattering, and electromagnetic compatibility (EMC/EMI) studies.

- COMSOL Multiphysics is a general-purpose FEM platform capable of performing both quasi-static and full-wave electromagnetic simulations, as well as coupled multi-physics analyses. Its flexibility allows it to address a wide variety of engineering problems; however, its general-purpose nature often results in higher modeling complexity and computational cost compared to application-specific EM tools, making it less common in routine parasitic extraction and EM–circuit co-simulation for electronic design.

- Finally, CST Studio Suite provides multiple EM solvers within a single environment. These include MoM-based solvers for planar multilayer structures, FEM solvers for frequency-domain full-wave analysis, and time-domain solvers based on the Finite Integration Technique (FIT) and the Transmission Line Matrix (TLM) method. CST is particularly strong in antenna design, broadband simulations, and EMC investigations.

Given the diversity of commercial EM simulation tools and the variety of modeling regimes they cover, a comparative overview is essential to clearly position each solver within the broader electromagnetic modeling landscape. To this end, Table 3.1 summarizes the most relevant commercial EM tools discussed above, classifying them according to their numerical formulation, electromagnetic modeling regime, and typical application domains.

This comparison provides a concise reference that highlights the fundamental differences between quasi-static, full-wave planar, and full-wave three-dimensional solvers. It also motivates the methodological choices adopted in the following of this work, in particular the focus on Ansys Q3D Extractor and Ansys HFSS for the analysis of PCB and semiconductor package parasitics in DC–DC power converters, where both quasi-static and full-wave effects must be considered in a complementary manner.

Table 3.1 Comparison of commercial electromagnetic simulation tools based on numerical formulation, modeling regime, and typical application domains.

Tool	**Numerical Method**	**Modeling Regime**	**Typical Applications**
Keysight ADS	MoM (2.5D), FEM	Quasi-static, Full-wave	RF and microwave planar circuits, multilayer PCB structures, EM–circuit co-simulation
Keysight EMPro	FEM, FDTD	Full-wave	General 3D EM analysis, antennas, transient field simulations
Ansys Q3D Extractor	BEM / FEM (hybrid)	Quasi-static	Parasitic RLCG extraction for interconnects, PCB, semiconductor packages, power electronics
Ansys HFSS	FEM, DGTD	Full-wave	High-frequency components, distributed interconnects, radiation and coupling analysis
Ansys SIwave	Hybrid solver (2.5D)	Full-wave	Signal and power integrity analysis for large PCB structures
Cadence Clarity	FEM, FDTD	Full-wave	Large-scale 3D EM problems, high-speed interconnects, advanced packaging
Cadence Sigrity	Hybrid solver (2.5D)	Quasi-static, Full-wave	Signal and power integrity in PCB and IC packaging
AWR AXIEM	MoM (2.5D)	Full-wave	Planar RF and microwave structures
AWR Analyst	FEM	Full-wave	General 3D EM analysis of RF components
Altair Flux	FEM	Quasi-static	Electric machines, magnetic components, inductors, transformers, low-frequency EM analysis
Altair FEKO	MoM, FEM, FDTD	Full-wave	Antennas, EMC/EMI, scattering, large-scale EM problems
COMSOL Multiphysics	FEM	Quasi-static, Full-wave	General-purpose multi-physics EM analysis, research-oriented simulations
CST Studio Suite	MoM, FEM, FIT/TLM	Full-wave	Antennas, EMC, high-frequency and time-domain EM simulations

In summary, the overview presented in this chapter highlights how EM simulation tools can be classified according to the numerical method employed, the geometric representation adopted, and the physical regime considered for solving Maxwell's equations. The Method of Moments and the Finite Element Method constitute the main numerical approaches addressed in this dissertation. With regard to geometric modeling, EM solvers can be classified according to whether they employ 2D, 2.5D, or full 3D representations. In the context of the analyses considered in this work, 2.5D and full 3D representations are of primary interest, as they allow the geometric features and interconnections of PCB and package structures to be represented. Likewise, solvers may operate under quasi-static or full-wave assumptions, each being applicable within specific frequency ranges and electromagnetic conditions. Once the most appropriate solver has been selected, the simulation workflow described in Section 3.1 can be followed to systematically build, analyze, and validate the EM model of the structure under investigation.

Chapter 4

Electromagnetic Modeling and Parasitic Extraction of Interconnect Systems

The results presented in this chapter are adapted from published articles P2, P3, P4 and P5.

In the previous chapter, simulation tools suitable for EM analysis have been introduced, together with their theoretical foundations and practical capabilities. Building upon this background, the present chapter focuses on their application to the EM modeling and parasitic extraction of interconnect systems. The objective is to establish a systematic workflow that enables the transition from the physical geometry of a structure to an equivalent electrical model, suitable for circuit-level simulations, specifically, in the time domain. In particular, the analyses presented in this work are conducted using Ansys simulation environments, with port definition and simulation settings described in Sections 4.1.1 and 4.2.1 for Q3D and HFSS, respectively. These tools enable the investigation of EM behavior over a wide frequency spectrum, ranging from quasi-static conditions to fully dynamic wave propagation regimes. In this context, the choice of the appropriate simulation approach is dictated by the electrical characteristics of the system under study, including its physical dimensions, operating frequency range, and required level of modeling accuracy.

The first part of this chapter is devoted to quasi-static EM analysis, performed using the Q3D Extractor tool. This approach relies on the quasi-static assumption and is therefore suitable for structures whose dimensions are significantly smaller than the wavelength associated with the highest frequency of interest, as previously discussed. Within this framework, the fundamental concepts underlying the simulation setup are introduced, including the definition of ports and their role in the extraction of equivalent electrical parameters [64–69]. The procedure adopted for EM simulation is outlined, including DC and AC analyses, as well as the resulting frequency-dependent representation of the extracted parameters [70–72]. Particular attention is given to the modeling of frequency-dependent effects, with specific reference to the skin effect. Advanced techniques aimed at improving computational efficiency and accuracy are presented. These methods enable the optimization of the simulation process and support the generation of compact models, which can be effectively employed in time-domain circuit simulations.

In the second section, the focus shifts to full-wave EM simulations, carried out using HFSS. Unlike quasi-static methods, full-wave solvers account for the complete set of Maxwell's equations, as detailed in earlier sections. This approach becomes essential when dealing with electrically large structures, high-frequency operation, or configurations where distributed effects cannot be neglected. Therefore, the use of HFSS for EM modeling is described, including the setup of the simulation environment, boundary conditions and excitation methods. The extraction of frequency-domain responses, in the form of scattering parameters, is discussed with the procedure for deriving the corresponding parasitic values. The approach adopted for co-simulation differs from that used in Q3D, as the port used in the full-wave simulations does not allow voltages to be referenced to a common ground node. Consequently, a methodology is introduced to overcome this limitation and obtain a complete model for time-domain analysis.

The final part of the chapter addresses broadband modeling techniques. Particular emphasis is placed on the differences between quasi-static and full-wave results in terms of modeling capabilities. To this aim, methods for the reliable measurement of very low impedance values are presented, enabling a valid comparison between the two approaches. Starting from these considerations, broadband models are developed to accurately characterize parasitic behavior across a wide frequency range. This

approach is particularly relevant for power electronic systems, where switching transients and harmonics may extend over several decades of frequency. Finally, the procedure for generating the broadband model and translating it into an accurate time-domain netlist is described, thereby enabling its integration into circuit-level simulations.

4.1 Quasi-static analysis

The simulation methodology is first presented, detailing the procedures adopted for the extraction of parasitic inductances and resistances required by advanced electromagnetic and circuit-level modeling techniques. Particular attention is devoted to strategies aimed at reducing simulation time and computational cost in PCB–package co-design, while preserving modeling accuracy. Furthermore, equivalent modeling approaches are introduced to improve numerical stability, convergence, and efficiency in time-domain simulations, enabling reliable analysis of complex electronic systems.

4.1.1 Port Definition and Simulation Settings

EM simulation tools relying on quasi-static formulations follow a structured sequence of computational steps. The corresponding workflow implemented in Q3D can be summarized as follows [73–78].

- **Geometry Definition**: The first stage consists in the construction of the three-dimensional representation of the device under test. The geometry may be created directly within the Q3D interface or imported from external computer-aided design (CAD) tools. During this phase, all conductors, dielectric layers, insulating regions, and material properties must be defined.
- **Net Assignment and Terminal Definition**: once the physical structure is defined, electrical connectivity is established through the assignment of nets, each representing a group of conductors belonging to the same electrical path. Q3D requires the explicit definition of terminals, which are limited to two

types *Sources* and *Sinks*. These terminals identify the locations where current enters and exits a given net. Each net must include at least one Source and one Sink. Terminals are defined by selecting either a two-dimensional sheet object (such as a rectangle) or a face of a three-dimensional conductor. Typical choices include the end faces of conductor traces, a representation of these terminals is presented in Fig(4.1).

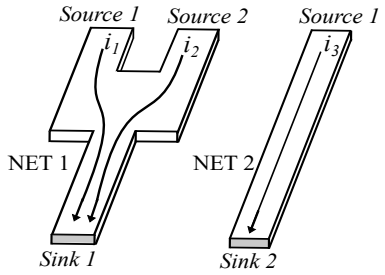


Fig. 4.1 Schematic representation of Source and Sink terminals in Q3D.

- **Solver Selection and Analysis Setup**: three independent solvers are present, Capacitance–Conductance (CG), DC RL, and AC RL, each dedicated to the extraction of specific parasitic parameters.

  – *The CG solver*: computes capacitances and dielectric conductances using a surface mesh approach and accounts for dielectric dispersion effects.

  – *The DC RL solver*: employs a volumetric finite element mesh to calculate the DC resistance directly, while inductance is obtained through post-processing.

  – *The AC RL solver*: captures frequency-dependent phenomena, such as the skin effect, using a surface mesh to compute inductance, with resistance again evaluated as a post-processing quantity.

  Each solver operates independently, maintaining its own mesh, convergence criteria, and solution database. The user specifies the solution type, which determines the required accuracy, tolerance limits, and refinement depth. Key adjustable parameters include:

  – *relative error thresholds*, defining the maximum allowable variation between consecutive adaptive passes;

  - *maximum number of adaptive passes*, which limits the extent of mesh refinement;
  - *frequency points*, which can be defined as a discrete set or as a sweep over a specified frequency range.

  These settings directly influence both computational cost and extraction accuracy. Increasing the number of frequency points improves the resolution of the extracted R, L, C, and G profiles, at the expense of longer simulation times.

- **Post-Processing and Parameter Extraction**: upon completion of the simulation, Q3D provides frequency-dependent curves for resistance, inductance, capacitance, and conductance. Additionally, electric and magnetic field distributions can be visualized, allowing inspection of current paths, localized hotspots, and coupling mechanisms.

The quasi-static extraction approach adopted by Q3D relies on the frequency-dependent redistribution of current within conductive materials. This behavior is governed by the skin effect, which represents the underlying physical mechanism used to distinguish different frequency regimes in the analysis.

The skin effect describes the tendency of alternating current to concentrate near the surface of a conductor as frequency increases, leading to a non-uniform current density across the conductor cross section. The characteristic penetration depth of the current, commonly referred to as skin depth, is modeled in Q3D according to the following formulation [73]

$$\delta = \sqrt{\frac{2}{\omega \sigma \mu_0 \mu_r}}, \tag{4.1}$$

where $\omega = 2\pi f$ is the angular frequency, σ is the electrical conductivity of the conductor material, μ_0 is the permeability of free space, and μ_r is the relative permeability of the conductor.

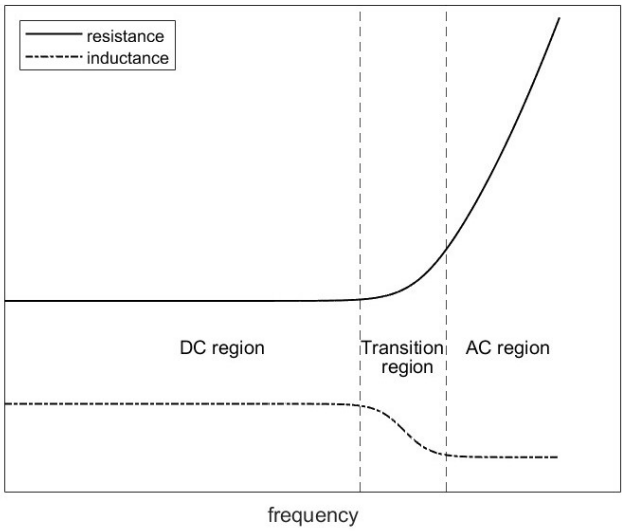


Fig. 4.2 Resistance and inductance behavior due to the skin effect and division of the frequency range into DC region, transition region and AC region.

Based on the conductor dimensions and material properties, Q3D automatically partitions the simulation frequency range into three distinct regions: a low-frequency (DC) region, a transition region, and a high-frequency (AC) region, as illustrated in Figure 4.2. This subdivision reflects the progressive evolution of current distribution within the conductor as frequency varies.

For a conductor of thickness d, the onset of the high-frequency AC region is defined as the frequency at which the skin depth becomes much smaller than the conductor thickness. Under this condition, current is confined to a thin layer near the conductor surface, and the starting frequency of the AC regime is given by

$$f_{\text{AC,limit}} = \frac{9}{\sigma \pi d^2 \mu_0 \mu_r}. \tag{4.2}$$

Conversely, the upper bound of the DC region corresponds to frequencies for which the skin depth remains larger than the conductor thickness, ensuring an approximately uniform current distribution over the entire cross section. This upper DC limit is expressed as

$$f_{\text{DC,limit}} = \frac{1}{\sigma \pi d^2 \mu_0 \mu_r}. \tag{4.3}$$

Within the DC region, both resistance and inductance exhibit an approximately constant behavior up to $f_{\mathrm{DC,limit}}$, as current uniformly penetrates the conductor cross section. In the AC region, the confinement of current near the conductor surface reduces the effective cross-sectional area available for conduction. As a result, resistance increases proportionally to the square root of frequency, while inductance decreases and asymptotically approaches a constant value as frequency increases.

Between the DC and AC regimes, a transition region is identified. In this interval, resistance and inductance values are estimated through interpolation between the respective DC and AC asymptotic behaviors. This approach ensures a smooth and physically consistent variation of the extracted parasitic parameters across the entire frequency range.

4.1.2 Derivation of parasitic inductance and resistance

As discussed in the previous section, electrical connectivity in Q3D is established through the definition of nets and the associated Source and Sink terminals. Building upon this terminal-based description, Q3D internally maps each Source–Sink pair onto a corresponding port representation. For each Source and each Sink defined within the model, a port is automatically generated by the simulator. These ports collectively define a multiport network, for which a complete scattering matrix is computed across the specified frequency range.

For each individual net, the corresponding inductance and resistance values between the designated source node and each associated sink node can be extracted by processing the simulated frequency data. In particular, the S-parameters obtained from the electromagnetic solver are first transformed into the impedance matrix (Z-parameters), which provides a direct representation of the network voltage and current relationships. Once the Z-matrix is available, the electrical behavior of a specific source–sink pair can be isolated by applying appropriate termination conditions. This is achieved by short-circuiting the terminal of the selected sink node to ground, thereby allowing the impedance seen from the source node to be evaluated under controlled boundary conditions. The procedure is illustrated in Figure 4.3(a), where the grounding of the sink terminal enables the determination

of both the effective resistance and the inductive contribution associated with the corresponding current path.

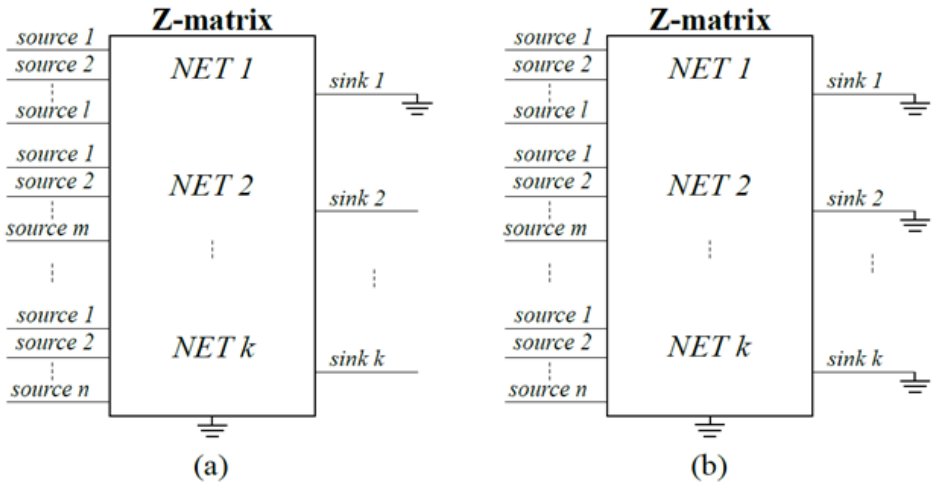


Fig. 4.3 Z-matrix converted from S-matrix obtained from electromagnetic simulation. (a): closing alternately the sink of each net to GND to compute the parasitic values of that net, (b): closing sink of every net to GND to compute the parasitic values between different nets.

For each net, the direct values of parasitic inductance and resistance between a source and sink defined in that same net (self-inductance and self-resistance) are obtained by considering the imaginary part $\Im(\cdot)$ and real part $\Re(\cdot)$ of the corresponding element of the modified impedance matrix as:

$$L_{i,i} = \frac{\Im\left(Z_{\mathrm{mod}(i,i)}\right)}{2\pi f}, \qquad R_{i,i} = \Re\left(Z_{\mathrm{mod}(i,i)}\right). \tag{4.4}$$

Whereas for the parasitic components defined between different sources on the same net (mutual inductance and mutual resistance), we have:

$$L_{i,j} = \frac{\Im\left(Z_{\mathrm{mod}(i,j)}\right)}{2\pi f}, \qquad R_{i,j} = \Re\left(Z_{\mathrm{mod}(i,j)}\right). \tag{4.5}$$

Here, Z_{mod} represents the appropriately modified impedance matrix.

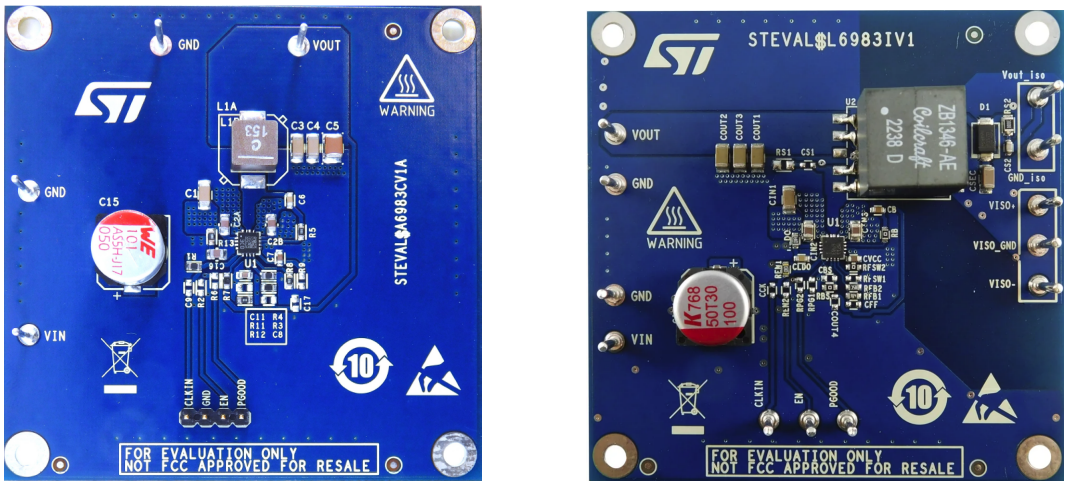
Conversely, it is also possible to evaluate the parasitic resistances and inductances between different sources belonging to different nets (mutual inductance and mutual

resistance). In this case, the matrix is computed as illustrated in part (b) of Figure 4.3. All sinks of the nets are connected to ground, and the analysis focuses exclusively on the mutual parasitic resistance and inductance between terminals belonging to different nets.

Consequently, the direct extraction of the S-parameter matrix from Q3D provides an efficient means to characterize the frequency-dependent parasitic behavior of the structure under analysis. By post-processing the simulated network parameters, the relevant resistance and inductance contributions can be readily derived over the frequency range of interest, enabling their direct assessment for the intended analyses.

4.1.3 Co-simulation between PCB and PKG

In high-performance synchronous buck converters, the switching behavior is critically influenced by the parasitic elements associated with the power delivery path, as discussed in the previous chapter, and these are directly related to the way in which the converter is physically realized. Representative examples of modern power conversion systems are provided by commercial evaluation platforms such as the STEVAL-A6983CV1 in Fig. 4.4(a) or the STEVAL-L6983IV1 in Fig. 4.4(b), developed by STMicroelectronics. These systems integrate a fully functional synchronous buck converter on a PCB, where the power stage is implemented using a monolithic integrated circuit (IC) housed in a dedicated semiconductor package (PKG). The considered platform reflects a typical implementation of a compact switching converter, in which the power MOSFETs and the gate drivers are fully integrated within the device PKG, while passive components and interconnections are realized on the PCB. This architectural partitioning inherently results in a contribution of parasitic elements across two physically distinct but electromagnetically coupled domains [79–96].



(a) (b)

Fig. 4.4 STMicroelectronics evaluation board based on (a) DC-DC converter buck regulator A6983CQTR (STEVAL-A6983CV1) and (b) synchronous iso-buck converter L6983I (STEVAL-L6983IV1).

From an EM standpoint, the most critical contribution arises from the high-current switching loop, as outlined in the previous chapter, which includes the input decoupling capacitor, the internal power switches, and the associated return path. Since this loop inherently spans both the PCB and the semiconductor device PKG, its behavior is governed by a tightly coupled EM system. As a result, the interaction between these two regions plays a dominant role during fast switching transients in shaping key phenomena such as voltage overshoot at the switching node and current ringing. More specifically, these effects strongly depend on the spatial distribution of current and return paths, which extend through PKG interconnects (bond wires or bumps, lead frames) and PCB structures (vias and traces). The close proximity between conductors belonging to different structures gives rise to significant coupling effects, which modify the effective impedance of the switching loop and can introduce resonant modes involving both PCB and PKG parasitics. As a consequence, the effective loop inductance cannot be uniquely partitioned into separate PCB and PKG contributions, but instead results from their combined EM interaction. Neglecting this coupled behavior by treating the PCB and the PKG as independent subsystems leads to an incomplete representation of the underlying physics. A comprehensive analysis therefore requires a modeling approach capable of capturing the combined frequency-dependent EM behavior of the entire structure.

Different approaches can be adopted to address this problem using EM simulators, as presented in the following sections. Each is analyzed in terms of its underlying principles, together with its advantages and limitations.

Full model

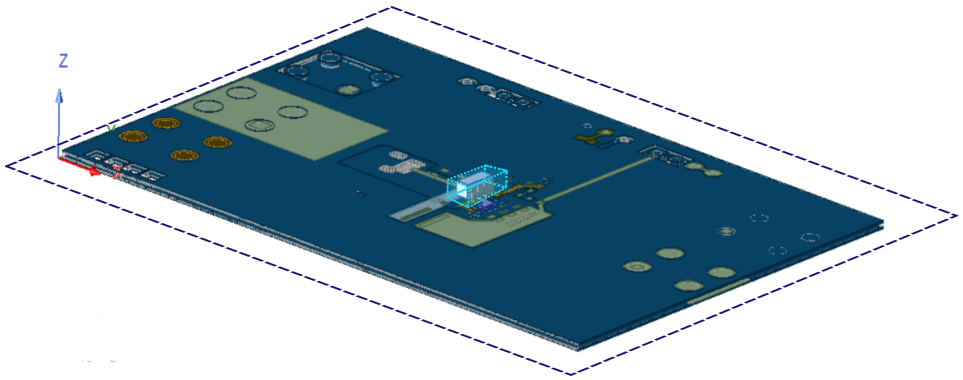


Fig. 4.5 Q3D simulation of the whole system constituted of PCB highlighted in dark blue and PKG in light blue.

The most comprehensive approach consists in performing an EM simulation of the combined PCB–PKG structure, in this case using Q3D as EM solver as illustrated in Fig. 4.5. By modeling both domains within a single simulation environment, all parasitic elements are inherently taken into account together with their spatial distribution and mutual coupling, the complete EM behavior is captured, allowing the model to consider the complete set of interactions.

Despite its accuracy, this approach presents significant computational challenges. In EM simulations, the required computational resources are strongly dependent on the number of unknowns used to describe the system. Denoting this number by N, it generally increases with the geometrical complexity of the model, the amount of detail included in both the PCB and the PKG, and the resolution adopted in the discretization process. When both domains are simulated together, the size of the model grows. In addition to the elements of the PCB, such as traces, vias, and planes, the simulation must also include the structure of the PKG, involving interconnects, routing, and material interfaces. This results in a substantial increase in the number of geometrical elements to be discretized. A finer mesh is required to accurately

resolve small geometrical features and to correctly capture frequency-dependent effects. However, increasing the mesh density leads to a rapid growth in the number of unknowns, which directly impacts both memory usage and simulation time.

To mitigate this issue, EM solvers generally allow the discretization to be refined non-uniformly, with finer elements introduced only in regions where a higher spatial resolution is required. In Q3D, adaptive mesh refinement can therefore be used to locally increase the discretization density around geometrically critical regions while maintaining a coarser mesh elsewhere. Although this approach can significantly reduce the number of discretization elements compared with a uniformly fine mesh, it does not fully eliminate the computational challenges associated with the simulation of the complete PCB-PKG assembly. The combined model still involves a larger number of unknowns and electromagnetic coupling interactions that must be simultaneously accounted for by the numerical solver. More generally, the computational cost of EM simulations exhibits a non-linear dependence on the size of the numerical problem. In MoM formulations, the interactions among the discretized elements lead to a dense system matrix. For an $N \times N$ matrix, its construction and storage require $\mathscr{O}(N^2)$ computational effort and memory, respectively. The solution of the resulting linear system further introduces a significant computational cost, a direct solver requires $\mathscr{O}(N^3)$ time to solve the system of equations, whereas a conventional iterative solver requires $N_{\text{itr}}\mathscr{O}(N^2)$ operations for N_{itr} iterations [97]. Instead, in FEM formulations, the solution of a three-dimensional problem scales as $\mathscr{O}(N^2)$ [98].

Consequently, even when adaptive meshing limits the increase in discretization density, the simulation of the complete PCB–PKG structure may still require substantially greater memory resources and longer solution times than the separate analysis of the individual domains. This computational burden motivates the investigation of alternative simulation strategies aimed at reducing the complexity of the EM problem while retaining the relevant parasitic effects and electromagnetic interactions between the two domains.

Cascade method

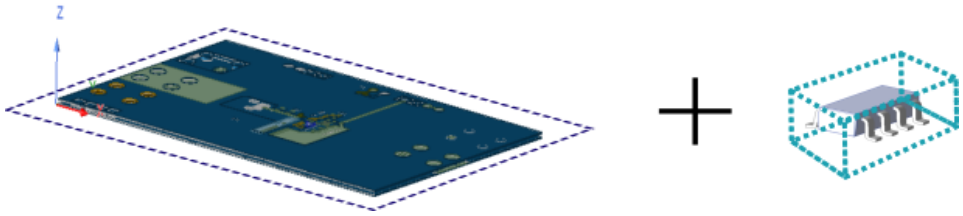


Fig. 4.6 EM simulation of the two separate system and cascade of the obtained results.

To mitigate the high computational cost associated with full-system EM simulations, an alternative approach consists in simulating the PCB and the PKG separately, as represented in Fig. 4.6 and subsequently integrating their results. This strategy enables a significant reduction in computational load while still allowing a system-level description of the parasitic behavior. The underlying principle is to partition the overall structure into two distinct domains, corresponding to the PCB and the PKG, which are analyzed independently. In each case, the parasitic elements are extracted separately, resulting in reduced model complexity and improved simulation efficiency.

The two resulting subnetworks must then be combined to reconstruct the behavior of the complete system. While scattering parameters provide an effective representation of an n-port network in terms of incident and reflected waves, and are particularly suitable for measurement and EM-based characterization, they are not convenient for analyzing cascaded two-port networks. This limitation arises from the fact that the S-parameter formulation does not directly relate the input and output variables in a form that can be easily combined across multiple interconnected stages. To overcome this limitation, alternative network representations are adopted. In particular, transmission-based formulations, such as the T-matrix (or equivalently ABCD parameters), establish a direct relationship between the input and output quantities of a two-port network. This representation is inherently suited for cascaded structures, as it enables the overall response of multiple interconnected networks to be obtained through a straightforward matrix multiplication.

In particular, when considering a two-port representation of the system, the transmission (T-) parameters can be defined in terms of incident and reflected waves as:

$$\begin{bmatrix} b_1 \\ a_1 \end{bmatrix} = \begin{bmatrix} T_{11} & T_{12} \\ T_{21} & T_{22} \end{bmatrix} \begin{bmatrix} a_2 \\ b_2 \end{bmatrix}. \tag{4.6}$$

In contrast, the ABCD parameters describe the network behavior in terms of port voltages and currents, as illustrated in Fig. 4.7.

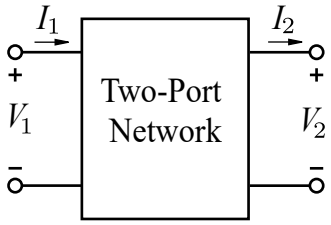


Fig. 4.7 Representation of a two-port network.

In this representation, the relationship between the electrical variables at the input and output ports is expressed as:

$$\begin{bmatrix} V_1 \\ I_1 \end{bmatrix} = \begin{bmatrix} A & B \\ C & D \end{bmatrix} \begin{bmatrix} V_2 \\ I_2 \end{bmatrix}. \tag{4.7}$$

Therefore, considering $\mathbf{T}_1$ and $\mathbf{T}_2$ as the transmission matrices describing the first and second subsystems, respectively, the overall network is given by:

$$\mathbf{T}_{\text{tot}} = \mathbf{T}_1 \cdot \mathbf{T}_2, \tag{4.8}$$

an analogous relationship holds for the ABCD representation.

Implementing this framework in MATLAB, multi-port networks can be cascaded using the dedicated functions `cascadesparams`, which enables the direct combination of individual S-parameter representations into an overall cascaded network.

This decoupled approach offers significant advantages in terms of computational efficiency and scalability, particularly for large multi-domain systems where a com-

plete EM co-simulation would be computationally prohibitive. By partitioning the structure into separate PCB and PKG models, each subproblem can be solved independently, leading to a substantial reduction in simulation complexity and overall computational cost. However, these benefits come at the expense of modeling approximations introduced during the partitioning process. The accuracy of the final system representation strongly depends on the quality of the parasitic extraction and on the validity of representing inter-domain interactions. The main limitation of this methodology therefore lies in the trade-off between computational efficiency and physical accuracy. While the approach is well suited for system-level analysis and design iteration, it requires careful validation of the extracted parasitic parameters, since some interaction can be neglected.

Segmentation and recombination method

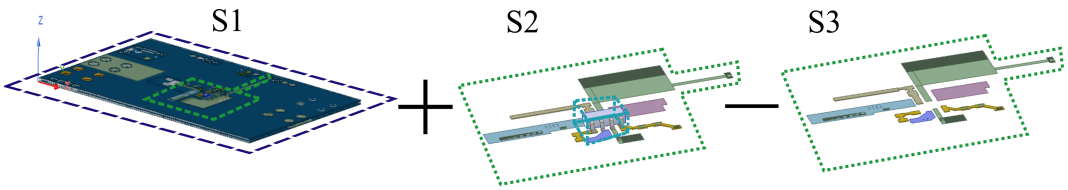


Fig. 4.8 Simulation of PCB (S1), simulation of PKG+signal traces connected to it (S2), and simulation of signal traces only (S3).

The need to balance simulation accuracy with computational efficiency motivates the adoption of a structured EM simulation strategy. The proposed method is based on three distinct simulations as reported in Fig. 4.8, designed to isolate and reconstruct the parasitic contributions associated with the PCB, the PKG, and their mutual interaction.

- The first simulation (S1 in Fig. 4.8) considers the PCB alone, and is used to extract the parasitic elements associated exclusively with the PCB layout, that includes traces and vias.
- In the second simulation (S2 in Fig. 4.8), the PKG is introduced together with the PCB traces, while excluding the PCB substrate, therefore approximating the model but simplifying the EM problem. This configuration captures the

combined EM behavior of the PKG–PCB traces, including both individual contributions and interaction effects between the two structures.

- The third simulation (S3 in Fig. 4.8) is performed on the PCB traces alone, with the substrate removed. This case is used to isolate the parasitic contribution of the copper routing independently of the dielectric environment.

Once the three EM simulations are completed, the corresponding parasitic contributions can be systematically combined to isolate and selectively analyze the different physical effects. Within this scope, the model can be treated as a linear time-invariant (LTI) system. This assumption follows from the use of linear material properties and from the the absence of any explicit time dependence in the system parameters. In particular, linear constitutive relations are assumed for the materials,

$$\mathbf{D} = \varepsilon \mathbf{E}, \qquad \mathbf{B} = \mu \mathbf{H}, \qquad \mathbf{J} = \sigma \mathbf{E}, \tag{4.9}$$

where the material parameters are constant and independent of time.

In general, a system is linear if the response to a linear combination of input excitations,

$$x(t) = a x_1(t) + b x_2(t), \tag{4.10}$$

is given by the corresponding linear combination of the individual responses,

$$y(t) = a y_1(t) + b y_2(t), \tag{4.11}$$

where $y_1(t)$ and $y_2(t)$ denote the responses to $x_1(t)$ and $x_2(t)$, respectively.

While on the other side, a system is time-invariant if a temporal shift applied to the input signal produces an identical delay in the corresponding output, without altering its shape,

$$\text{if } x(t) \to y(t), \quad \text{then } x(t - t_0) \to y(t - t_0), \tag{4.12}$$

where t_0 is an arbitrary time shift.

Therefore, the representation of the system as an LTI model guarantees the applicability of the superposition principle. Furthermore, the quasi-static formulation

adopted under low-frequency approximations allows the decomposition of the EM response into distinct parasitic contributions, which can be independently extracted and consistently recombined.

By subtracting the trace-only contribution (S3) from the combined PCB–PKG simulation (S2), the contribution associated with the PKG and its interaction with the PCB is isolated. This operation removes the effect of the PCB traces alone while preserving the interaction with the simplified PCB structure. The intrinsic parasitics of the PCB structure are instead obtained from the PCB-only simulation (S1). As a result, the overall parasitic model can be reconstructed by combining the isolated PCB contribution with the PKG-related and interaction terms extracted from the previous step.

To correctly combine and separate the contributions obtained from the S-parameters of the individual EM simulations, the procedure previously introduced for extracting the resistive and inductive parasitic elements from Q3D results is adopted. In particular, the S-parameters are first converted into the corresponding modified Z-matrix, in Fig. 4.3, from which the equivalent R and L contributions are derived for each simulation. By applying the reduction of the Z-matrix as described, only the quantities of interest are retained. This enables the matrices associated with each configuration to be directly combined through addition and subtraction. In particular, the matrix derived from S1 is added to that obtained from S2, while the contribution associated with S3 is subtracted. The resulting matrix is then used to derive the final R and L parasitic parameters according to the proposed methodology.

Comparison of Modeling Strategies

The explained method is applied to the simulation of the model of PCB and PKG in Fig 4.8 with the quasi static-solver Q3D. Results are compared to the case of the simulation of the complete system which takes into account all the interactions between PCB and PKG, and to the most widespread method, i.e., the case of cascading PCB and PKG considering transmission parameters. Terms of comparison are the simulation time of each block according to the methodology adopted, and the accuracy computed by means of the maximum relative error between the resistance (or inductance) computed with the approximated method and with the full simulation,

and averaged for the different considered cases. Data are collected in Table 4.1. It is possible to observe that the simulation time of the proposed method is similar with that of the cascade one, and significantly reduced compared to the whole system simulation, decreasing the resource effort required by the electromagnetic simulation. Furthermore, with the proposed approach, the parasitic effect between PCB and PKG is not completely neglected, as it happens in the case of the cascade approach, but it is possible to obtain an accuracy comparable to the full method.

Table 4.1 Performance comparison between the full sistem simulation, the standard cascade approach and the proposed approach.

Methodology	**Accuracy**	**Simulation**	**Time**
Full system	100%	PCB+PKG	32h5min
Cascade	74%	PCB	18h18min
		PKG	6min
Proposed	90%	PCB	18h18min
		PKG+Traces	14min
		Traces	10min

The values of parasitic inductances and resistances are computed for the case of the whole simulation, the cascade, and the proposed one starting from the electromagnetic simulation results. Parasitic inductance and resistance between sink and source in the same net, considering two nets, are represented in Figure 4.9. Parasitic inductance and resistance between sources on the two different nets previously considered are depicted in Figure 4.10.

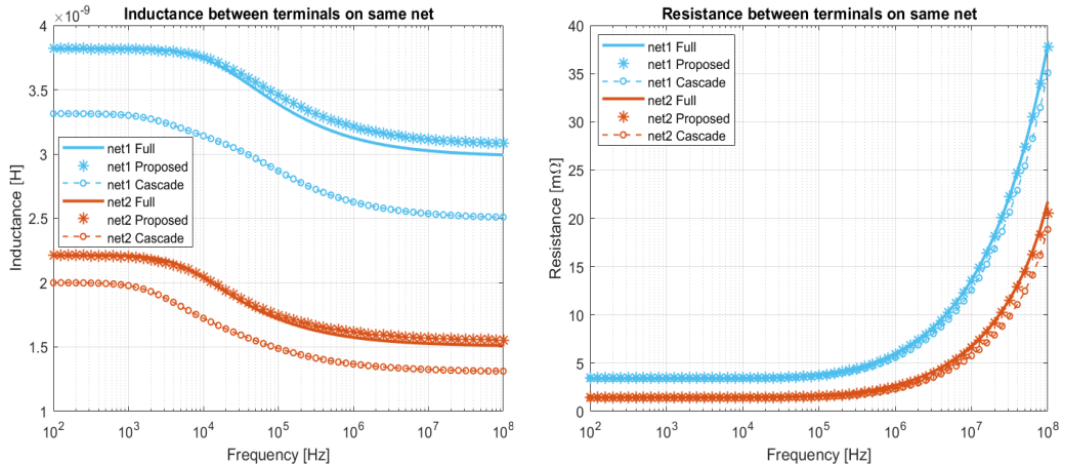


Fig. 4.9 Comparison between (self) parasitic inductance and (self) resistance on the same net (computed for source1 on net1 and for source1 on net2) starting from Z-matrix (a) using the three different methods explained.

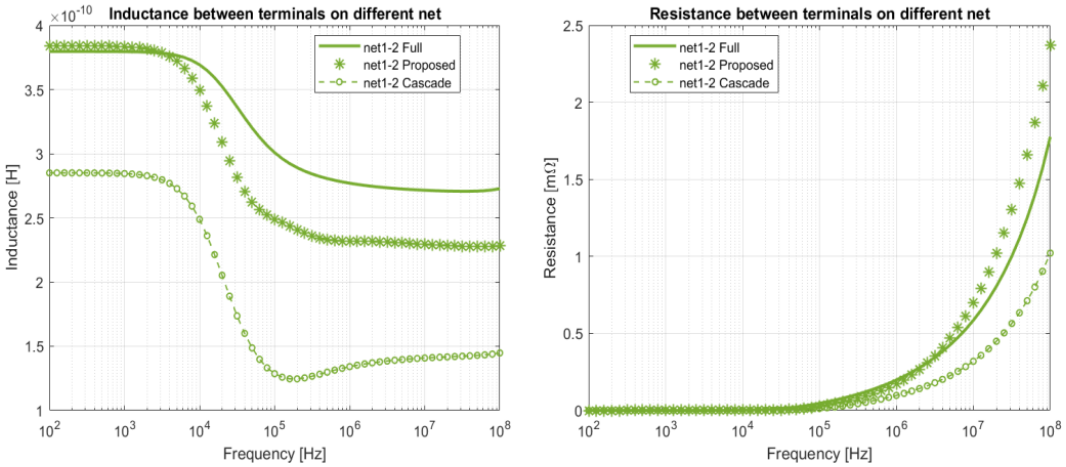


Fig. 4.10 Comparison between (mutual) parasitic inductance and (mutual) resistance between two sources on different nets (from source1 on net1 to source1 on net2) obtained starting from Z-matrix (b) using the three different methods explained.

From the comparison it is possible to observe that with the segmentation and recombination methodology a good fitting of the parasitic components with the entire system simulation is obtained, in particular at low frequencies they totally overlap, showing an improvement compared to the simple cascade case.

4.1.4 Time-domain model

After performing the EM simulation, the extracted parasitic information must be incorporated into circuit-level simulations in the time domain. This step is essential, as the accurate analysis of SMPS, such as buck converters, fundamentally relies on time-domain simulations capable of capturing switching phenomena, transient dynamics, and the resulting voltage and current ripple. However, EM simulations provide results in the frequency domain, either as network parameters (e.g., S-parameters) or as frequency-dependent representations of parasitic elements (R, L, C, and G), which can be directly visualized as a function of frequency in Q3D. In contrast, the final target of the modeling process is their integration into SPICE-like circuit simulators, which operate in the time domain and require equivalent circuit representations. Therefore, a key step in the modeling flow consists in transforming the EM-extracted frequency-domain data into a circuit model that can be directly implemented within a SPICE environment. This transformation must preserve fundamental physical properties such as causality and passivity, which are intrinsic to any physically realizable interconnect [99–107].

Causality expresses the fundamental temporal constraint that the system response at any given time instant cannot depend on future values of the excitation. Accordingly, a system is causal if it reacts only to present and past inputs, and never anticipates events that have not yet occurred. This concept can be formally characterized by the following theorem.

Theorem 4.1.1. *[108] A system is causal if and only if for every input* $\mathrm{x}(t)$ *that vanishes for* $t < t_0$*, the corresponding output signal* $\mathrm{y}(t)$ *also vanishes for all* $t < t_0$*.*

When restricting attention to LTI systems, the general definition of causality leads to the following condition on the impulse response.

Theorem 4.1.2. *[108] An LTI system is causal if and only if all the elements* $h_{ij}(t)$ *of its impulse response matrix* $\mathbf{h}(t)$ *are vanishing for* $t < 0$*, i.e.,*

$$\mathbf{h}(t) = \mathbf{0} \qquad \textit{for all } t < 0, \tag{4.13}$$

where $\mathbf{h}(t)$ *denotes the impulse response matrix of the system.*

Although EM solvers inherently describe causal physical structures, numerical representations obtained from sampled frequency data or approximate fitting procedures may unintentionally violate this condition if causality is not explicitly enforced. These violations typically result in non-physical responses in the reconstructed time-domain behavior.

Passivity, on the other hand, expresses the property that a system cannot generate energy internally, but it can only store or dissipate the energy supplied by external sources. In the time domain, an N-port network described in terms of port voltages $\mathbf{v}(t)$ and currents $\mathbf{i}(t)$ is said to be passive if the net energy absorbed by the network satisfies

$$\int_{-\infty}^{t} \mathbf{v}^{\mathsf{T}}(\tau)\,\mathbf{i}(\tau)\,d\tau \;\geq\; 0, \qquad \forall t. \tag{4.14}$$

where $(\cdot)^{\mathsf{T}}$ denotes the transpose of the vector. This condition constitutes the fundamental physical definition of passivity, as it is a direct consequence of the principle of energy conservation, which implies that a system cannot supply more energy than it has previously absorbed. For the systems described in terms of scattering parameters, it is convenient to work with incident and reflected waves at the ports, denoted respectively by $\mathbf{a}(t)$ and $\mathbf{b}(t)$. With an appropriate normalization, the squared norms of these quantities correspond to the instantaneous incident and reflected powers. Passivity then requires that

$$\int_{-\infty}^{t} \left(\mathbf{a}^{\dagger}(\tau)\mathbf{a}(\tau) - \mathbf{b}^{\dagger}(\tau)\mathbf{b}(\tau)\right) d\tau \;\geq\; 0, \qquad \forall t, \tag{4.15}$$

where $(\cdot)^{\dagger}$ denotes the conjugate transpose. This inequality implies that the total reflected energy cannot exceed the total incident energy. When the system is LTI, passivity admits an equivalent frequency-domain formulation in terms of the scattering matrix. In this case, energy conservation is expressed by

$$\mathbf{S}^{\dagger}(\omega)\,\mathbf{S}(\omega) \;\leq\; \mathbf{I}, \qquad \forall\, \omega. \tag{4.16}$$

where ω denotes the angular frequency and $\mathbf{S}(\omega)$ represents the value of the scattering matrix of the network.

The requirements in equations (4.14) and (4.15) can be interpreted in terms of energy exchange between the system and its environment. In particular, they require

that the cumulative net energy absorbed by the system remains positive at every time instant. This implies that, over any time interval, the system cannot deliver more energy than it has previously received. As a consequence, any energy dissipation or power delivery at the external ports must be preceded by a corresponding phase of energy storage or absorption within the system. Equivalently, energy release is only admissible after an amount of energy has been accumulated internally. A system that violates this temporal ordering by exhibiting energy generation prior to absorption, does not satisfy the passivity conditions. From this viewpoint, passivity imposes strong constraints on the temporal structure of the system response and excludes any form of anticipative behavior. This observation leads to the following result.

Theorem 4.1.3. *[108]*

If a linear time-invariant system is passive, then it is necessarily causal.

This result has important implications from a modeling perspective. Since, for linear time-invariant systems, passivity defined in a rigorous energetic sense guarantees causal behavior, any violation of passivity in an extracted or approximated model may also lead to noncausal responses in the time domain. Such inconsistencies compromise the physical validity of the model and may result in numerical instabilities when the model is employed in transient simulations. In practice, numerical model extraction and approximation procedures based on frequency-domain electromagnetic data do not inherently preserve either passivity or causality. This limitation becomes particularly critical when the resulting interconnect models are embedded within SPICE-like transient analyses and interact with nonlinear circuit elements, such as switching devices. In these conditions, even small violations of physical constraints may trigger numerical divergence or spurious oscillatory behavior, severely affecting simulation robustness. For this reason, the synthesis of equivalent circuit representations from EM-extracted frequency-domain data must be carried out with particular care, ensuring that both passivity and causality are explicitly enforced. Preserving these properties is essential to obtain time-domain models that are physically meaningful, numerically stable, and reliable when integrated into larger system-level simulations.

Several techniques have been developed to perform this transformation, ranging from simple single-frequency parameter extraction to more advanced and physically

consistent modeling approaches. The main difference between these approaches lies in the trade-off between simplicity, computational efficiency, and accuracy over a given frequency range. In the following sections, these methodologies are introduced in increasing order of complexity, beginning with single-frequency RLCG extraction, progressing to ladder-network representations, and finally addressing broadband passive macromodeling techniques.

Single-frequency RLCG model

The simplest approach for deriving an equivalent circuit representation from EM simulation data consists in the extraction of lumped resistance, inductance, capacitance, and conductance parameters at a single frequency. Within this methodology, the interconnect is modeled as a RLCG network whose parameters are selected to match the EM response at a specified operating point. Q3D directly provides the parasitic values, which can subsequently be used to build the equivalent circuit shown in Fig. (4.11).

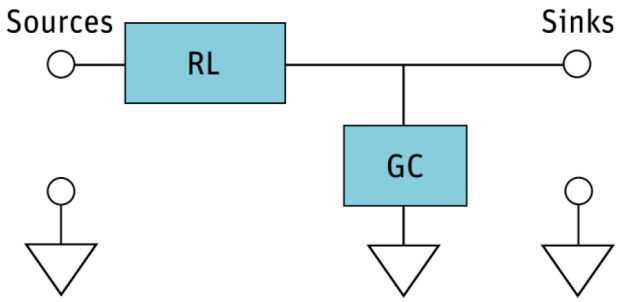


Fig. 4.11 Equivalent model of parasitic values extracted at a single frequency with Q3D. Picture from [73].

From a modeling standpoint, this approach offers several advantages. First, it yields a highly compact circuit representation consisting of a limited number of lumped elements, which can be easily implemented in SPICE-like simulators with negligible computational overhead. This simplicity makes single-frequency RLCG models particularly well suited for early design stages and preliminary performance assessment, where the rapid simulation turn-around is essential. Furthermore, as the extracted parameters are directly related to physical quantities, the resulting models

can provide valuable information on the dominant parasitic effects associated with the interconnect.

Despite these advantages, the limitations of single-frequency RLCG extraction must be carefully considered. By construction, the model captures the EM behavior only at the selected frequency, neglecting any frequency dependence of the parasitic parameters. As a consequence, phenomena such as skin effect and proximity effect cannot be accurately represented over a wide frequency range. When these phenomena become significant, the model may introduce substantial inaccuracies, particularly when employed in transient analyses.

Ladder circuit

The limitations of single-frequency RLCG extraction motivate the introduction of an intermediate modeling approach capable of capturing frequency-dependent effects while retaining a relatively compact circuit representation. This is achieved by modeling the interconnect using ladder networks composed exclusively of resistive and inductive elements, whose combined behavior reproduces the variation of parasitic resistance and inductance with frequency [109–118].

In this manner, the behavior associated with current redistribution phenomena, such as skin and proximity effects in conductors, are effectively captured. By appropriately cascading multiple RL sections, the transition from low-frequency to high-frequency conduction regimes can be approximated over a prescribed frequency range, yielding a more accurate description compared to a single-frequency lumped model.

This modeling approach is particularly effective in the analysis of SMPS, as the frequency dependence of parasitic inductance in the power loop—discussed in the previous chapter—directly affects current ripple, voltage overshoot, and switching-induced ringing. Accurately capturing the variation of inductance with frequency therefore enables more reliable prediction of these phenomena. Moreover, owing to the simplicity of the circuit topology and the limited model order, systematic variation of layout geometry and material properties can be performed efficiently, making this approach well suited for parametric studies in design exploration and

optimization. For these reasons, these models often provide an effective trade-off between physical fidelity and computational efficiency for system-level analysis of power electronic converters, prior to the adoption of more comprehensive broadband macromodeling techniques.

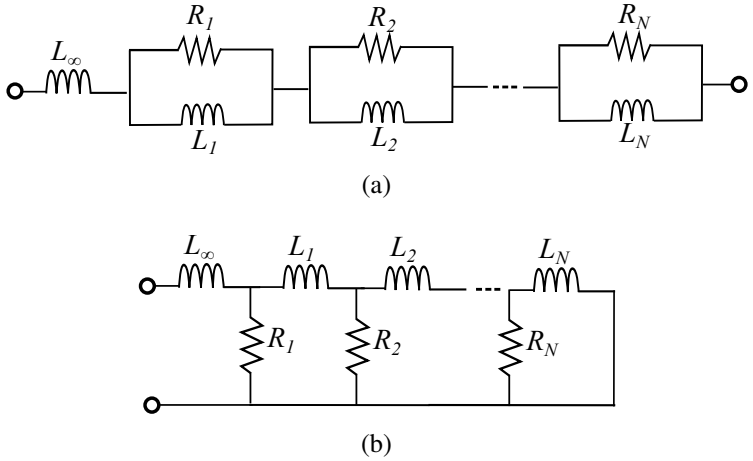


Fig. 4.12 Ladder circuit for network synthesis with Foster 1st form (a) and Cauer 1st form (b).

Classical network synthesis theory establish how a passive, LTI impedance can be implemented through networks of lumped elements [119]. Within this framework, Foster and Cauer syntheses, respectively shown in Fig 4.12(a) and (b), represent canonical constructions that map a realizable impedance function into equivalent circuits, thereby forming the theoretical foundation of ladder-based models for frequency-dependent parasitic behavior [120–130].

Let $Z(s)$ denote the driving-point impedance of a one-port network. Network synthesis theory establishes that any positive-real (PR) function can be realized by means of a passive network composed of lumped RLC elements. In the scalar case, positive-realness is defined by the following properties:

$$\begin{aligned} &Z(s) \text{ is analytic for } \Re\{s\} > 0, \\ &\Re\{Z(s)\} \geq 0 \quad \forall s \text{ with } \Re\{s\} > 0, \\ &Z(s^*) = Z^*(s). \end{aligned} \tag{4.17}$$

According to Foster model the impedances that can be represented have the following form:

$$Z(s) = A_\infty s + \sum_{i=1}^{N} \frac{A_i s}{s + \sigma_i} \tag{4.18}$$

where, as represented in Figure 4.12(a): $A_\infty = L_\infty$, $A_i = R_i$ and $\sigma_i = \frac{R_N}{L_N}$. Each term corresponds to an elementary branch, realized either as a parallel or series RL network (i.e. Foster I form, Foster II form) depending on the chosen dual form. From a theoretical viewpoint, this expansion decomposes the overall impedance into a sum of independent modes, each contributing over a limited frequency range.

For Cauer synthesis, instead, the implemented impedences in Fig 4.12(b) are the following,

$$Z(s) = A_\infty s + \cfrac{1}{\frac{1}{R_1} + \cfrac{1}{sL_1 + \cfrac{1}{\frac{1}{R_2} + \cfrac{1}{sL_2 + \cdots + \cfrac{1}{\frac{1}{R_N} + \frac{1}{sL_N}}}}}}} \tag{4.19}$$

with $A_\infty = L_\infty$, where the resulting ladder topology consist of alternating resistive and inductive elements.

Foster and Cauer syntheses realize the same class of PR functions, providing systematic procedures for representing passive, LTI one-port impedances through networks of lumped, frequency-independent elements. In this process, they establish the theoretical legitimacy of ladder-based circuit representations as mappings of frequency-dependent impedance behavior onto passive network topologies.

When the impedance arises from frequency-dependent current redistribution mechanisms in conductors, such as those associated with skin effect, the resulting ladder topologies can be viewed as a discrete approximation of an underlying diffusion process governing current penetration within the conductor cross-section. Since diffusion phenomena are characterized by a continuum of penetration depths and associated relaxation times, an exact circuit representation would, in principle, require an infinite number of degrees of freedom. In practice, however, the dominant behavior over a finite frequency range can be captured by truncating the ladder to a limited number of sections. As a consequence, direct application of these syntheses may lead to high-order circuit realizations to obtain an accurate result. In fact, the synthesis process involves identifying poles and zeros, or an equivalent

continued-fraction expansion, and selecting a finite network order that yields an acceptable approximation.

Since in conductor affected by skin effect, the frequency dependence of resistance and inductance follows a well-defined physical law governed by current diffusion within the conductor cross-section, the general Foster or Cauer can therefore be optimized [131–134], giving rise to models that work better for this context [135, 136].

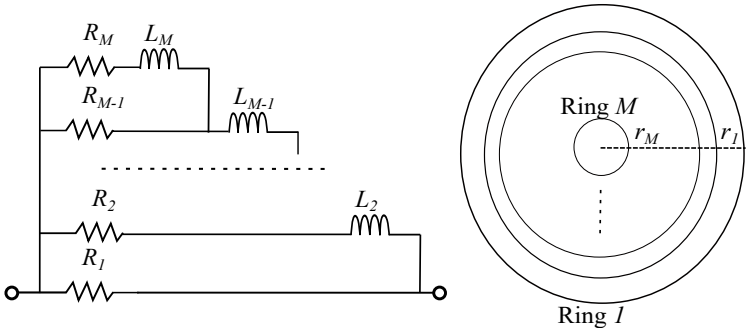


Fig. 4.13 Equivalent circuit for skin-effect loss and corresponding conductor ring definition.

One of the physically motivated formulations in this regard is the time-domain skin-effect model proposed in [137]. In this approach, skin effect is derived directly from the diffusion equation governing current penetration and is represented through an equivalent circuit obtained by discretizing the conductor cross-section (Fig. 4.13).

The conductor is subdivided into a set of concentric regions, each associated with a partial resistance and a partial inductance per unit length. These parameters depend explicitly on the geometry and material properties of the conductor. For a circular conductor of conductivity σ, partial resistance per unit length of the i-th region can be expressed as

$$R_i = \frac{1}{A_i \sigma}, \tag{4.20}$$

where A_i denotes the cross-sectional area of the corresponding annular layer. The corresponding partial inductance per unit length is given by

$$L_i = \frac{\mu (r_{i-1} - r_i)}{2\pi r_i}, \tag{4.21}$$

where μ is the magnetic permeability, and r_{i-1} and r_i define the radial boundaries of the layer. These expressions explicitly link the circuit parameters to the physical geometry of the conductor, providing a clear interpretation of each ladder section in terms of current diffusion depth.

While this formulation is physically rigorous and offers valuable insight into the nature of skin effect, its applicability is inherently limited. The derivation relies on strong assumptions regarding conductor geometry. As a result, the model cannot be straightforwardly extended to arbitrary cross-sections, complex layouts, or interconnect structures where current distribution is influenced by geometry, proximity effects, or nonuniform return paths.

Moreover, the parameter extraction process is analytical rather than data-driven, and therefore cannot directly leverage frequency-dependent resistance and inductance values obtained from EM solvers. These limitations motivate the development of equivalent skin-effect models that retain the physical insight of diffusion-based approaches while being applicable to general interconnect geometries and directly compatible with EM-extracted data.

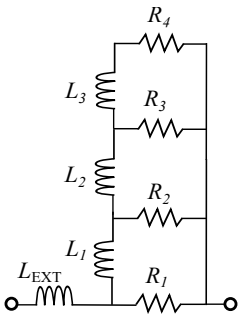


Fig. 4.14 Neikirk Ladder model.

This limitation is partially overcome by the Neikirk model [138] in Fig. 4.14, which introduces a physically optimized ladder representation of skin effect that can be derived from EM simulations. In particular, the Neikirk model can be adapted by using the DC resistance R_{dc} and inductance L_{dc}, together with the high-frequency resistance R_{ac} and inductance L_{ac} evaluated at a representative angular frequency ω. Starting from these extrema, an iterative fitting procedure is applied, to determine the intermediate resistive and inductive values of a predefined RL ladder topology.

The fitting procedure exploits the known behavior of skin effect, namely the fact that resistance grows approximately proportional to the square root of frequency, while the internal inductance decreases and approaches a constant external value. By enforcing these trends, the ladder parameters are adjusted so that the equivalent circuit reproduces both the transition of $R(f)$ and $L(f)$ between the low-frequency and high-frequency limits.

This approach is particularly effective for transmission lines and uniform conductors, but its generality is inherently limited, as the intermediate frequency response is not directly extracted but reconstructed by assuming an idealized skin-effect behavior based solely on the extreme values.

These limitations motivate the development of a more general equivalent skin-effect modeling approach, in which the ladder parameters are derived directly from EM-extracted data over multiple frequency decades, without assuming a specific analytical dependence of the impedance on frequency.

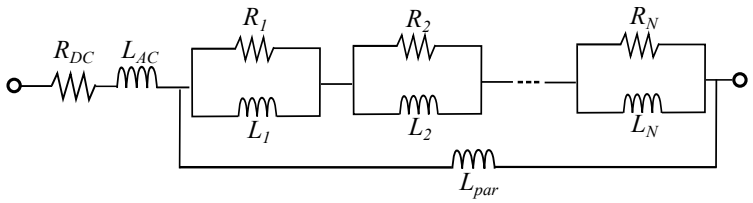


Fig. 4.15 Representation of the proposed equivalent circuit to reproduce the skin-effect behavior.

Therefore, the proposed equivalent circuit, depicted in Figure 4.15, is formulated as a modified Foster-type ladder.

Unlike classical synthesis approaches, the construction of this model does not require *a priori* knowledge of the location of singularities in the complex frequency plane. Instead, resistance and inductance values obtained from the quasi-static EM solver, are directly used to determine the circuit parameters. In this way, the model accurately reproduces the increasing of resistance with each cell element $R_i - L_i$, and at the same time to recover the value of the inductance with L_{par}. Considering the frequency space between the ending of DC region and the maximum frequency desired for the analysis, a new cell element is added for each decade of frequency.

Therefore if N is the number of decades of interest after $f_{DC,limit}$ a number of cell equal to N must be inserted in the final equivalent circuit.

The impedances that can be represented now are:

$$Z(s) = A_0 + \frac{A_p s \sum_{i=1}^{N} \left[A_i \prod_{\substack{j=1 \\ j\neq i}}^{N} (s+\sigma_j) \right]}{A_p \prod_{i=1}^{N} (s+\sigma_i) + \sum_{i=1}^{N} \left[A_i \prod_{\substack{j=1 \\ j\neq i}}^{N} (s+\sigma_j) \right]} + A_\infty s \tag{4.22}$$

where $A_0 = R_{DC}$, $A_\infty = L_{AC}$, $A_p = L_{par}$, $A_i = R_i$ and $\sigma_{i,j} = \frac{R_{i,j}}{L_{i,j}}$ as can be seen in Figure 4.15.

In order to get the desired value for inductance and resistance in the DC region the limits of the impedance for frequency that tends to 0 are computed and they are imposed to be equal to the simulator values extracted in that region:

$$\lim_{f\to 0} \mathrm{Re}[Z(s)] = R_{DC} = R_{DC,sim} \tag{4.23}$$

$$\lim_{f\to 0} \mathrm{Im}\left[\frac{Z(s)}{2\pi f}\right] = L_{AC} + \frac{L_{par} \sum_{i=1}^{N} L_i}{L_{par} + \sum_{i=1}^{N} L_i} = L_{DC,sim} \tag{4.24}$$

where Re and Im are the real part and the imaginary part operator, respectively.

The same procedure is applied to higher frequency to obtain the desired inductance value at the maximum frequency needed:

$$\lim_{f\to \infty} \mathrm{Im}\left[\frac{Z(s)}{2\pi f}\right] = L_{AC} = L_{AC_{max},sim} \tag{4.25}$$

Conversely, to reproduce the progress of the resistance with the increasing of frequency, the real part of the impedance is approximated with its limit at frequency that tends to infinity. Subsequently for each decade of frequency after the ending of DC region, the computed limit is equated to the corresponding parameter extracted from the simulator, therefore the resistance of every $R_i - L_i$ cell is assigned, until reaching

the cell $R_N - L_N$ that corresponds to the behavior of the last decade of frequency of interest:

$$\lim_{f\to\infty} \mathrm{Re}[Z(s)] = R_{DC} + \sum_{i=1}^{N} R_i = R_{AC_i,sim} \tag{4.26}$$

In this way the desired resistance values have been set and to obtain them in correspondence of the right frequency points so that the frequency evolution of the real part of the impedance is correctly reproduced, the inductance values are chosen as follows:

$$L_N = \frac{k_N R_N}{2\pi f_N} \tag{4.27}$$

where k_N, is a degree of freedom, whose suggested value, for $N \neq 1$, is $k_N = 3$ since it was possible to notice experimentally that the position of the zeroes and poles falls in the correct place to ensure that the increase in the resistance curve is proportional to the square root of the frequency. Otherwise for the first cell the value of inductance has to be chosen not to have negative values. By setting $k_1 \geq 3$ we satisfy the following condition that guarantees having only real components:

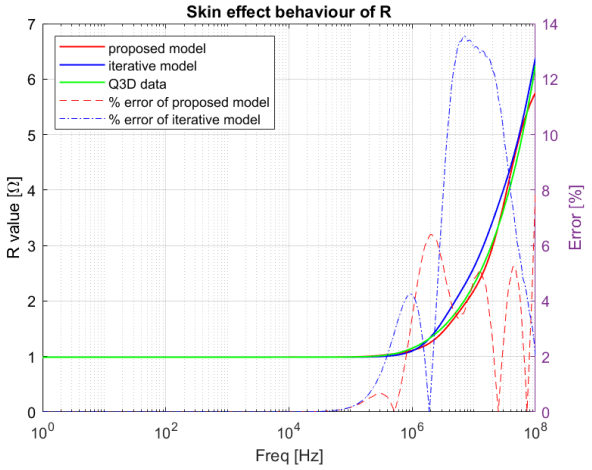
$$L_1 + \sum_{i=2}^{N} L_i > L_{DC} - L_{AC} \tag{4.28}$$

Consequently constraints on each element of the circuit were defined, and by solving the mathematical impositions it is possible to directly obtain the values of the resistances and inductances that constitute the equivalent skin-effect circuit model.

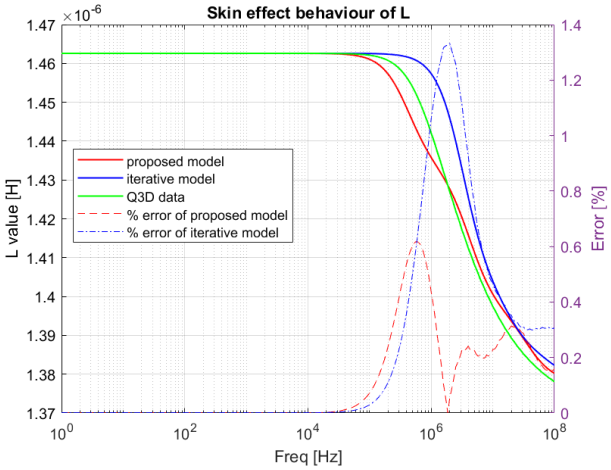
The proposed method is now implemented into practical examples. Two different structures are analyzed to observe the generic validity of the model.

First, the PCB coil used also in [139] is considered. The files that described its geometry and the assignment of material properties are loaded into the software. The electromagnetic simulation runs up to 100 MHz because since that value the predominant non-ideality is the skin effect while after that frequency the resonance takes over. The upper limit of the DC region is approximately equal to 100 kHz, instead the lower bound of AC region is about 1 MHz as can be seen from the curves obtained from the electromagnetic simulation in Figure 4.16. Therefore, the required number of cells to reproduce this behavior is $\log(100\,\mathrm{MHz}/100\,\mathrm{kHz}) = 3$.

Subsequently after having performed the EM analysis the values of resistance and inductance in DC region and in each decade of frequency after the ending of DC region are extracted from the simulator. The conditions explained above are imposed and the equivalent circuit that is obtained has the following parameters: $R_{DC} = 0.9884\,\Omega$, $R_1 = 0.16\,\Omega$, $R_2 = 1.15\,\Omega$, $R_3 = 3.95\,\Omega$, $L_{AC} = 1.378\,\mu H$, $L_1 = 77\,nH$, $L_2 = 55\,nH$, $L_3 = 19\,nH$, $L_{par} = 0.19\,\mu H$.
The resulting resistance and inductance obtained from the computed equivalent circuit is then evaluated and compared to the target data obtained from the electromagnetic simulation. A comparison with the existing method of Kim and Neikirk following the iterative procedure is also performed.



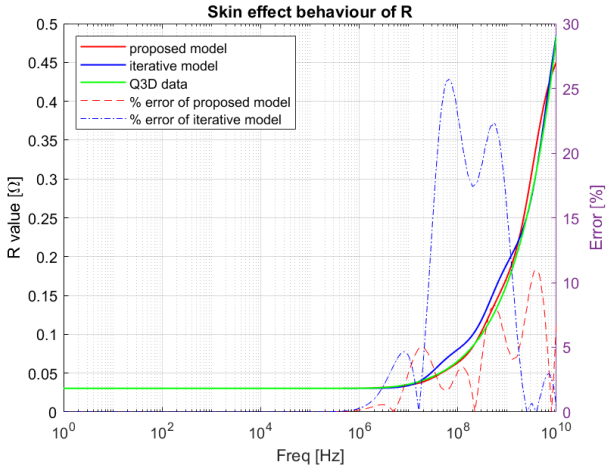
(a)



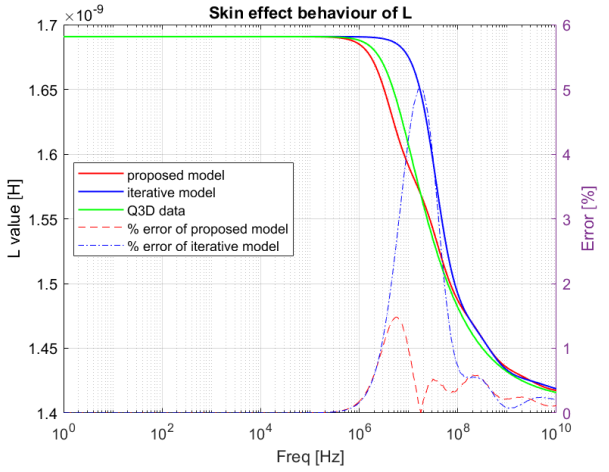
(b)

Fig. 4.16 Comparison of resistance and inductance behavior of a PCB coil between proposed circuit, Kim and Neikirk iterative method and wanted value obtained from electromagnetic simulation.

The second considered case is a copper bonding wire with a diameter of 1.2 mil of a QFN package, to which the same procedure has been applied.



(a)



(b)

Fig. 4.17 Comparison of resistance and inductance behavior of a copper wire of a package between proposed circuit, Kim and Neikirk iterative method and wanted value obtained from electromagnetic simulation.

In this case since the rising times of the signals that are involved are of the order of *ns* we are interested in parasitic resistance and inductance in a wide band of frequencies, therefore the simulation is performed up to 10 GHz. The limit of DC region is about 1 MHz while the lower bound of AC region is approximately equal to 10 MHz. Since now the decades of interest after the initial constant region are 4, the equivalent circuit has 4 cell elements with the following values: $R_{DC} = 0.03\,\Omega$, $R_1 = 5.2\,\text{m}\Omega$, $R_2 = 30\,\text{m}\Omega$, $R_3 = 0.1\,\Omega$, $R_4 = 0.32\,\Omega$, $L_{AC} = 1.416\,\text{nH}$, $L_1 =$

0.25 nH, $L_2 = 0.14$ nH, $L_3 = 48$ pH, $L_4 = 15$ pH, $L_{par} = 0.69$ nH. Also in this case the parasitic resistance and inductance of the proposed circuit are compared in Figure 4.17 with that obtained with the iterative method and the desired values of the simulator.

As a result of the comparison, it can be noted that in both the examples over the entire range of frequencies the obtained curves almost approximate the target behavior of the electromagnetic simulation. By computing the relative error of the models with respect to the simulator values it is possible to see that the error of the proposed method is comparable with the one of the iterative procedure. Thus a circuit with equal simulation complexity constitute only of R and L elements is obtained but with a reduced computational time and less calculation effort, maintaining accuracy and showing a lower maximum error on the range of frequency of interest.

Broadband model

In applications where interconnect behavior must be accurately represented over a wide frequency range, compact frequency-dependent RL ladder models often prove insufficient. While such reduced models are suitable for low-frequency or quasi-static analysis, they are unable to capture the full EM response when strong coupling effects, frequency-dependent losses, and distributed phenomena become significant. In these scenarios, a broadband modeling approach is required in order to faithfully describe the complete frequency-domain behavior of an arbitrary N-port interconnect structure as obtained from full-wave or quasi-static EM simulations.

Broadband macromodels aim to approximate the entire frequency response of the interconnect, typically expressed in terms of scattering parameters, by means of a rational representation that can be efficiently employed in time-domain circuit simulations. This requires transforming frequency-domain EM data into an equivalent time-domain model, suitable for transient and mixed-signal analysis. As a result, simulation environments capable of converting S-parameters into a time-domain representation, generating a SPICE-compatible netlist, must be employed.

In this work, several commercial tools were evaluated and used to generate broadband macromodels from EM simulation results, including the Broadband

Macromodel Generator in ANSYS, the Broadband SPICE Model Generator in Keysight ADS, the N-Port component in Cadence Spectre, the `rationalfit` function in MATLAB, and the IdEM framework, currently integrated within the CST environment, summarized in Fig.4.18. Although all these tools aim at achieving the same fundamental goal, namely, enabling accurate time-domain simulation of broadband interconnects, they differ significantly in terms of modeling methodology, degree of user control, transparency, robustness, and passivity handling.



Fig. 4.18 Different tools used for the data translation from frequency to time domain.

- **Broadband Model Generator** of commercial tools such as ANSYS and Keysight ADS provide automated broadband macromodel generators that extract SPICE-compatible equivalent circuits directly from EM simulation results. Internally, these tools fit the tabulated S-parameters using rational functions and synthesize equivalent networks suitable for transient analysis.

  The overall workflow is designed to be largely automatic, hiding the numerical complexity associated with rational approximation, pole extraction, and passivity enforcement. Typically, the user specifies global fitting targets, such as maximum error tolerances, or bounds on the model order. Based on these constraints, the solver automatically determines the pole structure and performs iterative fitting. While this approach is convenient for standard use cases, it offers limited transparency. In particular, the user has no direct access to the extracted pole locations, cannot monitor the evolution of the fitting error across iterations, and cannot selectively intervene on problematic fitting. As a consequence, the quality of the final macromodel, defined in terms of accuracy, stability, passivity, and model order, can only be assessed a posteri-

ori, after exporting the fitted S-parameters or the synthesized SPICE netlist and performing an external validation. Achieving an acceptable trade-off between fitting accuracy and model complexity often requires multiple extraction cycles, with parameter adjustments performed largely by trial and error. Passivity enforcement in both ANSYS and ADS is also handled as a closed, internal process. The user is not informed about which specific frequencies, matrix entries, or residues violate passivity, nor about the magnitude of the perturbations introduced to restore it. This lack of visibility makes it difficult to assess whether the passivation step has significantly degraded accuracy, especially in dense multi-port structures where small local violations may lead to substantial global corrections. A representative example of this approach is the broadband equivalent circuit generated by quasi-static EM solvers such as Q3D, shown in Fig. 4.19.

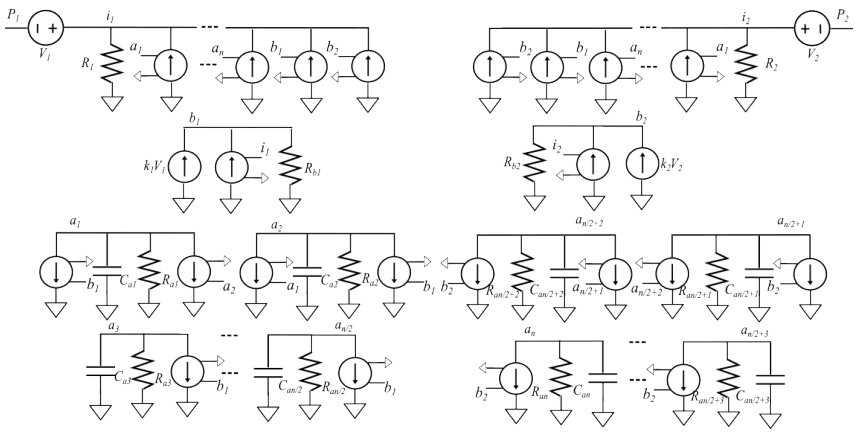


Fig. 4.19 Broadband circuit generated from Q3D simulator to reproduce the variation of parasitic element in frequency of a generic N-port system.

Unlike reduced RL ladder models, the resulting circuit is no longer composed exclusively of passive lumped elements, but also includes controlled sources. These controlled generators are required to reproduce the full multi-port frequency response extracted from the EM solver, including coupling effects and frequency-dependent behavior. Although this increased structural complexity enables a much more general and accurate representation of the interconnect response, passivity is no longer guaranteed by construction. In particular, the inclusion of controlled sources may lead to non-physical energy generation if

the model is not explicitly constrained. When these broadband macromodels are embedded in SPICE-like transient simulations, especially in the presence of nonlinear elements such as switching devices or control circuitry, this can result in numerical instability and convergence issues.

To mitigate these issues, as previously discussed, passivity enforcement is often applied as a necessary condition to guarantee stable time-domain behavior. However, the applied correction procedures frequently results in a degradation of modeling accuracy.

- **The N-Port** component available in Cadence Virtuoso, using the Spectre simulator, offers several internal options for converting frequency-domain S-parameter data into a representation suitable for transient simulation. One option relies on Digital Signal Processing (DSP) techniques, in which the time-domain impulse response is reconstructed directly from the tabulated frequency response using interpolation, windowing, smoothing, and inverse fast Fourier transform (IFFT) procedures. In this mode, no rational macromodel is generated, and no poles or residues are computed. An alternative option is the Complex Pole Fitting (CPF) mode, which constitutes the only Spectre-based approach that performs a rational approximation of the S-parameters. When CPF is enabled, Spectre executes a vector-fitting-like procedure to extract complex poles and residues. However, the implementation exposes very limited configurability. The user cannot specify the number of poles, adjust initial pole locations, or iteratively refine the fit. As a result, the user has no direct control over the pole structure, model order, or fitting accuracy, nor over the procedures used for passivity enforcement. When passivity correction is applied, no information is provided regarding the location or severity of the violations, the affected frequency ranges, or the magnitude of the perturbations introduced into the rational coefficients. Consequently, it is not possible to evaluate whether the correction has compromised model fidelity. Overall, the Spectre N-Port component represents a black-box solution with minimal tunability. While it is effective for circuits with a very small number of ports and smooth S-parameters datasets, it is generally unsuitable for high-order multi-port interconnects or applications requiring tight control over accuracy, complexity, and numerical robustness.

- **MATLAB Vector Fitting (VF)** [140, 141] provides full theoretical control over the rational approximation process. The user can freely select the number of poles, define their initial locations, choose the relocation strategy, and inspect the extracted pole–residue structure in detail. Moreover, fitting errors can be explicitly computed, visualized, and analyzed, enabling the development of customized fitting workflows. Despite this high level of transparency and flexibility, MATLAB VF has several limitations. Handling large multi-port datasets requires substantial custom scripting, as the tool does not natively manage complex port-dependent fitting strategies. Furthermore, the resulting rational model is not guaranteed to be passive. MATLAB provides separate functions to detect passivity violations and to attempt their correction by perturbing residues and constant terms. However, these procedures are not as robust or sophisticated as those implemented in dedicated macromodeling tools. In addition, the generation of SPICE-compatible macromodels is not fully integrated into the fitting workflow and requires the use of separate export functions. Therefore, although MATLAB VF offers unmatched theoretical freedom and insight into the fitting process, it lacks the automation, robustness, and industrial-grade integration required for large-scale broadband macromodeling.

- **IdEM** represents a high-performance and rigorously controlled environment for broadband macromodel extraction from S-parameter data. It combines advanced Vector Fitting techniques with model-order reduction and robust passivity enforcement algorithms to generate rational, causal, and passive macromodels. A key strength of IdEM lies in its complete transparency throughout the modeling process. The user can inspect poles, residues, fitting errors, and passivity violations at every stage, with real-time visualization of the error both as a function of frequency and across the full S-parameter matrix. Unlike ANSYS and ADS, where the relationship between fitting parameters and model quality can only be assessed after export, IdEM continuously exposes these metrics during fitting, enabling precise control over the accuracy–complexity trade-off. Passivity enforcement in IdEM is also significantly more advanced. The tool identifies the exact frequencies and matrix elements where passivity is violated, quantifies the severity of each

violation, and applies optimized correction strategies. Crucially, the accuracy of the model can be immediately re-evaluated after passivation, allowing the user to verify that numerical stability has been restored without introducing unacceptable distortions. IdEM optimization algorithms typically produce models with fewer poles compared to those generated by fully automatic fitting engines, thereby reducing simulation complexity while maintaining accuracy.

To ensure robust time-domain simulation, passivity enforcement techniques must be applied to broadband macromodels. These techniques impose global energy constraints on the fitted rational model, thereby guaranteeing stability and convergence when the macromodel is embedded in transient simulations involving nonlinear circuit elements. However, passivity enforcement is not without consequences. In many cases, the correction process perturbs the original model coefficients, introducing localized distortions in the frequency response. Such distortions may degrade modeling accuracy, particularly in frequency regions of primary interest. Consequently, a fundamental trade-off emerges between numerical robustness and fidelity to the original EM data. This trade-off represents a fundamental challenge in broadband macromodeling and must be carefully managed. A detailed discussion of this aspect is deferred to Section 4.3.3.

Therefore, depending on the specific analysis objective, interconnect models can provide different accuracy and computational cost. Single-frequency RLCG models and frequency-dependent RL ladder representations constitute efficient alternatives when the dominant phenomena are well understood and confined to limited frequency ranges. The selection of the interconnect representation must be guided by the specific analysis to be performed. In practical design workflows, this often leads to a hierarchical modeling strategy in which different interconnect models are employed at different stages of analysis or for different subsystems within the same system-level simulation.

4.2 Full-wave analysis

As established in the preceding discussion, the switching operation of power electronic converters produces rapid variations in voltage and current waveforms, which

inherently result in conducted electromagnetic emissions characterized by a broad spectral content. While the fundamental component of the emission spectrum is directly related to the switching frequency, the non-ideal shape and periodic nature of the switching waveforms generate higher-order harmonics that extend over several decades in frequency.

From an EM modeling perspective, this broadband behavior cannot be fully captured using purely quasi-static approaches. Although quasi-static solvers are well suited for low-frequency parasitic extraction, the increasing importance of high frequencies effects motivates the adoption of full-wave EM analysis. In this context, full-wave solvers are required to accurately account for propagation delay, phase variation, coupling, and radiation phenomena that influence the behavior of printed circuit boards and packages.

In the following section, the full-wave simulation framework is introduced and particular emphasis is placed on the configuration of EM models in the time domain and on the implications of this choice for accurately capturing switching node waveform.

4.2.1 Port Definition and Simulation Settings

To provide a comprehensive description of frequency-domain electromagnetic modeling, the procedure implemented in HFSS [142], is outlined in the following, consistently with the approach adopted for the quasi-static case.

- **Geometry and Material Definition**: the HFSS workflow starts with the construction of a three-dimensional model representing the device or structure under test. The geometry can be created directly within the HFSS environment or imported from external CAD tools. Once the geometry is defined, material properties are assigned to each object.
- **Simulation Space and Boundary Conditions**: unlike Q3D, which inherently addresses open-region quasi-static problems, HFSS requires the specification of a simulation boundary that encloses the entire structure. This boundary defines the computational domain in which the finite element solution is

performed, and all objects within this volume are included in the mesh. Closed boundaries model structures in which electromagnetic energy cannot leave the domain except through defined ports, whereas open boundaries allow waves to radiate outward. For radiating structures, radiation boundaries are typically placed at a distance of at least $\lambda/4$ from strongly radiating elements, where λ denotes the operating wavelength corresponding to the frequency of interest, and $\lambda/10$ from weakly radiating ones. HFSS also allows the user to specify an operating frequency when creating an open region through the *Create Open Region* dialog. In this case, the software automatically sizes the boundary volume based on the wavelength corresponding to the specified frequency, ensuring an appropriate balance between accuracy and computational cost. As the geometry size increases, the simulation boundary scales accordingly, maintaining consistent electromagnetic behavior.

- **Port Definition and Excitations**: After defining the simulation space and boundaries, ports and excitations are assigned. Ports simultaneously act as excitation sources and as interfaces for the extraction of network parameters. Two primary port types are available: lumped ports and wave ports. Both can be used to compute S-, Y-, and Z-parameters, as well as local field quantities.

  – *Lumped ports* are typically employed for single-mode excitation in non-uniform or electrically small structures, such as connectors, BGA transitions, and PCB trace terminations.

  – *Wave ports* on the other hand, are used for closed guiding structures that may support multiple propagating modes, including waveguides and coaxial lines.

The selected port type affects the normalization and interpretation of the extracted S-parameters. Lumped ports allow normalization to a user-defined characteristic impedance, making them particularly suitable for low-impedance interconnect and PCB analyses. Wave ports compute the characteristic impedance directly from the field solution and allow the excitation and extraction of multiple modes, which is essential for high-frequency or multi-mode structures. HFSS provides two solution formulations: Driven Modal and Driven Terminal. Both are compatible with lumped ports, for which the resulting S-parameters

are equivalent. The choice of formulation determines how excitations and responses are interpreted.

  - In *Driven Modal solution*, ports are treated from a field-based transmission line perspective. Excitations are defined in terms of incident power, and the port fields are decomposed into orthogonal modes, such as transverse electric (TE), transverse magnetic (TM), or transverse electromagnetic (TEM). Each propagating mode corresponds to a distinct entry in the S-, Y-, and Z-parameter matrices. This formulation is particularly well suited for structures where multiple modes propagate, including waveguides and radiating devices.
  - In contrast, the *Driven Terminal solution* adopts a circuit-oriented perspective, where the port excitation is expressed in terms of total voltage, defined as the superposition of incident and reflected components. Each conductor associated with a port is treated as an individual terminal, and propagation is assumed to occur in a single TEM mode. This approach is particularly advantageous for low-impedance and circuit-like structures, such as PCB interconnects, connectors, and differential pairs, and it naturally supports differential S-parameter extraction.

  Therefore, all simulations presented in this work were performed using lumped ports in the Driven Terminal formulation, consistently with the characteristics of the PCB and package structures considered.

- **Analysis Setup and Frequency Sweep**: once ports are assigned, HFSS allows configuration of the analysis parameters that govern convergence and numerical accuracy. This includes the definition of a solution frequency, the frequency range for subsequent sweeps, and the error tolerance. The solution frequency is the frequency at which adaptive meshing and convergence are performed. At this frequency, HFSS generates an initial finite element mesh and iteratively refines it until the solution meets the specified accuracy criteria, typically quantified by the parameter ΔS, which represents the maximum allowable relative change in S-parameters between consecutive adaptive passes. For optimal accuracy, the solution frequency is usually selected near the frequency of primary interest or close to expected resonances. After convergence

at the solution frequency, HFSS performs a frequency sweep over the user-defined range. The sweep points are used to evaluate the frequency-dependent behavior of S-parameters, fields, and related quantities. In most cases, the mesh generated at the solution frequency is reused for the sweep, although additional refinement may occur for broadband or multi-frequency adaptive analyses. Other relevant parameters in this stage include the maximum number of adaptive passes and the specification of sweep points, which together ensure convergence to a stable and accurate solution while avoiding unnecessary computational effort.

- **Post-Processing and Equivalent Parameter Extraction**: once convergence is achieved, HFSS enables detailed visualization of S-parameters and electromagnetic field distributions. For circuit-level analysis, the extracted S-parameters can be transformed into Y-parameters, as discussed in more detail in the following section.

The described workflow highlights the suitability of HFSS for frequency-domain EM analysis, supporting the extraction of accurate S-parameters and field information necessary for modeling and subsequent circuit-level evaluation.

4.2.2 Derivation of parasitic inductance and resistance

Using HFSS, it is possible to accurately simulate the actual current paths within the structure under analysis and to extract the associated parasitic parameters of the resulting conductive loops. Similarly to Q3D, the extracted parasitic elements can subsequently be incorporated into electrical co-simulation environments together with discrete components, enabling comprehensive signal-integrity, power-integrity, and EMI analyses. In HFSS, system excitation is typically defined through differential ports in order to correctly represent the physical behavior of multi-conductor interconnects. However, when an equivalent representation with respect to the Q3D port definition is desired, an alternative modeling strategy can be adopted by using single-ended ports referenced to a common point on the PCB ground. While this approach facilitates a more direct comparison between full-wave and quasi-static results, it introduces several limitations, which are discussed in the following.

- The use of multiple single-ended ports increases the total number of ports and, consequently, the order of the time-domain macromodel, resulting in higher computational complexity [143].
- Assigning the same reference to all ports is often impractical in EM simulator environments. For instance, in multilayer PCBs, directly referencing all ports to the same ground node may not be physically feasible [144].
- Even with a ground reference on the same layer, connecting all terminals to this point inevitably involves electrically long port extensions, which alter the extracted parasitics. Additional techniques, such as de-embedding, are necessary to remove the port contribution [145].

For these reasons, employing differential ports in the full-wave simulation becomes necessary. In this configuration, the resulting parasitic effects captured in the simulation correspond to those associated with the simulated current loop. To extract the parasitic resistance and inductance from HFSS results, the relationship between the S-parameters and the admittance matrix (Y-parameters) can be used.

For each port, the S-parameters are computed while terminating all other ports with the system reference impedance Z_0. Instead, to obtain the Y-parameters matrix, the other ports are considered in short-circuit conditions. This means that for each port, the corresponding Y-parameter inherently accounts for the parasitic effects of the entire loop, with the remaining ports effectively forming a closed circuit. In other words, the self-admittance $Y_{i,i}$ of a given port represents the combined influence of all parasitic elements along the current path that passes through the ports closed in a short circuit, capturing the full electromagnetic behavior of the loop in which the ports are embedded.

Once the Y-matrix is obtained, the self-admittance of a given port can be used to calculate the parasitic resistance and inductance as:

$$L_i = \Im\left(\frac{1}{Y_{i,i}\,2\pi f}\right), \qquad R_i = \Re\left(\frac{1}{Y_{i,i}}\right). \tag{4.29}$$

4.2.3 Co-simulation in time domain

Building on the requirement to adopt differential port definitions discussed in the previous section, an important implication arises in the subsequent transient analysis. In this configuration, all voltages are inherently evaluated as relative quantities between port terminals, rather than as absolute voltages referenced to the system ground. As a consequence, the direct observation of the SW-node voltage with respect to the ground reference is not possible. This limitation is particularly critical in gate-driver design and in the assessment of radiated EMI, where absolute voltage levels and common-mode behavior play a fundamental role [15], [9].

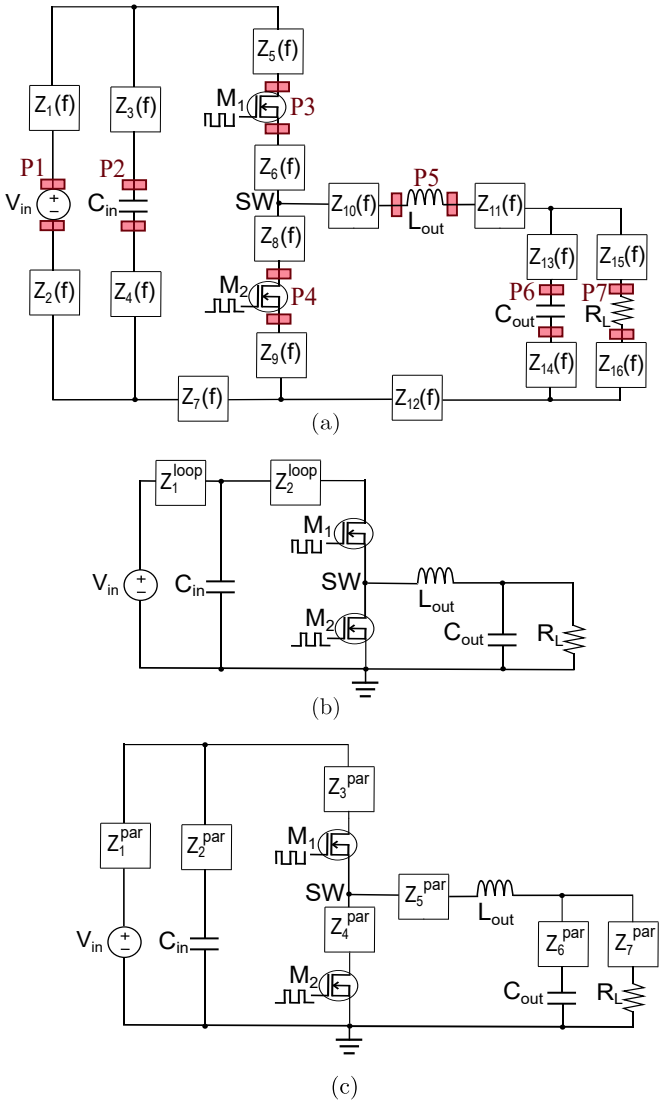


Fig. 4.20 (a) Circuit schematic of the DC–DC Buck converter with parasitic impedance, and terminals representing the differential ports of EM simulation. (b) Usually adopted method for first-order estimation of SW voltage. (c) Presented model of parasitic components.

A comprehensive model accounting for the parasitics between each component of the Buck converter is presented in Fig. 4.20(a), where $Z_n(f) = R_n(f) + j2\pi f L_n(f)$ represents the frequency-dependent parasitic element impedances. During the EM analysis, differential ports are placed across each component pad, as highlighted in red in Fig. 4.20(a). In the subsequent time-domain co-simulation, the components are added, and the resulting voltages represent relative quantities, preventing direct access to node voltages with respect to the ground reference.

A widely adopted approach to overcome this limitation, for a first-order estimation, consists of considering the parasitic components of the switching loop, as depicted in Fig. 4.20(b), in particular its loop inductance since it is critical for high-frequency switching behavior. However, this method provides an initial estimation, since as noted in [146, 147], the parasitics of the different interconnections directly influence the resulting waveforms.

To illustrate the impact of the different modeling circuits on the SW node voltage, a Buck converter operating at a SW frequency of 500 kHz, with $C_{\text{in}} = 4.7\,\mu\text{F}$, $C_{\text{out}} = 22\,\mu\text{F}$ and $L_{\text{out}} = 1\,\mu\text{H}$ is considered. At this stage, topology (a) is treated as if the parasitic values were not derived from the EM simulator, which would otherwise generate a single model providing only relative voltages. Instead, the parasitics are assumed to be known and represented by a series inductor of 2 nH and a series resistor of 0.5 mΩ. This approach allows constructing the actual circuit including the parasitics, which can then be directly compared with the models designed to replicate this behavior. From the waveforms obtained with SIMPLIS, shown in Fig. 4.21, it can be observed that the configuration (b), with respect to circuit (a), provides only an approximation, leading to an overestimation of the peak during the rising edge and an inaccurate reproduction of the negative peak during the falling transition.

Therefore, the model shown in Fig. 4.20(c) is proposed, where the parasitic elements are grouped as follows:

$$\begin{aligned}
Z_1^{\text{par}} &= Z_1(f) + Z_2(f), & Z_2^{\text{par}} &= Z_3(f) + Z_4(f),\\
Z_3^{\text{par}} &= Z_5(f) + Z_6(f) + Z_7(f), & Z_4^{\text{par}} &= Z_8(f) + Z_9(f),\\
Z_5^{\text{par}} &= Z_{10}(f) + Z_{11}(f) + Z_{12}(f), & Z_6^{\text{par}} &= Z_{13}(f) + Z_{14}(f),\\
Z_7^{\text{par}} &= Z_{15}(f) + Z_{16}(f).
\end{aligned} \tag{4.30}$$

Analytically deriving the Y-parameters at the ports defined in Fig. 4.20(a) for topology (a) and (c), where each element of the admittance matrix is defined as:

$$Y_{i,j} = \left.\frac{I_i}{V_j}\right|_{V_k=0, k\neq j}, \tag{4.31}$$

it can be observed that the resulting matrices are identical:

$$\mathbf{Y}^{(a)} = \mathbf{Y}^{(c)}. \tag{4.32}$$

Indeed, as shown by the SW node voltage in Fig. 4.21, the waveforms of topology (a) and (c) exhibit good correspondence.

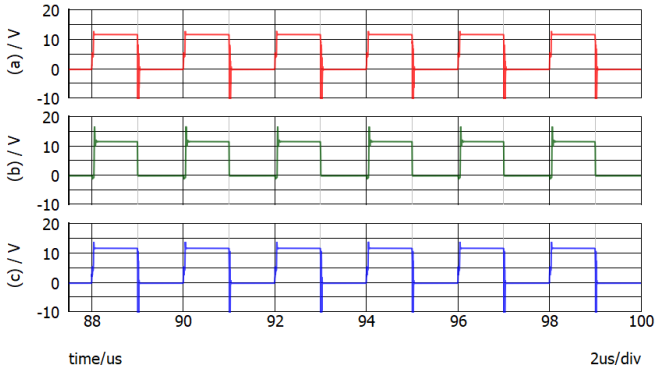


Fig. 4.21 Comparison between SW voltage of complete model of parasitic element (a), first approximation model (b) and proposed model (c).

Considering now the parameters obtained from the EM analysis (e.g., S-, Z-, or Y-matrices), and knowing the circuit topology of parasitic elements in Fig. 4.20(c), the values of all parasitic impedances can be uniquely determined [148]. The analytical Y-matrix of circuit in Fig. 4.20(c), $\mathbf{Y}^{(c)}$ is therefore equated to the numerical values of Y-matrix obtained from the EM simulation, $\mathbf{Y}^{\text{sim}}$:

$$\mathbf{Y}^{(c)}(\{Z_n^{\text{par}}\}) = \mathbf{Y}^{\text{sim}}, \tag{4.33}$$

where Z_n^{par} represent the unknowns, and can be derived by inverting the system in MATLAB environment.

The derived frequency-dependent impedances can subsequently be converted into the time domain to generate a macromodel, either directly in HFSS, using a broadband generator in ADS, or with dedicated tools such as IdEM. This enables the co-simulation of the extracted parasitic network with the Buck converter components, allowing the evaluation of absolute node voltages.

To validate the simulation results and confirm the correct extraction of the parasitic elements, a two-layer PCB, described in P4, was specifically designed to

enhance the contributions of the interconnect impedances. The EM simulation of the PCB is performed using HFSS, the Ansys full-wave solver. Considering the loop impedance seen from port 1, with ports 2, 3, and 4 in Fig. 4.20(a) short-circuited, while keeping the remaining ports in open condition, the impedance can be derived from the presented model as:

$$Z_{\text{loop}}^{\text{model}} = (Z_3^{\text{par}} + Z_4^{\text{par}}) // Z_2^{\text{par}} + Z_1^{\text{par}}. \tag{4.34}$$

Consistently, the impedance of the same loop was experimentally measured using a two-port probe P2102A across port 1, Bode 100 as vector network analyzer (VNA) and J2102B Common Mode Transformer to prevent ground loop problem blocking common mode current [149], following the shunt through methodology described in [150]. This setup allows a derivation of the impedance starting from S-parameters measurement [151]:

$$Z_{\text{loop}}^{\text{meas}} = \frac{Z_0 S_{21}}{2(1 - S_{21})} \tag{4.35}$$

where Z_0 is equal to the reference impedance.

The real and the absolute value of the imaginary parts of the impedance, divided by 2πf, are then compared leading to the results shown respectively in Fig. 4.22(a) and (b), demonstrating good agreement between the derived model and the measured data.

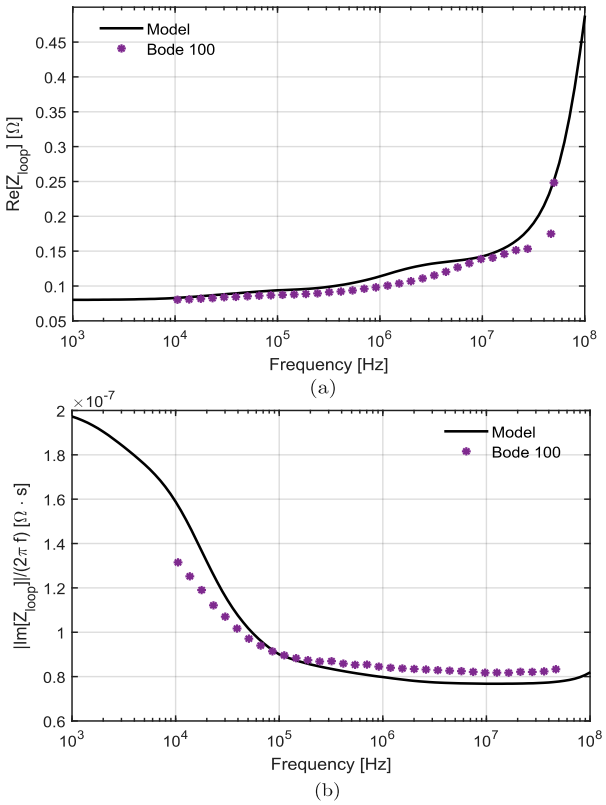


Fig. 4.22 (a) Comparison between measurement of the real part of the loop impedance and the one derived from the model, and (b) measurement of imaginary part of the loop impedance divided by 2πf and the model.

4.3 Broadband model

In this section, the results obtained from EM simulations carried out using the quasi-static and full-wave approaches previously presented, are reported and analyzed. The outcomes of the two methodologies are systematically compared with experimental measurements in order to assess their respective ranges of validity and applicability. This comparison highlights the transition from quasi-static to full-wave behavior and motivates the need for a broadband modeling approach. Accordingly, a broadband EM model is introduced, capable of accurately representing the system response over a wide frequency range. Furthermore, an effective technique for translating the developed broadband model from the frequency domain to the time domain is presented.

4.3.1 Measurement technique of low-impedance values

To determine which measurements method is most suitable to be employed, we can consider a simple system configuration consisting solely of a resistive load. Within this framework, three fundamental impedance-measurement techniques can be implemented using a Vector Network Analyzer [150].

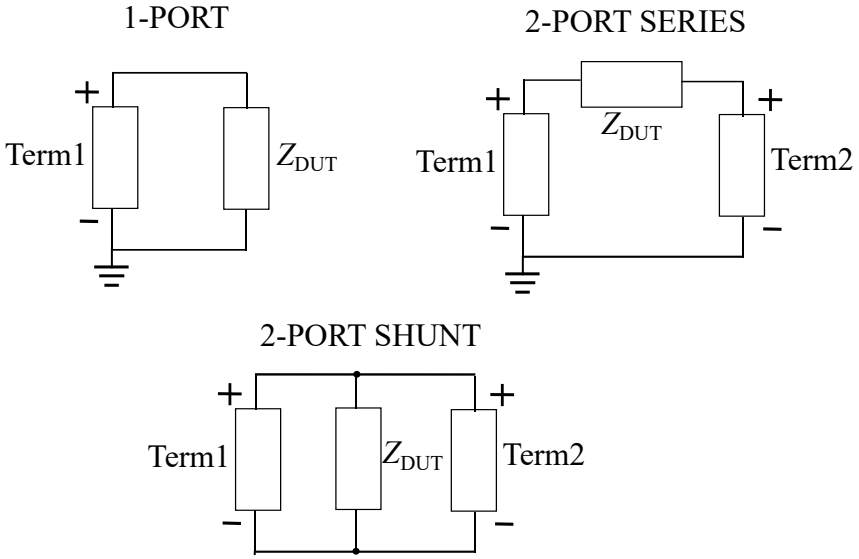


Fig. 4.23 Different configurations of impedance measurement for a DUT

- The 1-port reflection method, which relies exclusively on the measurement of the reflected signal S_{11} at a single port,
- the 2-port series, uses a two-port configuration in which the device under test is inserted in series between the ports,
- the 2-port shunt through techniques, where the device is connected in parallel between the two ports. In this case a model of common mode transformer is used to mitigate the ground loop problem that will be explained lately.

These techniques employ VNA ports to establish the required excitation and sensing conditions. The three different methods are depicted in Fig.4.23. A sweep of $S(Z_{DUT})$ across a broad range of DUT impedances can be simulated for each of these three configurations, and representative results are shown in Fig.4.24. In all cases, measurement sensitivity degrades as the magnitude of the relevant S-parameter

approaches 1, where small variations in impedance produce minimal observable changes.

Because we aim to characterize very low impedance values, the most appropriate approach is the 2-port shunt-through technique, which offers enhanced sensitivity and accuracy in the low-impedance regime. With this method we are capable of capturing very low impedance values up to very high frequencies [152].

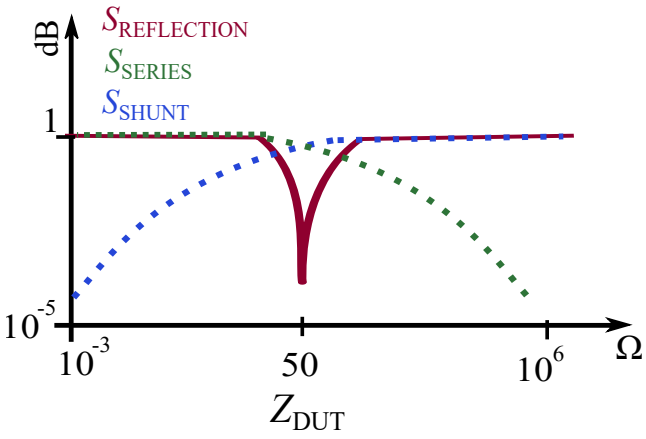


Fig. 4.24 Magnitude of S-parameter as a function of DUT resistance for the three different impedance measurements methods.

Therefore, the measurement can be implemented as represented in Fig.4.25, using the device of interest as Z_{DUT} and a VNA, in particular Bode 100 that works up to frequencies equal to 40 MHz and Rigol RSA 3030N, used for measurements at higher frequencies, starting from MHz range up to 3 GHz.

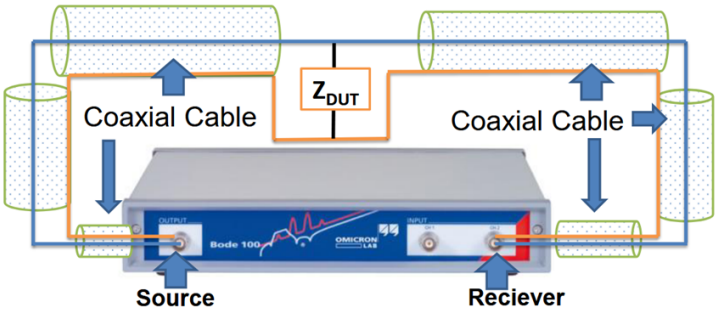


Fig. 4.25 Two-Port Shunt Through measurement with VNA, in this case with Bode 100. Pictures from [149].

Starting from this configuration we can derive the circuit representing the two port shunt-through method in Fig. 4.26, constituted by the model of the source with its internal impedance and the receiver. The DUT instead, is connected in parallel between these two ports.

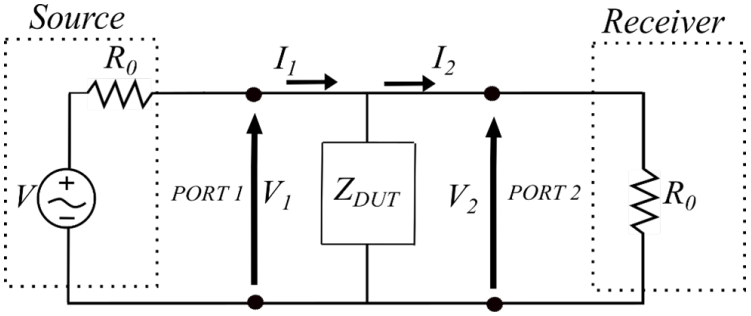


Fig. 4.26 Two-Port Shunt Through circuit configuration.

For a two-port network, the measured scattering parameters can be related to the impedance of the DUT, [149] [151]:

$$S_{21} = \frac{2V_2}{V_1 + I_1 Z_0} = \frac{2Z_{\text{DUT}}}{2Z_{\text{DUT}} + Z_0}, \tag{4.36}$$

from which the DUT impedance can be expressed as

$$Z_{\text{DUT}} = \frac{Z_0 S_{21}}{2(1 - S_{21})}. \tag{4.37}$$

Here, V_1 and V_2 denote the voltages at ports 1 and 2, respectively, and I_1 is the current entering port 1.

The transmission coefficient can be interpreted as the square root of the ratio between the power delivered to the receiver when the DUT is present and the power that would be delivered in its absence. Accordingly, S_{21} quantifies the fraction of power transmitted through the DUT relative to the reference condition. For a reference impedance $Z_0 = 50\,\Omega$, the extracted impedance can be approximated as

$$Z_{\text{DUT}} \approx 25\, S_{21}. \tag{4.38}$$

This relation indicates that higher transmitted (i.e., received) power corresponds to larger values of the transmission coefficient, and consequently to a higher extracted impedance.

Any increase in the received power is therefore reflected as an increase in the value of Z_{DUT}, which constitutes the fundamental mechanism underlying the ground loop problem.

In particular, the ground connection of the VNA introduces an unintended alternative current return path, leading to measurement inaccuracies. Furthermore, each cable exhibits finite losses, which can be modeled as parasitic resistances. Due to safety requirements, all ground connections within the VNA setup are electrically bonded, which further contributes to the formation of ground loops.

The ground connection of the VNA in facts, creates an unwanted alternative path for the current signal, resulting in a measurement error. Every cable will have cable losses which are marked as cable resistances in Fig. 4.27. Due to National Electrical Code (NEC) requirements for public safety, all ground connections within the VNA setup must be electrically bonded.

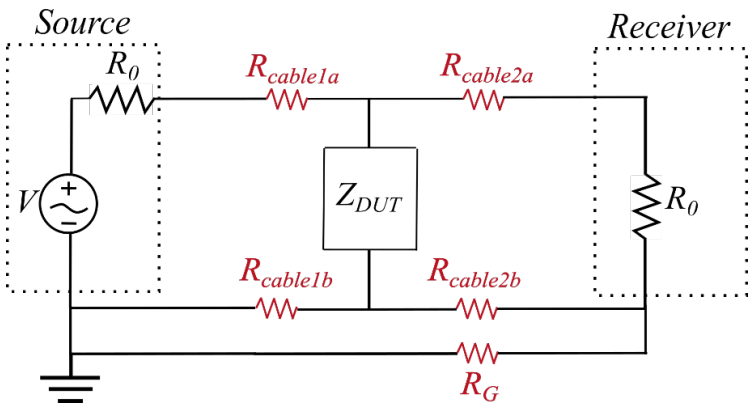


Fig. 4.27 Representation of ground loop problem with generation of common mode current.

This forms a ground loop in the 2-port shunt-through measurement as shown in Fig. 4.27. This Figure illustrates the alternative return path for the signal current, commonly referred to as the common-mode current. The presence of ground connections creates this path. If it were absent, the entire current would return exclusively through the cable. The added ground network therefore provides an

additional return path for current which depends upon the value of R_G. In almost all VNAs, $R_G \ll R_{cable1b}$ and $R_{cable2b}$. Consequently, the extra current becomes significantly larger than in the configuration without this supplementary return path. This current contributes additional power to the receiver, thereby increasing S_{21} and, consequently, the estimated $Z_{DUT} = 25 \cdot S_{21}$. This increase represents a measurement artefact and does not correspond to the true value of Z_{DUT}, thus, it must be regarded as an error. Two approaches typically adopted to mitigate this problem are the use of a coaxial transformer or a semi-floating differential amplifier [149, 153].

- **Coaxial common-mode transformer**: the first approach to mitigating ground loop issues involves the introduction of a high-quality common-mode transformer, often implemented as a coaxial transformer. As suggested by its name, this device is designed to suppress common-mode currents. The transformer is typically wound on a ferrite core in such a way that when $I_{out} = I_{in}$, the effective inductance presented to the current is negligible. This portion of the current, referred to as the differential current, is the component that contributes to normal circuit operation and VNA measurements. Conversely, any portion of the current that flows asymmetrically, i.e. through one path without returning through the corresponding return path, is classified as common-mode current. The common-mode transformer presents a very high inductive impedance to this undesired current, effectively blocking its flow. The degree of suppression, commonly called attenuation, is strongly dependent on the specific design and winding configuration of the transformer. To ensure that normal measurement operation remains the same, the transformer is engineered so that the differential current sees a nominal impedance of 50Ω, not affecting normal VNA measurements operation. A critical practical consideration is that, being a transformer, the device is inherently ineffective at DC. Experimental results indicate that commercially available models, such as the Picotest J2102A, operate effectively at frequencies above approximately 3 kHz, although this threshold can vary depending on cable length and electrical properties. The upper frequency limit for effective common-mode suppression is determined by the ferrite core material and its quality factor, which sets the bandwidth over which the transformer maintains high attenuation of common-mode signals.

- **Semi-floating differential amplifier**: the second approach to addressing the ground loop problem involves the implementation of a semi-floating differential amplifier within the measurement setup. This type of amplifier is specifically designed to present a very high resistance to common-mode currents, thereby significantly reducing the flow of unwanted currents that could otherwise distort measurement results. Unlike common-mode transformers, which are inherently ineffective at DC due to their transformer-based design, the semi-floating differential amplifier remains effective across the entire frequency spectrum, including DC.

For the presented measurement setup, to address the issue associated with ground loop problems, the Picotest J2102B common mode transformer is inserted to block the common mode current.

Once the value of Z_{DUT} has been accurately determined through the measurement procedure, it becomes possible to derive the parasitic resistance and inductance by extracting, respectively, the real and imaginary part of the obtained impedance:

$$R = \Re\{Z_{\mathrm{DUT}}\}, \qquad L = \frac{\Im\{Z_{\mathrm{DUT}}\}}{2\pi f}. \tag{4.39}$$

To perform a comprehensive and detailed analysis of the parasitic elements, a customized 2 layer PCB has been developed, with a substrate made of FR4 and a thickness of 1.6 mm, a copper trace with a height of 0.035 mm, 1.8 mm width and a length of 770 mm; at the ends of the trace, vias are employed to provide a connection to the underlying ground plane. In order to correctly measure the impedance of the trace a shunt through measurement is performed, which is the standard method capable of capturing very low impedance values up to very high frequencies [154, 155]. With this methodology, S-parameters are measured using Vector Network Analyzer, in particular Bode 100 that works up to frequencies equal to 40 MHz and Rigol RSA 3030N, used for measurements at higher frequencies, starting from MHz range up to 3 GHz. To address the issue associated with ground loop problems, the common mode transformer is inserted to block the common mode current. The described test configuration is illustrated in Figure 4.28.



Fig. 4.28 Measurement setup with Bode 100 (and Rigol RSA 3030N) as VNA, J2102B Common Mode Transformer, 2-port probe P2102A and PCB layout.

For the comparison with simulation results, both the quasi-static tool, Q3D, and the full-wave one, HFSS, from Ansys environment, were employed to achieve accurate solutions across different operating conditions. The first one was used under the low-frequency approximation previously explained, whereas the latter was adopted to accurately model the electromagnetic behavior at higher frequencies.

To obtain the self-inductance/resistance values between the sink and each source, with the Ansys quasi-static simulator, methodology described in Sec. 4.1.2 is adopted. With the full-wave simulator, loop values of parasitic components are obtained starting from the matrix of Y-parameters as detailed in Sec. 4.2.2. In this condition, the parasitic values of inductance and resistance of the described PCB are measured and simulated.

As illustrated in Figure 4.29, the results of the low frequencies simulation with Q3D align perfectly with the experimental measurements with Bode 100. Instead, when the frequency is higher than $v_p/(10d) \approx 20\,\text{MHz}$, where $v_p = c/\sqrt{\varepsilon_r}$ is the propagation velocity in a medium, with c equal to the speed of light and ε_r is the relative dielectric constant of FR4, the quasi-static limit is exceeded and the measurements performed with the Rigol VNA closely match the HFSS results, which, by contrast, at low frequencies exhibit a relative error between 20%-40% for inductance and resistance values.

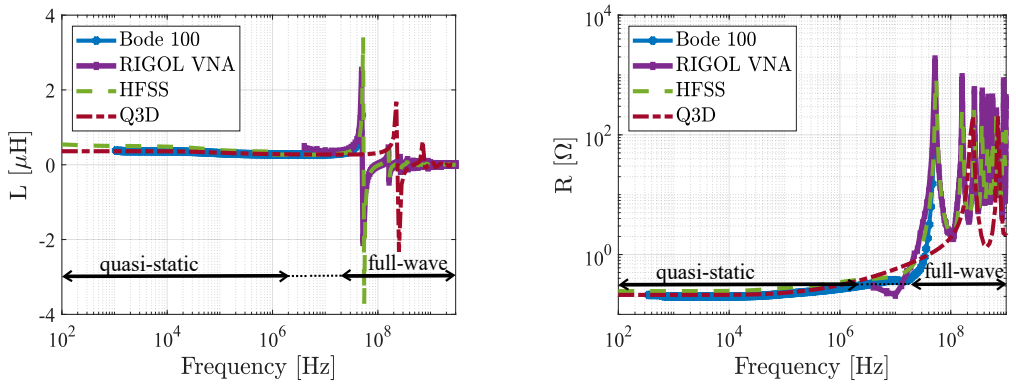


Fig. 4.29 Comparison between parasitic (a) inductance and (b) resistance of the described PCB, obtained with measurement using Bode 100 and Rigol RSA 3030N VNA and with simulation employing Q3D and HFSS.

4.3.2 Model derivation

A general and rigorous procedure is required to ensure simulation results are accurate and meaningful within the context of the specific application under investigation. Considering the need to employ commercially available EM solvers for a practical and computationally feasible analysis, it thus becomes evident that, given the inherent validity constraints of each solver, adopting a multi-tool strategy is essential to obtain an accurate model over a wide frequency range. The results obtained from quasi-static and full-wave solvers must be combined to construct a unified description valid over the entire frequency range of interest. It can subsequently be transformed into a time-domain model, to perform transient co-simulation with circuit level components, requiring that the resulting netlist accurately preserves the original frequency-domain behavior to ensure reliable results.

The novel workflow can therefore be defined as schematized in Figure 4.30.

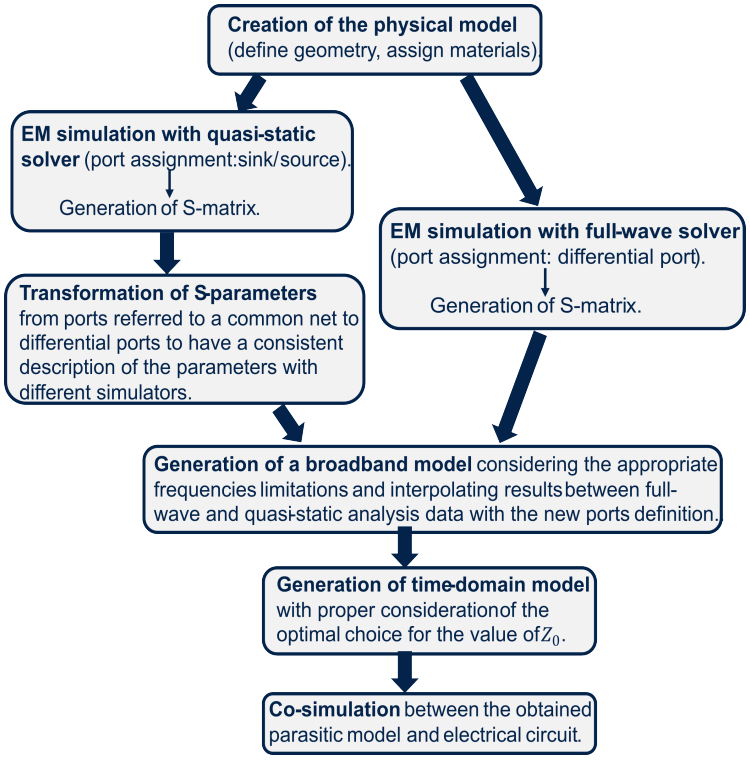
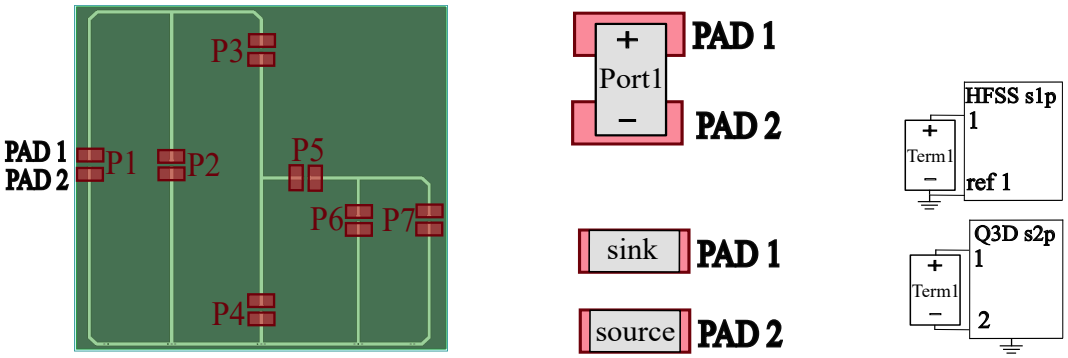


Fig. 4.30 Proposed flow for the generation of an accurate time-domain model of parasitic suitable for SPICE-like circuit simulation.

A second PCB, with the same material definition, trace width and thickness as the previous one, is then realized to consider a n-port device (Figure 4.31-a), where, in this case, n is equal to 7. As in the previous case, for the EM analysis, differential ports are set in HFSS, while in Q3D a sink or a source is located where in the full-wave solver the positive and negative terminal of the differential port is present (Figure 4.31-b). Therefore in HFSS an S-matrix with n differential ports is obtained, while the port configuration in Q3D leads into a 2n ports S-matrix referred to a common net. To transform the Q3D matrix in the same format as HFSS, the Keysight tool ADS is used and the new S-parameters are extracted forcing the reference net of the terminal to the corresponding sink or source present in the Q3D EM simulation (Figure 4.31-c). In this way a model directly comparable with HFSS is obtained, the S-matrices from the two different tools are now described in the same format, and it is possible to generate a broadband model valid from DC to GHz, using a hybrid approach.

The matrix of S-parameters extracted with Q3D is employed for the low-frequency region, while the matrix extracted with HFSS is adopted for the high-frequency region. In order to correctly combine the two systems, Q3D data are considered starting one decade before the quasi-static limit equal to $v_p/(10d)$ to ensure the validity of low-frequency data. Beyond this limit we can also ensure that HFSS data are correct since the low-frequency breakdown problem is no longer present. The intervals under consideration are highlighted in Figure 4.29. In the remaining decade of frequencies between these two systems, spline interpolation is applied to provide a smooth and precise transition between the values, ensuring the connection of the two systems is continuous and consistent. This procedure enables the derivation of a model composed of a single S-matrix that accurately characterizes the system behavior across the entire frequency range.



(a) (b) (c)

Fig. 4.31 (a) N-ports PCB, and different port configuration, considering one port as example, between (b) HFSS and Q3D for EM analysis and (c) ADS for the translation in the same format.

4.3.3 Time-domain model

The last step required to enable time-domain simulation is the transformation of the model from frequency to time domain. This final part of the workflow ensures that the system can be accurately integrated into circuit simulators that operate in time domain, such as SPICE-based tools. The S-parameters data must then be verified for passivity, as non-passive models can lead to instability in time-domain simulations. Additionally, causality must be preserved, which is necessary to maintain its physical

meaning. Moreover, it is essential that the transformation guarantees a high level of accuracy of the system behavior, otherwise the reliability and performance of the model are compromised.

To this end, simulators capable of converting S-parameters into their time-domain representation must be employed. In order to achieve an accurate conversion, let us make some considerations. According to [148] the reflection coefficient can be written as:

$$S_{ii} = \frac{Z_{\text{in}}^{(i)} - Z_0}{Z_{\text{in}}^{(i)} + Z_0} \tag{4.40}$$

with $Z_{\text{in}}^{(i)}$ equal to the input impedance at port i looking into the matching section.

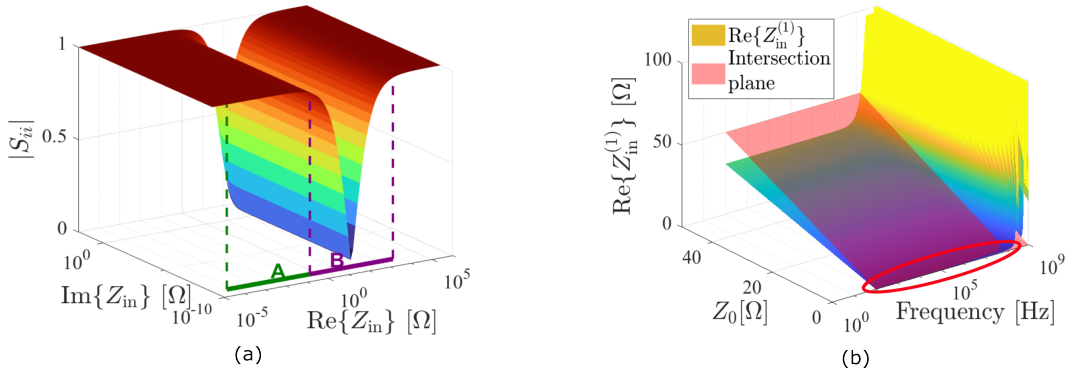


Fig. 4.32 (a) Magnitude of the variation of the reflection coefficient S_{ii} in (4.40) varying the real and imaginary part of Z_{in}, fixing the reference impedance Z_0 to 50 Ω. (b) Variation of the real part of Z_{in} looking from port P1 (Fig.4.31-a) as a function of frequency, varying Z_0, and intersection with plane Z=Z_0 highlighted in red.

In Figure 4.32-a, the behavior of S_{ii} in (4.40) is illustrated by fixing the reference impedance to 50 Ω while varying both the real and imaginary components of Z_{in}. It is evident that the behavior of the reflection coefficient is strongly influenced by variations in the real part of Z_{in}. Specifically, when that quantity becomes much larger than the value of Z_0, as highlighted in the region labeled as 'A', the magnitude of the reflection coefficient consistently converges towards 1. As a result, values of the real part of $Z_{\text{in}}^{(i)}$ very different from the each other lead to very similar values of the magnitude of S_{ii}. Instead, when the real part of $Z_{\text{in}}^{(i)}$ approaches the reference impedance value, as depicted in the second region 'B', a bending occurs in the curve representing $|S_{ii}|$, meanwhile the increase of its imaginary part determines

a slight increase in the reflection coefficient amplitude. Therefore, the range of the represented S-parameter expands significantly. In a different point of view, the precision required during the fitting process strongly depends on the region in which the analysis is performed. Let us estimate the resolution associated with the fitting process by computing the difference between the minimum and the maximum quantity of the absolute value of the reflection coefficient in each region:

$$\delta_{S_{ii}} = (|S_{ii}|_{\max} - |S_{ii}|_{\min}) \cdot \varepsilon_{\%}. \tag{4.41}$$

A tolerance factor ε, expressed as a percentage of this range, is applied to reflect the desired level of precision required for the model. Considering $\varepsilon_{\%} = 0.01$ and assuming both regions cover the same number of decades (i.e. region 'A': $5 \cdot 10^{-5}$-$5 \cdot 10^{-1}$ Ω, and region 'B': $5 \cdot 10^{-1}$-$5 \cdot 10^{3}$ Ω), we can compute $\delta_{S_{ii}}$ that is the value we require to set in the fitting process as absolute tolerance. In the first region it is approximately equal to $1.8 \cdot 10^{-4}$, instead in the second region $\delta_{S_{ii}} \approx 1.8 \cdot 10^{-2}$. It is clear that this second option substantially reduces the required tolerance error, maintaining the same precision of the fitted parameters. Thus, the optimal value of Z_0 to be selected during the creation of the model is such that it closely approaches the real part of Z_{in}. Relaxing the tool error tolerance during the fitting process, is not only beneficial in terms of numerical simulation, but also results in a less complex time-domain circuit netlist, conversely increased structural complexity may lead to a violation of the constraints on passivity and, in turn, could prevent the final simulation to converge. Additionally, the tool may not be able to achieve the level of precision required in the first region, degrading model accuracy.

A critical aspect is that the value of Z_{in} is influenced by the specific circuit configuration and the selected value of the reference impedance used to terminate the other ports during its computation. Consequently, once the S-parameters have been obtained from the EM simulation, it is possible to see Z_{in} variation for each port i, by changing the reference impedance of the derived S-parameters and then the input impedance value can be evaluated by inverting equation (4.40). Taking as example the broadband S-parameters previously derived from the EM analysis of the n-port PCB, in Figure 4.32-b it is possible to observe the behavior of the real part of $Z_{\text{in}}^{(1)}$ varying the frequency and the reference impedance Z_0. Intersecting this

curve with a plane equal to the reference impedance magnitude, that is the one used in the computation of the S-parameters from which $Z_{\text{in}}^{(1)}$ was derived, it is possible to identify a region outlined in red, before the system approaches its resonance frequency, in which it is more advantageous to select the reference impedance value during the fitting process, since the quantities corresponding to the real part of the input impedance and to Z_0 are close to each other.

In this way, it is possible to optimize the process and reduce the fitting error during the transformation of the parameters from frequency to time domain. As a consequence, the procedure can be more effectively controlled, allowing for improved precision in the generation of the model and leading to an overall increase in the reliability of the results.

Moreover, the controlled fitting workflow adopted in this work—based on reference impedance adjustment to improve accuracy—can be directly implemented within IdEM. The tool provides an interactive matrix interface that allows real-time monitoring of the S-parameter evolution induced by variations in the reference impedance Z_0, enabling a precise assessment of its impact on both model fidelity and structural complexity.

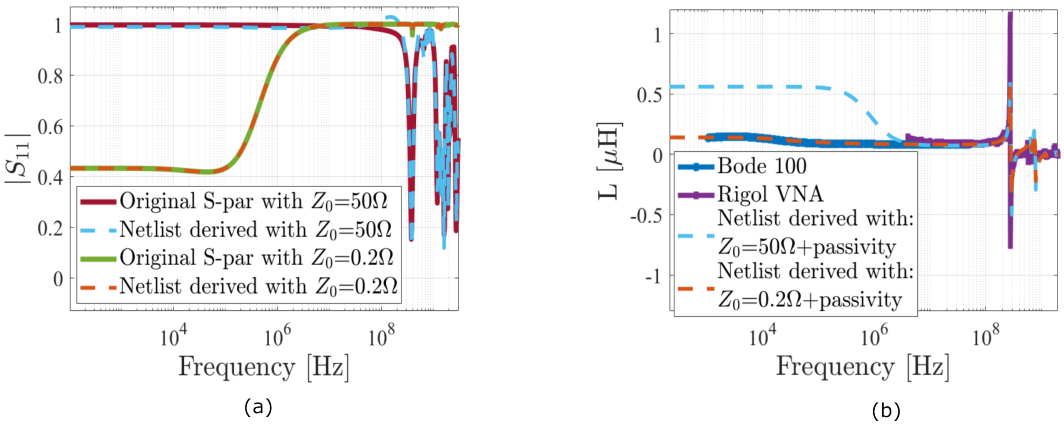


Fig. 4.33 (a) Comparison between original and derived S-parameters obtained from the time-domain netlist when Z_0 is equal to 50Ω and when it is close to Z_{in} seen from port P1 (Fig.4.31-a). (b) Comparison of the parasitic inductance estimated from measurements with Bode 100 and Rigol VNA and evaluated from the netlist with different Z_0, after ensuring passivity for both.

Finally a comparison between the derived model and measurements is carried out, with the aim of experimentally validating the model and verifying its accuracy. The 2-port shunt through method is applied to the n-port PCB, placing the 2-port probe across the positive and negative terminal of port 1, considering the port definition in Figure 4.31-a, short-circuiting ports 2,3,4 and leaving the other ports open, to isolate and make a comparison of the parasitic contributions of the remaining portion of the loop. As in the case of the 1-port PCB, the values of parasitic components are obtained starting from the measurement of the parameter S_{21}. For the simulation results, instead, the previously derived broadband model is adopted, and the software IdEM was employed for the generation of the time-domain netlist. As illustrated in Figure 4.33-a, two netlist are derived using different reference impedances. For Z_0 equal to $50\,\Omega$ the magnitude of the represented S-parameter remains close to 1 below the resonance frequency. As a consequence, minor fitting variations in the S-parameter cause significant changes in the extracted parasitics value. Hence, higher tool accuracy is required, resulting in a more complex and non-passive netlist. Conversely, the second netlist derived using an optimal value of Z_0, yields a passive and accurate model. Enforcing passivity, thus, becomes necessary for the first netlist, resulting, however, in a further reduction of accuracy, which can be observed in Figure 4.33-b, where the parasitic inductance derived from the models are compared with measurements. The proposed technique, instead, accurately describes the behavior of parasitic components throughout the entire frequency range, with reliable results even after the transformation of S-matrix into time domain, oppositely if Z_0 is not properly selected the accuracy degrades significantly.

A circuit suitable for time-domain simulator is consequently obtained and can be used in transient analyses by connecting it to the electrical components, allowing co-simulation between pure circuit schematic and EM simulation results.

Taking a practical case of study as an example, the equivalent circuit of the described n-port PCB can be employed for a detailed analysis of a DC-DC buck converter design. An analogous representation of the standalone converter is obtained, as can be seen in Figure 4.34, wherein now the broadband parasitic model is also included by attaching all electrical components to it, and the voltage at each port corresponds to the voltage across the connected component [155, 156]. It is now possible to carry out time-domain simulations to achieve a precise and optimized

design of the device. Observing the voltage waveform across the inductor allows for the identification of the contribution of parasitic elements to voltage overshoots and high-frequency ringing, particularly during switching transients. In the same way, it is possible to analyze the voltage spikes that occur across critical components such as the transistors and the diode. This, in turn, enables a more accurate evaluation of whether these devices are operating within their respective Safe Operating Areas (SOA). Moreover, computing the voltage and current across the switching element with the inclusion of parasitic effects allows for a more realistic estimation of power losses, which are essential for thermal management and efficiency optimization. It is also possible to better evaluate the output voltage ripple for selecting appropriate output filtering components and ensuring stable operation of the converter. Finally, accurately modeling input current allows for an effective design of input electromagnetic interference filter, ensuring compliance with electromagnetic compatibility standards.

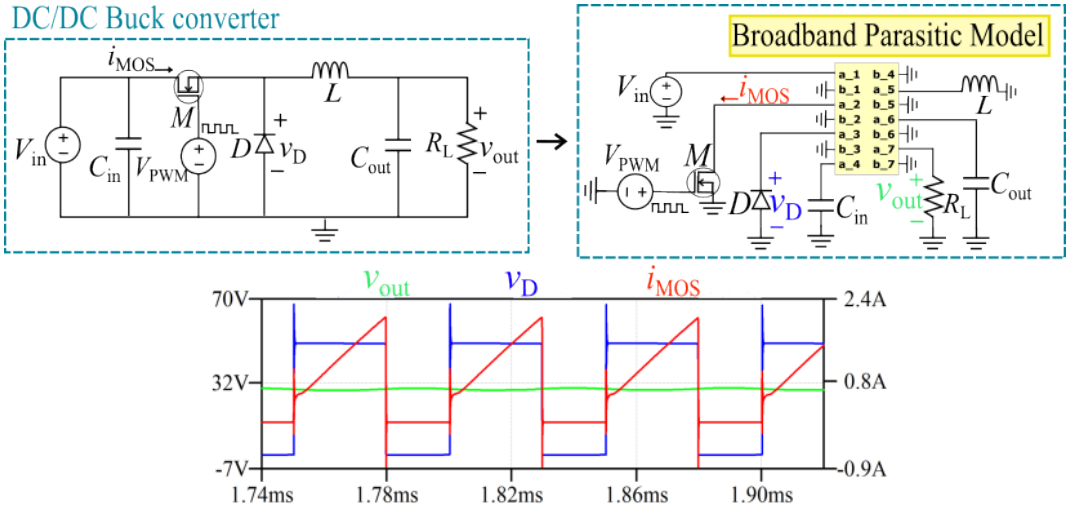


Fig. 4.34 Schematic of Buck converter and final equivalent model adding the netlist that reproduce EM simulation results. With this approach co-simulation between pure electrical and parasitic components can be performed within a time-domain simulator, in this case LTspice is employed and main voltage and current waveforms of the converter are represented.

Chapter 5

Near-field magnetic probing

This chapter addresses the relevance and application of near-field measurement techniques for the analysis of electromagnetic emissions in DC–DC converters. The focus is placed on the use of magnetic near-field microprobes as an effective tool for investigating current-driven radiation mechanisms that dominate in switched-mode power circuits.

The experimental procedure for performing near-field measurements using magnetic microprobes is detailed, with particular attention to the acquisition of spatially resolved magnetic field distributions above the surface of the device under test (DUT). By systematically scanning the probe over a predefined area, magnetic field maps are obtained, enabling localization of dominant emission regions and identification of critical current paths.

A key aspect of this methodology is the direct comparison between measured near-field data and full-wave EM simulation results. Such a comparison enables early-stage validation of design choices, assessment of shielding and layout solutions, and evaluation of mitigation strategies prior to physical prototyping. To establish and verify the consistency between the measurement environment and the numerical reconstruction approach, a transmission line (TL) is initially adopted as a simplified and well-controlled reference structure. This preliminary example provides a clear framework for correlating experimental observations with simulated field distributions before extending the methodology to more complex DC–DC converter topologies.

5.1 Near-field analysis

As discussed in the previous chapters, the early consideration of electromagnetic effects is essential for the accurate prediction and mitigation of conducted emissions in DC–DC converters. In particular, EM simulations have proven to be tool for analyzing the impact of parasitic elements and layout-dependent phenomena on converter waveforms, switching behavior, and conducted noise generation.

In an analogous manner, the same design strategy applies to radiated emissions. The electromagnetic phenomena responsible for conducted interference, as high di/dt current loops, fast switching transitions, and parasitic inductive and capacitive couplings—also represent the primary sources of near-field radiation in switched-mode power converters. To mitigate these effects, a variety of shielding and design techniques have been introduced at both the package and system levels. However, in many industrial development workflows, the effectiveness of these countermeasures is assessed only during the final validation stages. This process typically involves redesigning critical parts of the system, re-fabricating hardware, and performing additional measurement campaigns. These iterative loops introduce significant overhead in terms of development time, validation effort, and overall project cost.

Consequently, radiated EMI cannot be regarded as an independent post-validation issue, but rather as an extension of the EM behavior of the device. For this reason, near-field analysis is introduced as an additional approach to completely characterized the EM behavior of the system.

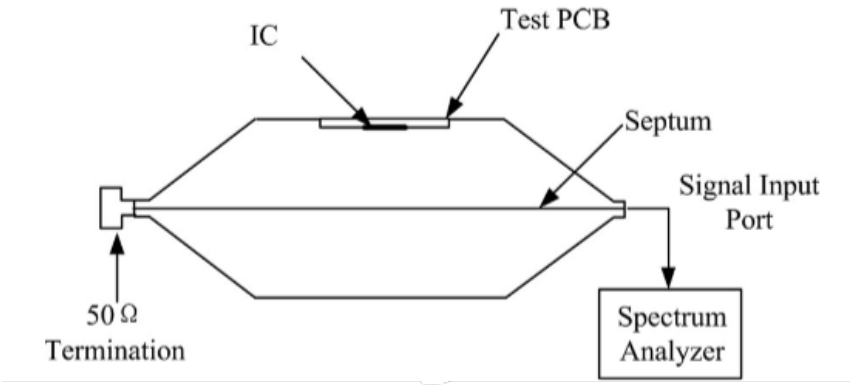


Fig. 5.1 TEM cell measurement standard setup. Picture from [157].

Therefore, in early design and pre-compliance phases, radiated emission verification are commonly performed using Transverse Electromagnetic (TEM) cells. This approach is widely adopted due to its straightforward implementation: the device under test is positioned within the cell, measurements can be conducted with limited instrumentation complexity, and the electromagnetic environment is highly repeatable and well controlled.

From a structural and electromagnetic standpoint, the TEM cell, depicted in Fig. 5.1, can be regarded as a closed transmission-line structure. It consists of an outer conductive enclosure acting as the return path and an inner conductor, commonly referred to as the septum, which serves as the signal line. The septum is connected to the input and output ports of the cell and is designed in order that the characteristic impedance of the structure is typically maintained at 50Ω. The TEM cell supports a fundamental TEM mode, in which the electric and magnetic fields are ideally transverse to the direction of propagation, with a well-defined polarization determined by the cell geometry. This measurement configuration is particularly well suited for the characterization of simple radiating structures, such as electrically small dipole antennas. In this case, the antenna can be precisely aligned with the known electric-field vector inside the cell, ensuring controlled and repeatable excitation conditions. Since electrically small dipoles exhibit a response proportional to the projection of the incident electric field onto their effective length vector, the fixed polarization of the TEM field enables consistent characterization of their radiation behavior.

However, when more complex DUTs are considered, the applicability of TEM cell measurements becomes limited. Integrated circuits, power converters, and multilayer packages exhibit radiation mechanisms that are generally unknown *a priori*, often involving multiple current paths, loop structures, and coupling modes. In these cases, the fixed polarization of the TEM mode represents a significant constraint. The TEM cell does not allow for the separation of the electric and magnetic field components, preventing an independent characterization of each field contributions. Moreover, the enclosed nature of the TEM cell environment limits direct correlation with free-space radiation behavior, as boundary conditions and field distributions differ substantially from those encountered in realistic operating scenarios. These aspects reduce the suitability of TEM cell measurements for detailed EMI analysis.

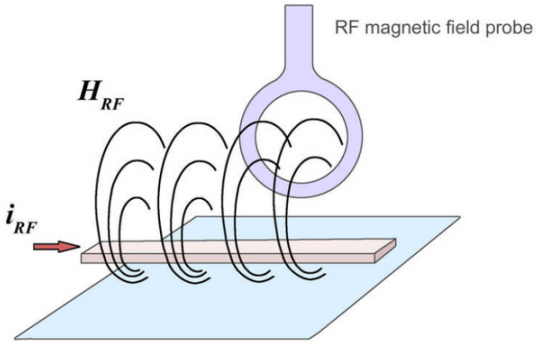


Fig. 5.2 Magnetic field detection with microprobe. Picture from [158].

To address these limitations, near-field measurement techniques based on electric and magnetic microprobes have gained increasing relevance. Near-field probes allow local sampling of the EM field in close proximity to the DUT surface, as represented in Fig. 5.2 enabling localized and independent measurement of electric and magnetic field components. By scanning the probe across a defined area, spatially resolved field distributions can be obtained, providing a direct vision of the localization and intensity of emissions.

For magnetic near-field probes, the measured quantity is closely related to the local current distribution on the DUT, since the magnetic field intensity is governed by Ampère's law. As a consequence, near-field magnetic measurements provide an effective means to analyze current-driven radiation mechanisms, particularly those associated with localized current loops and return paths.

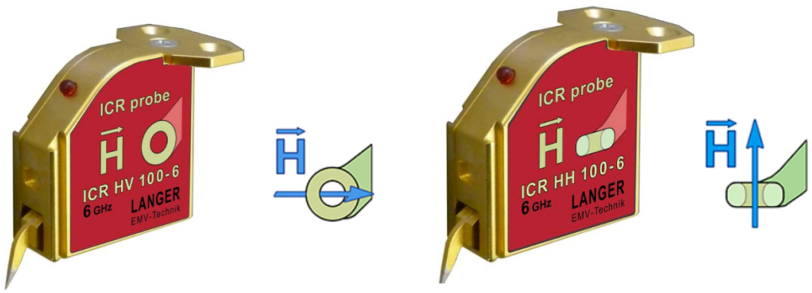
This approach is especially relevant for switched-mode power applications, notably DC–DC converters. The resulting current loops in power stages, gate drivers, and decoupling networks onstitute some of the dominant sources of radiated EMI. Consequently, magnetic near-field emissions are strongly correlated with layout-dependent current paths, making them particularly suitable for investigation using near-field magnetic probes.

By combining near-field measurements with EM simulations, it becomes possible to perform emission analysis at an early stage of the design process. Spatial field maps measured on the DUT surface can be directly compared with simulated

field distributions, enabling validation of modeling assumptions and identification of critical emission sources. Moreover, this methodology allows for systematic evaluation of layout modifications, shielding strategies, and filtering solutions before finalizing the hardware design. In the context of DC–DC converters, this approach provides a practical framework for reducing radiated EMI while preserving converter performance and power efficiency.

5.2 Experimental setup and measurement technique with magnetic micro-probe

Magnetic near-field measurements can be performed using different types of probes, whose sensitivity depends on the orientation of the probe loop with respect to the surface of the DUT. In general, magnetic near-field probes can be classified into horizontal and vertical probes, according to the orientation of the loop plane.



(a) (b)

Fig. 5.3 Langer microprobe with (a) vertical orientation and (b) horizontal orientation.

- Vertical magnetic probes, as shown in Fig. 5.3(a), are characterized by a loop whose plane is perpendicular to the DUT surface. In this configuration, the probe is mainly sensitive to the magnetic field components parallel to the surface, typically H_x or H_y, depending on the probe orientation. These probes are particularly effective for detecting magnetic fields associated with vertical current paths, vias, or interconnections that generate lateral magnetic field components.

- Conversely, horizontal magnetic probes, in Fig. 5.3(b), feature a loop oriented parallel to the DUT surface. This configuration leads to a primary sensitivity of the probe to the magnetic field component normal to the surface. Assuming a Cartesian coordinate system where the DUT lies in the x–y plane, horizontal probes are predominantly sensitive to the H_z component of the magnetic field. This characteristic is particularly advantageous for the investigation of PCB and integrated modules, where dominant radiation mechanisms are often associated with planar high-frequency current loops.

Magnetic near-field probes are commonly classified according to their geometrical configuration, orientation with respect to the DUT, and electrical bandwidth. These characteristics determine the probe sensitivity, spatial resolution, and applicability to different classes of electromagnetic emission mechanisms.

In the case of commercially available probes from Langer EMV-Technik, the probe model designation follows a standardized nomenclature of the form `HH XXX-Y`. Each element of this designation conveys specific information regarding the probe characteristics.

The first letter '`H`' indicates that the probe is sensitive to the magnetic field component of the EM field, as opposed to electric-field probes, which are denoted by the letter '`E`'. The second letter specifies the orientation of the probe loop with respect to the DUT surface. In particular, '`H`' denotes a horizontal orientation of the loop, while '`V`' refers to a vertical orientation. The numeric value '`XXX`' represents the diameter of the probe loop expressed in micrometers. The loop diameter is a key parameter governing the trade-off between spatial resolution and measurement sensitivity. Smaller loop diameters provide higher spatial resolution, enabling precise localization of small emission sources and narrow current paths. However, this improved spatial selectivity comes at the expense of reduced sensitivity, since the magnetic flux coupling is limited by the smaller loop area. Conversely, probes with larger loop diameters integrate the magnetic field over a wider spatial region, resulting in higher sensitivity but reduced spatial resolution. Finally, the suffix '`Y`' denotes the upper frequency limit of the probe expressed in gigahertz. This parameter defines the bandwidth over which the probe response can be considered valid and is

particularly relevant for measurements involving fast switching edges and broadband spectral content.

The selection of a specific probe model therefore depends on the expected spatial extent of the emission sources, the magnitude of the magnetic field to be measured, and the frequency range of interest. In practical measurement campaigns, it is common to employ probes with different loop diameters in order to balance spatial resolution and sensitivity according to the specific objectives of each analysis.

In the analysis presented in this work, a LANGER HH 100-6 magnetic near-field probe was employed, to achieve high spatial resolution in the investigation of localized emission sources. In particular, the reduced loop diameter of 100 μm allows the magnetic field to be sampled over a limited area, thereby minimizing spatial averaging effects and enabling improved spatial localization of small current loops and narrow fast-switching current paths, which are characteristic of switched-mode power converters. The operational bandwidth, extending up to 6 GHz, enables the capture of both the switching frequency of the DC–DC converter and the high-frequency spectral components generated by fast switching transients and parasitic resonant phenomena.

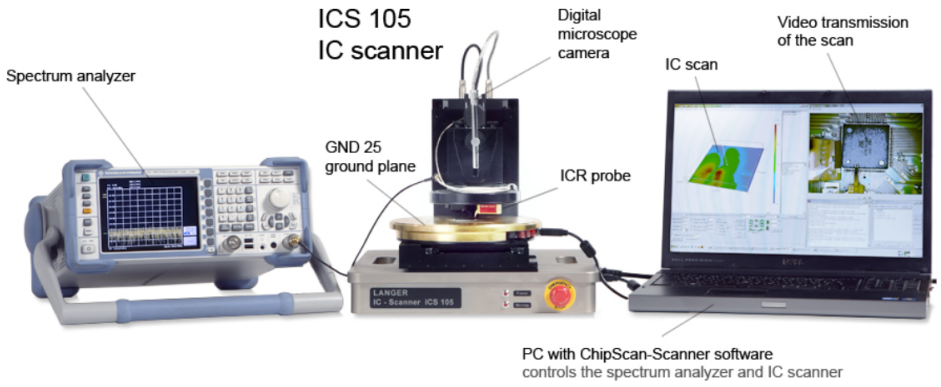


Fig. 5.4 Complete setup of measurment using microprobe and IC scanner, from [158].

The complete near-field measurement system consists of four main elements, as represented in Fig. 5.4: a spectrum analyzer, an automated scanning system, the device under test, and the control and acquisition software.

- Spectrum analyzer: the near-field probe is connected to a spectrum analyzer via a coaxial cable. The spectrum analyzer measures the voltage induced at the probe output and provides frequency-domain information on the emission amplitude.

- IC scanner: to achieve accurate and repeatable spatial mapping of the magnetic field, the probe is mounted on an automated positioning system. The scanner enables precise movement of the probe along the x and y directions parallel to the DUT surface. The user can define the boundaries of the scanning area, as well as the spatial step size, allowing control over the spatial resolution of the measurement.

  In addition to planar scans, the system supports vertical displacement of the probe along the z-axis. This capability makes it possible to perform measurements at different heights above the DUT surface, enabling three-dimensional characterization of the near-field distribution and analysis of field decay with distance.

- DUT: it is placed on the measurement platform and connected to a signal generator or appropriate power source, depending on the application. The excitation ensures that the DUT operates under controlled and reproducible conditions representative of normal operation. For power electronic circuits such as DC-DC converters, this typically involves applying nominal input voltage and load conditions to excite realistic switching behavior and current transients.

- ChipScan scanner: the coordination of probe movement and measurement acquisition is handled by the scanner software. Through the tool interface, the user defines the scanning coordinates, step size, measurement plane height, and acquisition parameters. For each probe position, the software synchronizes probe placement with spectrum analyzer measurements and records the corresponding spectral data.

  The acquired measurements are stored as spatially indexed datasets, enabling post-processing and visualization. ChipScan allows direct generation of two-dimensional near-field emission maps, where the measured magnetic field

intensity is represented as a function of spatial position. These maps provide a visualization of emission hotspots and dominant current paths on the DUT surface.

Following the definition of the measurement setup, it is necessary to relate the acquired measurement data to the physical quantity of interest. Although the near-field microprobe is employed to investigate the magnetic field distribution around the DUT, the quantity directly measured by the instrumentation is an electrical voltage rather than the magnetic field itself.

Specifically, the near-field magnetic probe operates as an inductive sensor, with its output voltage generated by the time-varying magnetic flux enclosed by the probe loop surface. This voltage is transmitted to the spectrum analyzer via a coaxial connection and constitutes the primary observable of the measurement system. A theoretical description is therefore required to establish the relationship between the measured voltage and the local magnetic field intensity in the vicinity of the DUT.

This relationship is derived by expressing the probe output voltage in terms of the magnetic flux through the loop surface. In particular, the output voltage is proportional to the time derivative of the magnetic flux, according to Faraday's law of electromagnetic induction, which states that the induced voltage V_{probe} is given by

$$V_{\text{probe}} = -\frac{d\Phi_B}{dt}. \tag{5.1}$$

where Φ_B denotes the magnetic flux. The magnetic flux through the loop is defined as the surface integral of the magnetic flux density $\mathbf{B}$:

$$\Phi_B = \int_S \mathbf{B} \cdot d\mathbf{S}. \tag{5.2}$$

In the near-field region above the DUT, the magnetic flux density is related to the magnetic field intensity $\mathbf{H}$ through the constitutive relation

$$\mathbf{B} = \mu_0 \mathbf{H}, \tag{5.3}$$

where μ_0 is the permeability of free space.

Under the assumption that the electromagnetic field can be considered approximately uniform over the small loop area (i.e., the loop dimensions are much smaller than both the wavelength and the spatial variation scale of the field), the induced voltage can be expressed as proportional to the time derivative of the average magnetic field component normal to the loop surface. In the frequency domain, this leads to a linear relationship between the measured voltage magnitude and the magnetic field intensity H.

In detail, considering (5.1), (5.2), (5.3), the measured voltage is given by:

$$V_{\text{meas}} = -\frac{d}{dt}\iint_S \mu_0 \mathbf{H} \cdot d\mathbf{S}, \tag{5.4}$$

where S denotes the area enclosed by the probe loop.

Moving to the frequency domain,the time derivative operator corresponds to multiplication by $j\omega$, yielding:

$$V_{\text{meas}} = -j\omega\mu_0 \iint_S \mathbf{H} \cdot d\mathbf{S}. \tag{5.5}$$

If the magnetic field can be assumed approximately constant over the loop area, the surface integral can be approximated as:

$$\iint_S \mathbf{H} \cdot d\mathbf{S} \approx S H_{\text{avg}}, \tag{5.6}$$

where H_{avg} denotes the average component of the magnetic field normal to the loop surface.

This leads to the following relationship between the measured voltage and the magnetic field:

$$V_{\text{meas}} = -j\omega\mu_0 S H_{\text{avg}}. \tag{5.7}$$

This expression highlights that, in the frequency domain, the probe output voltage is linearly related to the magnetic field intensity through a frequency-dependent transfer function proportional to $j\omega$ and to the loop area.

This relationship enables conversion of the voltage measured by the instrumentation into an equivalent magnetic field value.

5.3 Reconstruction of measurement output by EM simulation

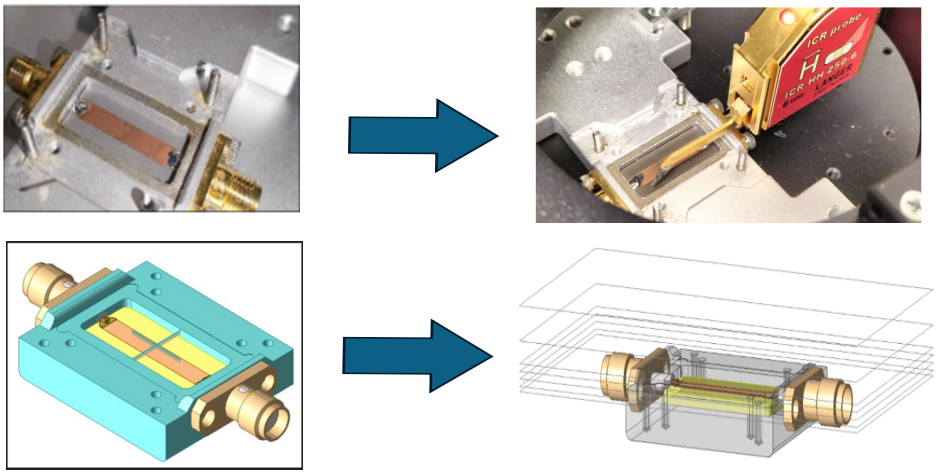


Fig. 5.5 Test line on a Mini TEM cell used for H field measurement with microprobe and creation of the physical model in HFSS and the same plane used in the scanning environment.

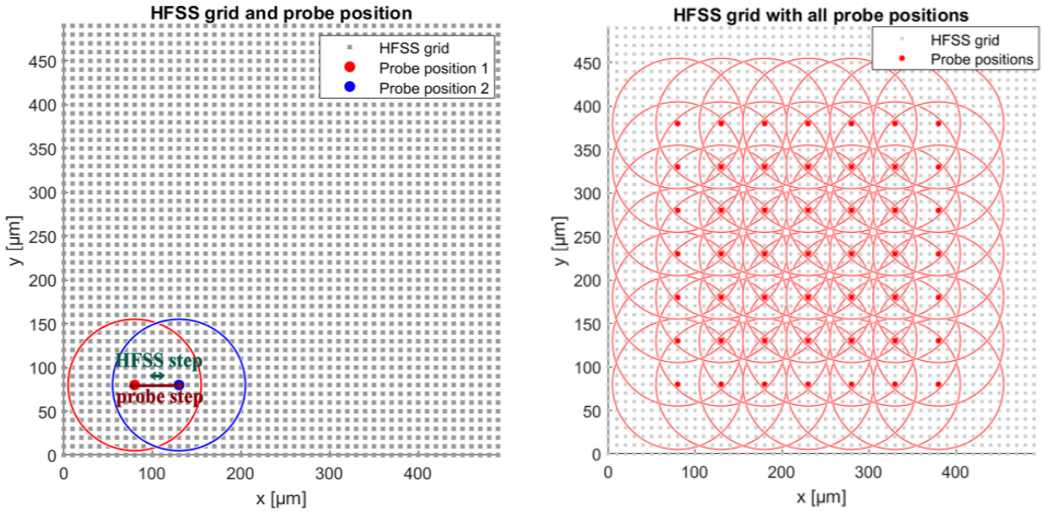
To enable a direct comparison between experimental near-field measurements and numerical predictions, the output of the magnetic near-field microprobe is reconstructed starting from full-wave EM simulations. The theoretical relationship between the probe voltage and the magnetic field, derived in the previous section, is here employed to reproduce the measurement process in a numerical environment.

The reconstruction procedure begins with the modeling of the DUT in Ansys HFSS. The model includes a representation of the geometry, material properties, and excitation conditions, defined to replicate the operating state used during experimental measurements. In addition, in the simulation environment, planar surfaces are defined in the region above the DUT, at fixed distances from the device, corresponding to the probe heights used during the near-field scanning measurements. This allows the simulated field data to be spatially aligned with the measurement grid used during scanning, as schematically illustrated in Fig. 5.5.

Once the model is defined, a frequency-domain EM simulation is performed, yielding the spatial distribution of the magnetic field in the vicinity of the DUT. Since the experimental measurements are carried out using horizontal magnetic probes,

the magnetic field component of interest is the one normal to the DUT surface. Assuming that the DUT lies in the x–y plane, this corresponds to the H_z component of the magnetic field.

The magnetic field component $H_z(x,y)$ is evaluated on the defined extraction plane in HFSS and exported as a numerical dataset. This dataset constitutes the input for the numerical reconstruction of the probe measurement output. The field extraction grid defined in HFSS is chosen to be finer than the spatial resolution of the experimental scan, in order to have a sufficient number of simulated field samples fall within the area enclosed by the probe loop.



(a) (b)

Fig. 5.6 Reproduction of the measurement environment. (a) HFSS simulation step and corresponding probe measurement step configuration. (b) Complete set of probe positions defined on the scanning plane.

The reconstruction and post-processing steps are carried out using MATLAB. As a first step, a discrete sampling grid corresponding to the magnetic field data exported from HFSS is defined, where the grid represents the spatial discretization used in the EM simulation. In addition, a discrete scanning grid is defined to replicate the spatial positions assumed by the probe during the experimental measurement. Each point of this latter grid corresponds to the center position of the probe loop for a given measurement location. Furthermore, the geometry of the probe loop is defined so as to reflect the actual diameter and orientation of the probe used during

the measurements. As illustrated in Fig. 5.6(a), a simplified representation of the reconstruction environment shows the dense HFSS sampling grid together with the successive probe positions defined for the numerical scan. The relationship between the two grids highlights how the finer simulation mesh enables accurate spatial averaging within each probe position. Fig. 5.6(b) depicts the complete set of probe positions over the predefined scanning plane, corresponding to the measurement grid used during the experimental campaign.

For each probe position, only the simulation field samples located inside the probe loop area are considered in the reconstruction process. The magnetic field sensed by the probe is defined as the spatial average of the magnetic field component normal to the DUT surface over the area enclosed by the probe loop. In continuous form, this average field can be expressed as

$$H_{\text{avg}} = \frac{1}{A} \int_A H_z(x,y)\, dA, \tag{5.8}$$

where A denotes the area enclosed by the probe loop and $H_z(x,y)$ is the normal component of the magnetic field evaluated on the extraction plane.

In practice, the magnetic field distribution obtained from HFSS is available only at discrete sampling points corresponding to the simulation step. Under this condition, the surface integral can be approximated by a discrete summation. If a uniform sampling grid is assumed, the average magnetic field can be written as

$$H_{\text{avg}} \approx \frac{1}{N} \sum_{i=1}^{N} H_z(x_i, y_i), \tag{5.9}$$

where N is the number of simulation sampling points lying within the probe loop area and $H_z(x_i, y_i)$ denotes the magnetic field value at the i-th sampling point.

Subsequently, the procedure is repeated for each probe position defined in the scanning grid, yielding a spatial map of H_{avg}.

Considering the relationship previously derived for an ideal magnetic loop probe in (5.7), the average magnetic field H_{avg} computed from the electromagnetic simulation can be directly related to the induced probe voltage. However, this expression

assumes an ideal probe, neglecting several practical effects such as finite loop impedance, probe geometry deviations, and internal losses.

To account for these non-idealities, a probe-specific correction factor is introduced. The real probe response can be modeled by including a probe transfer factor N_P, yielding

$$V_{\text{meas}} = -j\omega\mu_0 S N_P H_{\text{avg}}, \tag{5.10}$$

where N_P represents the effect of probe non-idealities on the electrical response of the probe to the applied magnetic field.

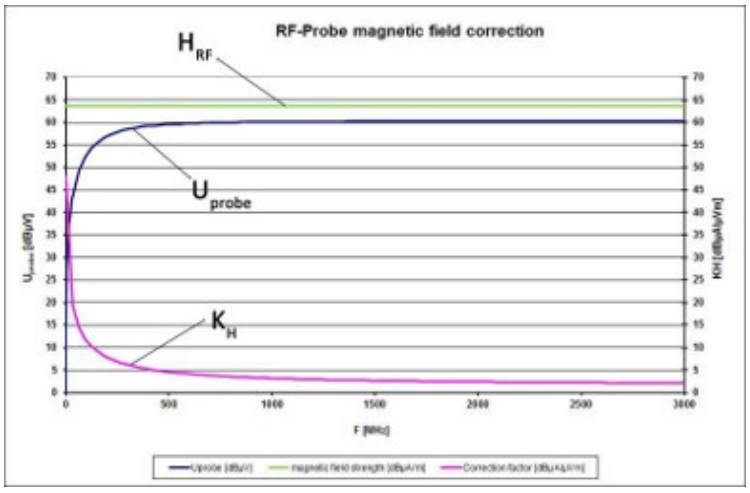


Fig. 5.7 Correction factor K_H provided by manufacturer [158].

Probe manufacturers provide a calibrated correction factor obtained through experimental characterization of the probe in a known and spatially uniform magnetic field. This calibration procedure accounts for the frequency-dependent response of the real probe as well as for geometric and electrical non-idealities. As a result, the correction factor establishes a direct and experimentally validated relationship between the magnetic field at the probe location and the voltage measured at the probe output, as schematically in Fig. 5.7.

The probe-specific correction factor, denoted as K_H, therefore embeds the complete frequency response of the probe and eliminates the need for explicit analytical modeling of the probe itself. Since K_H is obtained under controlled and repeatable field conditions, it provides a reliable link between the measured voltage and the corresponding magnetic field intensity.

Accordingly, the relationship between the measured voltage signal U_{probe} and the associated magnetic field intensity H_{RF} is provided by the manufacturer in the following form:

$$H_{\text{RF}}\ [\text{dB}\,\mu\text{A/m}] = U_{\text{probe}}\ [\text{dB}\,\mu\text{V}] + K_H\ [\text{dB}\,(\mu\text{A/m})/\mu\text{V}], \tag{5.11}$$

where U_{probe} represents the voltage measured at the spectrum analyzer input, H_{RF} is the corresponding magnetic field intensity, and K_H is the probe-specific correction factor expressed in logarithmic form.

Therefore, considering linear units, the correction factor K_H provides the direct proportionality between the average magnetic field sensed by the probe and the measured voltage, yielding

$$V_{\text{meas}} = \frac{1}{K_H} H_{\text{avg}}. \tag{5.12}$$

This expression represents the final link between the numerically reconstructed average magnetic field H_{avg}, obtained from electromagnetic simulations, and the voltage signal measured by the near-field probe. By applying the inverse correction factor provided by the manufacturer, the simulated magnetic field distribution can be directly converted into an equivalent probe output voltage, enabling a consistent and quantitative comparison between simulation results and experimental measurements.

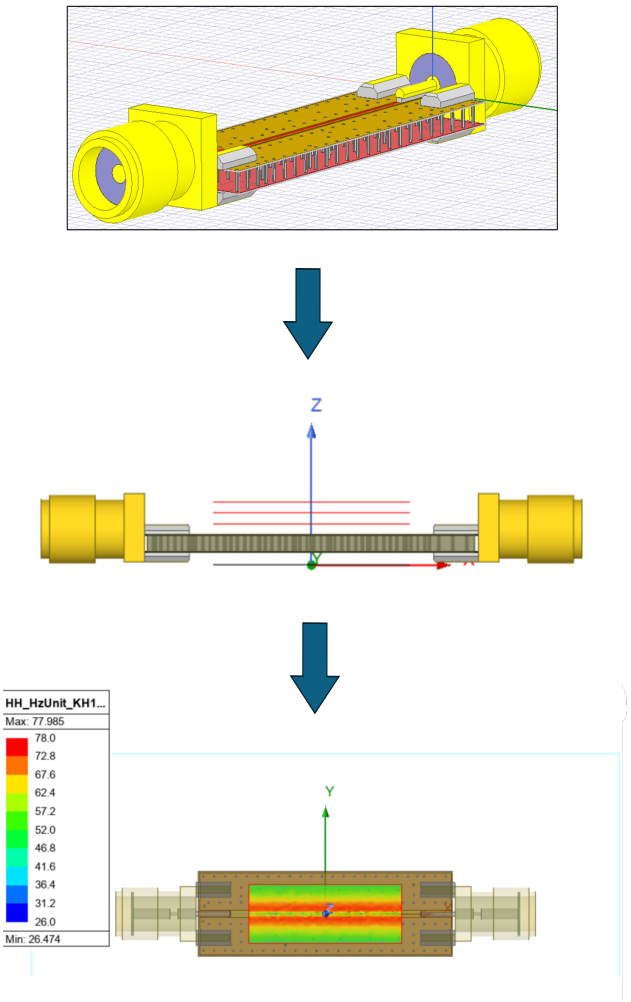
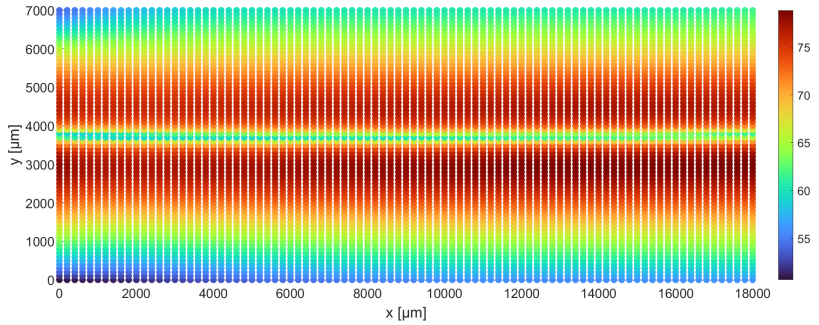


Fig. 5.8 Flow of simulation starting from the modeling of the structure, the definition of the observation plane above the PCB corresponding to the measurement scanning plane, and the resulting spatial distribution of the magnetic field component evaluated on this plane.

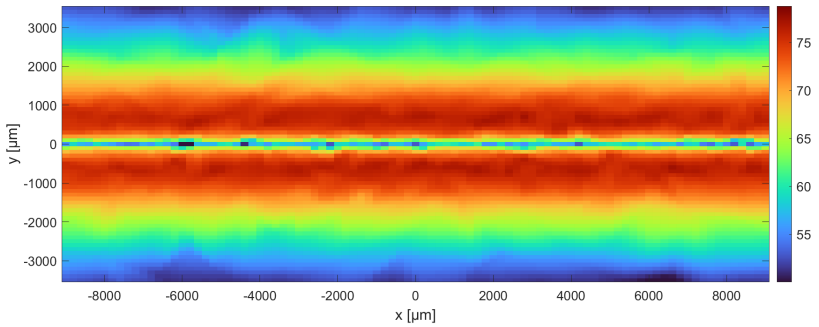
To validate the proposed reconstruction methodology, a simplified test case is considered. The device under test consists of a PCB implementing a coplanar transmission line, modeled in Ansys HFSS. Figure 5.8 provides an overview of the simulation setup, showing the HFSS model of the coplanar transmission line, the extraction plane defined above the DUT, and the corresponding H_z magnetic field distribution used for comparison with near-field measurements.

Near-field magnetic measurements are performed above the PCB using the procedure described in the previous sections, and the reconstructed probe output voltage is compared with the corresponding simulation results. The resulting measured

and simulated magnetic field distributions is reported in Fig. 5.9(a) and Fig. 5.9(b) respectively.



(a)



(b)

Fig. 5.9 Comparison of the voltage amplitude in dBμV associated with the H_z magnetic field component obtained from (a) near-field measurements using a magnetic microprobe and (b) full-wave electromagnetic simulations performed in HFSS.

The HFSS simulation demonstrates that increasing the spatial resolution of the field sampling, by refining the simulation mesh and by defining a denser extraction grid on the observation plane, would further improve the numerical accuracy of the reconstructed magnetic field distribution. However, this refinements would result in a significant increase in computational cost and simulation time. For this reason, a trade-off is adopted between numerical accuracy and computational efficiency,

selecting a mesh density and field sampling resolution that provide reliable results within a reasonable simulation time.

As illustrated in Fig. 5.9 in the regions located close to the transmission line edges, where the magnetic field intensity reaches its highest values, the discrepancy between measurement and simulation remains limited, with values not exceeding approximately 3–4 dBμV. These areas correspond to the dominant current paths of the coplanar structure, resulting in strong magnetic near-field emissions that are well captured by both the experimental setup and the numerical model.

Conversely, in the central region above the line and in lateral areas farther away from the conductor, where the magnetic field intensity is significantly lower, the difference between measured and simulated values increases and can reach up to approximately 10 dBμV. This behavior is expected, since lower field regions correspond to reduced probe output levels, thereby increasing the sensitivity of the measurements to noise, residual parasitic effects, and numerical discretization uncertainties. In this context, the use of a small-diameter magnetic microprobe with a loop diameter of 100 μm is particularly relevant. The probe provides high spatial resolution and is particularly well suited for the investigation of localized regions exhibiting elevated magnetic field intensities, i.e. the regions located near the transmission line edges.

Overall, the proposed reconstruction approach enables a consistent comparison between simulated and measured near-field data, supporting a physically meaningful interpretation of the microprobe output in terms of the underlying magnetic field distribution.

Chapter 6

Conclusions

This work has addressed the main EMC challenges associated with DC-DC converters, considering the mechanisms underlying electromagnetic disturbance generation, their effects on converter operation, and the techniques adopted to mitigate and characterize such phenomena. The work has first examined the fundamental sources of electromagnetic disturbances and their propagation paths, providing the basis for understanding their impact on system performance and EMC compliance. Particular attention has been devoted to passive EMI filtering, with emphasis on the design and optimization of input filters for converters operating under QSW-ZVS conditions. In this context, an optimal damping methodology has been developed and compared with the conventional converter configuration, highlighting the associated trade-offs between EMI attenuation, damping requirements, and preservation of converter performance and stability.

The dissertation has also investigated the role of commercial EM simulation tools in the design and characterization of power electronic systems. A comprehensive overview of the main commercial solutions has been provided, considering their numerical formulations, geometric representations, physical regimes, and available solution approaches, with particular reference to their applicability to PCB and package structures. Based on this analysis, a methodology for the efficient electromagnetic modeling of PCB and package interconnections has been developed, with the aim of obtaining accurate parasitic extractions while limiting the computational resources required for the simulation. The integration of the extracted electromag-

netic information into circuit-level simulations has then been considered, allowing the influence of parasitic elements on converter voltages and currents to be evaluated under realistic operating conditions.

Particular attention has also been devoted to the generation of time-domain models from frequency-domain EM simulation results. Different modeling and transformation techniques have been examined, highlighting their respective characteristics, advantages, and limitations when applied to broadband electromagnetic behavior. On this basis, a complete broadband modeling methodology has been presented, providing a consistent representation of the extracted parasitic effects over the frequency range of interest and enabling their incorporation into subsequent time-domain circuit simulations.

Finally, the analysis has been extended to radiated electromagnetic phenomena, with particular reference to near-field magnetic emissions. Measurement techniques based on magnetic microprobes have been considered, together with the extraction and post-processing of the corresponding field quantities from EM simulations. The comparison between numerical and experimental results provides a framework for assessing the ability of the electromagnetic models to reproduce the spatial distribution of near-field emissions.

Overall, the results presented in this dissertation highlight the importance of integrating electromagnetic considerations throughout the design and characterization of DC-DC converters. The combined use of analytical approaches, circuit-level simulations and electromagnetic modeling provides a comprehensive framework for investigating EMC-related phenomena, supporting the development of converter designs that account for both electrical performance and electromagnetic behavior from the early stages of the design process.

Publications

[P1] S. Simone, A. Hosseini, F. Gabriele, and F. Pareschi, "Impact of QSW-ZVS on Input EMI Filter Design in DC-DC Converters," *International Journal of Circuit Theory and Applications*, vol. 54, no. 7, pp. 3545–3554, 2026, doi: 10.1002/cta.70455.

[P2] S. Simone, F. Pareschi, D. Lena, and G. Setti, "Simulation Method for Quasi-Static Solver to Effectively Model Parasitic Components Between Package and PCB," in *Proc. IEEE 33rd Conference on Electrical Performance of Electronic Packaging and Systems (EPEPS)*, Toronto, ON, Canada, Oct. 2024, pp. 1–3.

[P3] S. Simone, F. Pareschi, G. Setti, and D. Lena, "Equivalent Skin Effect Model for Time-Domain Analysis Starting From Electromagnetic Simulator Values," in *Proc. 25th International Conference on Thermal, Mechanical and Multi-Physics Simulation and Experiments in Microelectronics and Microsystems (EuroSimE)*, Catania, Italy, Apr. 2024, pp. 1–6.

[P4] S. Simone, F. Pareschi, D. Lena, and G. Setti, "Complete Flow for PCB Design Consideration and Power/Signal Integrity Analysis Based on Broadband Model of Parasitic Elements," *International Journal of Circuit Theory and Applications*, vol. 54, no. 2, pp. 1216–1222, Feb. 2026.

[P5] S. Simone, F. Pareschi, and G. Setti, "Modeling of Parasitic Network of Buck Converter Using Full-Wave EM Solver for Design-Oriented Analysis of the Switching Voltage," in *Proc. International Conference on Numerical Electromagnetic and Multiphysics Modeling and Optimization (NEMO)*, pp. 73, 2026, doi: 10.1109/NEMO66765.2026.11622232.

References

[1] T. Hegarty. An overview of conducted EMI specifications for power supplies. Technical report, SLYY136, Texas Instruments, 2018.

[2] Robert Malczyk, Mateusz Bara, and Haihui Lu. Estimation of SMPS' conducted emission according to CISPR standards. *Applied Sciences*, 12(3):1458, 2022.

[3] Timothy Hegarty. The engineer's guide to EMI in DC-DC converters (part 1): Standards requirements and measurement techniques. *How2Power Today, Texas Instruments*, December 2017.

[4] Qing Hua, Zhijian Pan, Jiaxing Zheng, Shixin Wang, Fazhong Huang, Gongtang Wang, and Junfeng Ren. Parasitic Parameter Extraction and Analysis of High Voltage SiC Intelligent Power Module for Three-Phase Motor Control Applications. *Journal of Physics: Conference Series*, 1168:022104, 2019.

[5] Gregory Sizikov, Avinoam Kolodny, Eby G. Fridman, and Michael Zelikson. Frequency Dependent Efficiency Model of On-Chip DC-DC Buck Converters. In *2010 IEEE 26th Convention of Electrical and Electronics Engineers in Israel (IEEEI)*, pages 651–654, 2010.

[6] Gregory Sizikov, Avinoam Kolodny, Eby G. Fridman, and Michael Zelikson. Efficiency Optimization of Integrated DC-DC Buck Converters. In *2010 17th IEEE International Conference on Electronics, Circuits and Systems (ICECS)*, pages 1208–1211, 2010.

[7] Christian Ostergaard, Claus Kjeldsen, Morten Nymand, and Rakesh Ramachandran. Simulation and Measurement of AC Resistance for a High Power Planar Inductor Design. In *2019 IEEE 13th International Conference on Compatibility, Power Electronics and Power Engineering (CPE-POWERENG)*, pages 1–5, 2019.

[8] Wided Belloumi, Arnaud Breard, Jaleleddine Ben Hadj Slama, and Christian Vollaire. Impact of Layout on the Conducted Emissions of a DC-DC Converter Using Numerical Approach. In *2018 15th International Multi-Conference on Systems, Signals & Devices (SSD)*, pages 287–291, 2018.

[9] A. Bhargava, D. Pommerenke, K. W. Kam, F. Centola, and C. W. Lam. DC-DC Buck Converter EMI Reduction Using PCB Layout Modification. *IEEE Transactions on Electromagnetic Compatibility*, 53(3):806–813.

[10] Keong W. Kam, David Pommerenke, Federico Centola, Cheung-Wei Lam, and Robert Steinfeld. EMC Guideline for Synchronous Buck Converter Design. In *IEEE International Symposium on Electromagnetic Compatibility*, pages 47–52, August 2009.

[11] International Special Committee on Radio Interference (CISPR). Electromagnetic compatibility of multimedia equipment – Emission requirements. CISPR 32, 2015.

[12] International Special Committee on Radio Interference (CISPR). Industrial, scientific and medical equipment – Radio-frequency disturbance characteristics – Limits and methods of measurement. CISPR 11, 2015.

[13] K.W. Kam, D. Pommerenke, Cheung-Wei Lam, and R. Steinfeld. EMI Analysis Methods for Synchronous Buck Converter EMI Root Cause Analysis. In *IEEE International Symposium on Electromagnetic Compatibility (EMC)*, pages 1–7, August 2008.

[14] Zhe Li and David Pommerenke. EMI Specifics of Synchronous DC-DC Buck Converters. Electromagnetic Compatibility Laboratory, University of Missouri-Rolla, 2005.

[15] Texas Instruments. Reduce buck-converter EMI and voltage stress by minimizing inductive parasitics. *Analog Applications Journal*, 2016.

[16] Mark Pavier, Andrew Sawle, Arthur Woodworth, Ralph Monteiro, Jason Chiu, and Carl Blake. High Frequency DC:DC Power Conversion: The Influence of Package Parasitics. In *Eighteenth Annual IEEE Applied Power Electronics Conference and Exposition (APEC)*, volume 2, pages 699–704, 2003.

[17] An Overview of Radiated EMI Specifications for Power Supplies. Technical report, SLYY136, 2018. Texas Instruments.

[18] M. Bucolo, A. Buscarino, C. Famoso, L. Fortuna, M. Frasca, A. Cucuccio, G. Rascona, and G. Vinci. Model identification to validate printed circuit boards for power applications: A new technique. *IEEE Access*, 10:33047–33059, 2022.

[19] Timothy Hegarty. The engineer's guide to EMI in DC-DC converters (part 15): Differential-mode input filter design. *How2Power Today, Texas Instruments*, October 2020.

[20] V. Vorperian. *Fast Analytical Techniques for Electrical and Electronic Circuits*. Cambridge University Press, 2002.

[21] M. K. Kazimierczuk. *Pulse-Width Modulated DC-DC Power Converters*. Wiley, 2 edition, 2015.

[22] Robert W. Erickson and Dragan Maksimović. *Fundamentals of Power Electronics*. Springer, 3 edition, 2020.

[23] R.D. Middlebrook. Input Filter Considerations in Design and Application of Switching Regulators. In *IEEE Industry Applications Society Annual Meeting*, 1976.

[24] R.W. Erickson. Optimal Single Resistors Damping of Input Filters. In *IEEE Applied Power Electronics Conference and Exposition (APEC)*, 1999.

[25] Lei Xing, F. Feng, and Jian Sun. Optimal Damping of EMI Filter Input Impedance. *IEEE Transactions on Industry Applications*, 2011.

[26] Ahmed S. Emara, Denis Romanov, Gordon W. Roberts, Sadok Aouini, Mahdi Parvizi, and Naim BenHamida. Optimized Periodic Sigma-Delta Bitstreams for DC Signal Generation Used in Dynamic Calibration Applications. *IEEE Open Journal of Circuits and Systems*, 1(1):3–12, March 2020.

[27] B. Majmunović, B.A. McDonald, S.Y. Yu, and J. Strydom. 90°-Valley Unified Controller for Zero-Voltage-Switching Quasi-Square-Wave (ZVS-QSW) Boost Converter. *IEEE Transactions on Power Electronics*, 39(6):6930–6940, 2024.

[28] F. Karakaya, Ö. Gülsuna, and O. Keysan. Feasibility of Quasi-Square-Wave Zero-Voltage-Switching Bi-Directional DC/DC Converters with GaN HEMTs. *Energies*, 14(10):2867, 2021.

[29] S. Sharifi, M. Jabbari, and H. Farzanehfard. A New Family of Single-Switch ZVS Resonant Converters. *IEEE Transactions on Industrial Electronics*, 64(6):4539–4548, 2017.

[30] H. Bodur and A.F. Bakan. A New ZVT-ZCT-PWM DC-DC Converter. *IEEE Transactions on Power Electronics*, 19(3):676–684, 2004.

[31] Z. Zhang and K.D.T. Ngo. Multi-Megahertz Quasi-Square-Wave Flyback Converter Using eGaN FETs. *IET Power Electronics*, 10(10):1138–1146, 2017.

[32] I. Stevanovic and B. Wunsch. *Electromagnetic Modeling in Power Electronics*. MDPI, 2021.

[33] Y. Saito, T. Ibuchi, T. Funaki, K. Kawai, and T. Tsuda. A Study on EMI Noise Source Modeling with Voltage Source in Synchronous DC-DC Buck Converter. In *IEEE 11th International Symposium on Power Electronics for Distributed Generation Systems (PEDG)*, pages 470–475, 2020.

[34] J. Chen, Y. Han, Q. Han, and Q. Liu. A DPWM-Based Quasi-Constant Switching Frequency Control for Full ZVS Range Three-Phase Inverter with Reactive Power Transfer Capability. *IEEE Transactions on Industrial Electronics*, 70(5):4912–4921, 2022.

[35] M. Jabbari and M. Mokhtari. High-Frequency Resonant ZVS Boost Converter with Grounded Switches and Continuous Input Current. *IEEE Transactions on Industrial Electronics*, 67(2):1059–1067, 2019.

[36] F. Gabriele, F. Pareschi, G. Setti, R. Rovatti, D. Lena, and M.R. Borghi. Small-Signal Circuit Model for Synchronous Buck DC/DC Converter Featuring ZVS at Low-Side. In *IEEE International Symposium on Circuits and Systems (ISCAS)*, pages 1–5, 2023.

[37] G. Liu, H. Ouyang, and M. Xiao. Optimal Design of High Frequency High Efficiency and High-Power Density DC-DC Power Module Based on GaN. *IET Power Electronics*, 16(10):1667–1682, 2023.

[38] R.D. Middlebrook and S. Cuk. A General Unified Approach to Modelling Switching-Converter Power Stages. In *IEEE Power Electronics Specialists Conference*, pages 18–34, 1976.

[39] F. Gabriele, F. Pareschi, G. Setti, R. Rovatti, G. Calderoni, D. Lena, and M.R. Borghi. Small-Signal Model of a Boost Converter Exploiting ZVS at the High-Side MOSFET. In *IEEE 67th International Midwest Symposium on Circuits and Systems (MWSCAS)*, pages 1352–1356, 2024.

[40] V. Vorperian. Simplified Analysis of PWM Converters Using Model of PWM Switch. Continuous Conduction Mode. *IEEE Transactions on Aerospace and Electronic Systems*, 26(3):490–496, 1990.

[41] Hao Zhang. Simple Solution for Input Filter Stability Issue in DC/DC Converters. Technical report, SLUA929A, Texas Instruments, 2019.

[42] Timothy Hegarty. The engineer's guide to EMI in DC-DC converters (part 3): Understanding power stage parasitics. *How2Power Today, Texas Instruments*, March 2018.

[43] Loris Pace, Nadir Idir, Thierry Duquesne, and Jean-Claude De Jaeger. Parasitic Loop Inductances Reduction in the PCB Layout in GaN-Based Power Converters Using S-Parameters and EM Simulations. *Energies*, 14(5):1495, 2021.

[44] Wenchao Tian, Hao Cui, and Wenbo Yu. Analysis and Experimental Test of Electrical Characteristics on Bonding Wire. *Electronics*, 8(3):365, 2019.

[45] Maide Bucolo, Arturo Buscarino, Luigi Fortuna, Carlo Famoso, Mattia Frasca, Antonino Cucuccio, Gaetano Rascon'a, and Giovanni Vinci. A comparative analysis of computer-aided design tools for complex power electronics systems. *Energies*, 14(22):7729, November 2021.

[46] Florian Sawallich and Hans-Günter Eckel. Quantification of ANSYS Q3D Extractor for Inductive Extraction of Power Modules. 2020.

[47] G. Antonini, A. Ciccomancini Scogna, and A. Orlandi. De-Embedding Procedure Based on Computed/Measured Data Set for PCB Structures Characterization. *IEEE Transactions on Advanced Packaging*, 27(4):597–602, November 2004.

[48] Zhaoqing Chen. A Simple Lumped Port S-Parameter De-Embedding Method for On-Package-Interconnect and Packaging Component High-Frequency Modeling. In *2008 12th IEEE Workshop on Signal Propagation on Interconnects*, pages 1–4, Avignon, France, 2008.

[49] Mohammad Ali, Jens Friebe, and Axel Mertens. Simplified Calculation of Parasitic Elements and Mutual Couplings of Wide-bandgap Power Semiconductor Modules. In *2020 22nd European Conference on Power Electronics and Applications (EPE'20 ECCE Europe)*, pages P.1–P.10, Lyon, France, 2020.

[50] Ivana Kovacevic-Badstuebner, Ulrike Grossner, and Dan Popescu. Tools for Broadband Electromagnetic Modeling of Power Semiconductor Packages and External Circuit Layouts. In *2020 32nd International Symposium on Power Semiconductor Devices and ICs (ISPSD)*, pages 388–391, Vienna, Austria, 2020.

[51] Quang Le, Tristan Evans, Yarui Peng, and H. Alan Mantooth. PEEC Method and Hierarchical Approach Towards 3D Multichip Power Module (MCPM) Layout Optimization. In *2019 IEEE International Workshop on Integrated Power Packaging (IWIPP)*, pages 131–136, Toulouse, France, 2019.

[52] Tianjiao Liu, Thomas T. Y. Wong, and Z. John Shen. A New Characterization Technique for Extracting Parasitic Inductances of SiC Power MOSFETs in Discrete and Module Packages Based on Two-Port S-Parameters Measurement. *IEEE Transactions on Power Electronics*, 33(11):9819–9833, 2018.

[53] Altair Engineering. Altair FEKO, 2024.

[54] Romanus Dyczij-Edlinger, Guanghua Peng, and Jin-Fa Lee. Efficient finite element solvers for the maxwell equations in the frequency domain. *Computer Methods in Applied Mechanics and Engineering*, 169(3):297–309, 1999.

[55] Haixin Ke and Todd H. Hubing. Low-frequency full-wave finite element modeling using the LU recombination method. *The Applied Computational Electromagnetics Society Journal*, 23(4):303–308, December 2008.

[56] Dan Popescu and Maximilian Treiber. Broadband TCAD mixed-mode simulation framework for predictive modeling of fast dynamic switching events. In *2019 31st International Symposium on Power Semiconductor Devices and ICs (ISPSD)*, pages 327–330, Shanghai, China, 2019.

[57] Jianfang Zhu and Dan Jiao. Eliminating the Low-Frequency Breakdown Problem in 3-D Full-Wave Finite-Element-Based Analysis of Integrated Circuits.

IEEE Transactions on Microwave Theory and Techniques, 58(10):2633–2645, October 2010.

[58] Jianfang Zhu and Dan Jiao. A Theoretically Rigorous Full-Wave Finite-Element-Based Solution of Maxwell's Equations From dc to High Frequencies. *IEEE Transactions on Advanced Packaging*, 33(4):1043–1050, November 2010.

[59] Dan Jiao and Li Xue. Solution to the low-frequency breakdown in full-wave finite-element based analysis of general lossy problems. In *2016 IEEE International Symposium on Antennas and Propagation (APSURSI)*, pages 1129–1130, Fajardo, PR, USA, June 2016.

[60] Jun-Sheng Zhao and Weng Cho Chew. Integral equation solution of Maxwell's equations from zero frequency to microwave frequencies. *IEEE Transactions on Antennas and Propagation*, 48(10):1635–1645, 2000.

[61] Francesca Rapetti and Germain Rousseaux. On quasi-static models hidden in maxwell's equations. *Applied Numerical Mathematics*, 79:92–106, 2014.

[62] Scott E. Kruger. The three quasistatic limits of the maxwell equations, October 2019.

[63] Jianfang Zhu and Dan Jiao. A rigorous solution to the low-frequency breakdown in full-wave finite-element-based analysis of general problems involving inhomogeneous lossy dielectrics and non-ideal conductors. In *2011 IEEE MTT-S International Microwave Symposium*, pages 1–4, Baltimore, MD, USA, June 2011. IEEE.

[64] Chang Che, Huapeng Zhao, Yuandong Guo, Jun Hu, and Hongseok Kim. Investigation of Segmentation Method for Enhancing High Frequency Simulation Accuracy of Q3D Extractor. In *2019 IEEE International Conference on Computational Electromagnetics (ICCEM)*, pages 1–3, 2019.

[65] Lucian-Vasile Ene, Diana-Ramona Sănătescu, Cristian Sandu, Teodor-Catalin Bibirică, and Mihai Iordache. Simulation of Magnetically Coupled Coils in Ansoft Q3D Extractor Program. In *2017 International Conference on Optimization of Electrical and Electronic Equipment (OPTIM) & ACEMP*, pages 202–207, 2017.

[66] Steven Chen and Harish S. Krishnamoorthy. Analysis of Parasitic Inductance in Multi-MHz Frequency Switching Power Converters. In *2022 IEEE International Conference on Power Electronics, Drives and Energy Systems (PEDES)*, pages 1–5, 2022.

[67] Kailin Zhang, Miao Cai, Minghui Yun, Lei Song, and Daoguo Yang. Comparison Experiment of Parasitic Inductance Extraction of Power Module Based on ANSYS Q3D Software. In *2021 IEEE SSLChina: IFWS*, pages 58–60, 2021.

[68] Hocine Daou, Menouar Ameziani, Dominique Lhotellier, Francois Costa, Mickael Petit, and Eric Laboure. Dynamic Electric Model for IGBT Power Module Based on Q3D and Simplorer. In *2016 International Conference on Electrical Systems for Aircraft, Railway, Ship Propulsion and Road Vehicles (ESARS-ITEC)*, pages 1–6, 2016.

[69] Tianjiao Liu, Yanjun Feng, Runtao Ning, Thomas T. Y. Wong, and Z. John Shen. Extracting Parasitic Inductances of IGBT Power Modules with Two-Port S-Parameter Measurement. In *2017 IEEE Transportation Electrification Conference and Expo (ITEC)*, pages 281–287, 2017.

[70] Wided Belloumi, Arnaud Breard, Omssad Hajji, Christian Vollaire, and Jaleleddine Ben Hadj Slama. Automatic PCB Layout Optimization of a DC-DC Converter Through Genetic Algorithm Regarding EMC Constraints. *IEEE Access*, November 2021.

[71] Shilong Gou, Gang Dong, Zheng Mei, and Yintang Yang. Accurate Inductance Modeling of 3-D Inductor Based on TSV. *IEEE Microwave and Wireless Components Letters*, 28(10):900–902, 2018.

[72] Haidong Wu, Gang Dong, Wei Xiong, Changle Zhi, Shen Li, Zhangming Zhu, and Yintang Yang. Accurate Magnetic Coupling Coefficient Modeling of 3-D Transformer Based on TSV. *IEEE Microwave and Wireless Components Letters*, 32(12):1419–1422, 2022.

[73] Ansys Inc. *Ansys Q3D Extractor Help*, 2025.

[74] *Ansys Q3D SI Getting Started Module 1: Q3D Introduction*.

[75] *Ansys Q3D Getting Started Module 2: Q3D Workflow*.

[76] Ansys Inc. *Ansys Q3D Getting Started Module 3: Solution Setup*, 2020.

[77] Ansys Inc. *Ansys Q3D Getting Started Module 4: Capacitance Matrix*, 2020.

[78] Ansys Inc. *Ansys Q3D Getting Started Module 5: Inductance Matrix*, 2020.

[79] Antonio Ciccomancini Scogna, ChunTong Chiang, Linus Lau, LianKheng Teoh, and HsuenYen Lee. Modeling methodologies for multi level PCB-package co-simulation & co-design. In *2013 IEEE 22nd Conference on Electrical Performance of Electronic Packaging and Systems (EPEPS)*, pages 57–57, October 2013.

[80] Zhaoqing Chen. A lumped/discrete port de-embedding method by port connection error-cancelling network in full-wave electromagnetic modeling of 3D integration and packaging with vertical interconnects. In *2013 IEEE 63rd Electronic Components and Technology Conference (ECTC)*, pages 1980–1987, May 2013.

[81] Antonio Ciccomancini Scogna, Chun Tong Chiang, Klaus Krohne, Lian Kheng Teoh, and Hsuen-Yen Lee. Signal Integrity analysis for high speed channels in pcb/package co-design interface: 3D full wave vs. 2d/hybrid approach & full model vs. segmentation approach. In *2013 IEEE 15th Electronics Packaging Technology Conference (EPTC 2013)*, pages 585–588, December 2013.

[82] Zhaoqing Chen. A general co-design approach to multi-level package modeling based on individual single-level package full-wave S-parameter modeling including signal and power/ground ports. In *2012 IEEE 62nd Electronic Components and Technology Conference (ECTC)*, pages 1687–1694, May 2012.

[83] Jianmin Zhang, Antonio Ciccomancini Scogna, Tracey Vincent, Hong Shi, and Hui Liu. System level simulation solutions for high-speed channels - Package and PCB interface. In *2013 IEEE International Symposium on Electromagnetic Compatibility - EMC 2013*, pages 593–598, August 2013.

[84] Yin-Cheng Chang, Shawn S. H. Hsu, Da-Chiang Chang, Jeng-Hung Lee, Shuw-Guann Lin, and Ying-Zong Juang. A de-embedding method for extracting S-parameters of vertical interconnect in advanced packaging. In *2011 IEEE 20th Conference on Electrical Performance of Electronic Packaging and Systems (EPEPS)*, pages 219–222, October 2011.

[85] LianKheng Teoh, ChunTong Chiang, Antonio Ciccomancini Scogna, Klaus Khrone, and HsuenYen Lee. De-embedding method and segmentation approach using full wave solver for high speed channels in PCB/package co-design. In *2014 IEEE Electrical Design of Advanced Packaging & Systems Symposium (EDAPS)*, pages 33–36, December 2012.

[86] Hansel Dsilva, Abhishek Jain, Sasikala J, and Amit Kumar. Effective Segmentation approach of Package-to-PCB modeling using Full-Wave EM field Solver. In *2020 IEEE Electrical Design of Advanced Packaging and Systems (EDAPS)*, pages 1–3, December 2020.

[87] Jenny Xiaohong Jiang, Chit Zhung Tan, Xinyun Guo, Lei Hua, Yee Huan Yew, Nate Unger, Hui Liu, and Pheak Ti Teh. A Novel Modular Design and Modeling Methodology for High Speed High Density Die Package PCB Co-Simulation and Model Library Creation. In *2016 IEEE 66th Electronic Components and Technology Conference (ECTC)*, pages 2264–2269, May 2016.

[88] Om P. Mandhana. Decoupling optimization for IC-package and PCB systems considering high performance microprocessor core and signal interface interactions. In *2012 IEEE 62nd Electronic Components and Technology Conference (ECTC)*, pages 1800–1807, May 2012.

[89] Marc E. Kowalski and Patrick Codd. Co-Simulation of IC, Package and PCB Power Delivery Networks in Ultra-Low Voltage Power Rail Designs. In *2007*

Proceedings 57th Electronic Components and Technology Conference, pages 798–803, 2007.

[90] Heesok Lee, Jisoo Hwang, Hoi-jin Lee, and Youngmin Shin. A New SI-PI co-Simulation Approach for Efficient Consideration of Coupling Between PDN and SDN. In *2019 IEEE 69th Electronic Components and Technology Conference (ECTC)*, pages 682–687, 2019.

[91] Sidina Wane and An-Yu Kuo. Chip-package co-design methodology for global co-simulation of re-distribution layers (RDL). In *2008 IEEE 17th Conference on Electrical Performance of Electronic Packaging (EPEP)*, pages 59–62, 2008.

[92] Darryl Kostka, Taigon Song, and Sung Kyu Lim. 3D IC-package-board co-analysis using 3D EM simulation for mobile applications. In *2013 IEEE 63rd Electronic Components and Technology Conference (ECTC)*, pages 2113–2120, 2013.

[93] Seungwon Kim, Ki Jin Han, Youngmin Kim, and Seokhyeong Kang. Fast chip-package-PCB coanalysis methodology for power integrity of multi-domain high-speed memory: A case study. In *2018 Design, Automation & Test in Europe Conference & Exhibition (DATE)*, pages 885–888, 2018.

[94] S. Piersanti, F. De Paulis, A. Ciccomancini Scogna, M. Swaminathan, and A. Orlandi. Electromagnetic simulation of 3D stacked ICs: Full model vs. S-parameter cascaded based model. In *2014 IEEE International Symposium on Electromagnetic Compatibility (EMC 2014)*, pages 57–62, August 2014.

[95] Xiaohong Jiang and Hong Shi. Effective die-package-PCB co-design methodology and its deployment in 10 Gbps serial link transceiver FPGA packages. In *2009 IEEE MTT-S International Microwave Symposium Digest (MTT)*, pages 793–796, June 2009.

[96] Lakshya Saini and Ravinder Agarwal. Package Board Co-Simulation Using Equivalent Circuit Modeling Method for High-Speed System. *International Journal of Membrane Science and Technology*, 10(4):472–480, September 2023.

[97] Yoginder Kumar Negi and N. Balakrishnan. Tridiagonal and Block Tridiagonal Computed Sparse Preconditioners for Large Electrodynamic Electric Field Integral Equation (EFIE) Solution. *IEEE Transactions on Antennas and Propagation*, 2022.

[98] Bangda Zhou and Dan Jiao. Direct Finite-Element Solver of Linear Complexity for System-Level Signal and Power Integrity Co-Analysis. In *2014 IEEE International Conference on Signal and Power Integrity (SIPI)*, pages 721–726, 2014.

[99] B. Gustavsen and A. Semlyen. Rational Approximation of Frequency Domain Responses by Vector Fitting. *IEEE Transactions on Power Delivery*, 14(3):1052–1061, July 1999.

[100] A. Semlyen and B. Gustavsen. Vector Fitting by Pole Relocation for the State Equation Approximation of Nonrational Transfer Matrices. *Circuits, Systems, and Signal Processing*, 19(6):549–566, 2000.

[101] B. Gustavsen and A. Semlyen. A Robust Approach for System Identification in the Frequency Domain. *IEEE Transactions on Power Delivery*, 19(3):1167–1173, July 2004.

[102] C. K. Sanathanan and J. Koerner. Transfer Function Synthesis as a Ratio of Two Complex Polynomials. *IEEE Transactions on Automatic Control*, 8(1):56–58, January 1963.

[103] W. Beyene and J. Schutt-Ainé. Accurate Frequency-Domain Modeling and Efficient Circuit Simulation of High-Speed Packaging Interconnects. *IEEE Transactions on Microwave Theory and Techniques*, 45(10):1941–1947, October 1997.

[104] K. L. Choi and M. Swaminathan. Development of Model Libraries for Embedded Passives Using Network Synthesis. *IEEE Transactions on Circuits and Systems II*, 47(4):249–260, April 2000.

[105] M. Elzinga, K. Virga, L. Zhao, and J. L. Prince. Pole-Residue Formulation for Transient Simulation of High-Frequency Interconnects Using Householder LS Curve-Fitting Techniques. *IEEE Transactions on Components, Packaging and Manufacturing Technology*, 23(1):142–147, March 2000.

[106] M. Elzinga, K. Virga, and J. L. Prince. Improved Global Rational Approximation Macromodeling Algorithm for Networks Characterized by Frequency-Sampled Data. *IEEE Transactions on Microwave Theory and Techniques*, 48(9):1461–1467, September 2000.

[107] J. Morsey and A. C. Cangellaris. PRIME: Passive Realization of Interconnects Models from Measured Data. In *IEEE Topical Meeting on Electrical Performance of Electronic Packaging*, pages 47–50, 2001.

[108] Piero Triverio, Stefano Grivet-Talocia, Michel S. Nakhla, Flavio G. Canavero, and Ramachandra Achar. Stability, Causality, and Passivity in Electrical Interconnect Models. *IEEE Transactions on Advanced Packaging*, 30(4):795–808, November 2007.

[109] Mathias Magdowski, Sergey Kochetov, and Marco Leone. Modeling the Skin Effect in the Time Domain for the Simulation of Circuit Interconnects. In *Proceedings of the 2008 International Symposium on Electromagnetic Compatibility (EMC Europe)*, pages 1–6, September 2008.

[110] Xiaokang Liu, Flavia Grassi, Giordano Spadacini, Sergio A. Pignari, Francois Trotti, Nicolas Mora, and Werner Hirschi. Behavioral Modeling of Complex Magnetic Permeability With High-Order Debye Model and Equivalent Circuits. *IEEE Transactions on Electromagnetic Compatibility*, 63(3):730–738, 2021.

[111] D. Puyal, C. Bernal, J. M. Burdio, I. Millan, and J. Acero. A new dynamic electrical model of domestic induction heating loads. In *2008 Twenty-Third Annual IEEE Applied Power Electronics Conference and Exposition*, pages 409–414, February 2008.

[112] Yu Cao, R. A. Groves, Xuejue Huang, N. D. Zamdmer, J.-O. Plouchart, R. A. Wachnik, Tsu-Jae King, and Chenming Hu. Frequency-independent equivalent-circuit model for on-chip spiral inductors. *IEEE Journal of Solid-State Circuits*, 38(3):419–426, March 2003.

[113] Michael D. Bryant. A Bond Graph Model of an Electromagnetic Launcher—Part 1: Structure and Details. *IEEE Transactions on Plasma Science*, 39(1):29–39, 2011.

[114] M. J. Tsuk and J. A. Kong. A hybrid method for the calculation of the resistance and inductance of transmission lines with arbitrary cross sections. *IEEE Transactions on Microwave Theory and Techniques*, 39(8):1338–1347, 1991.

[115] Yoshitsugu Otomo and Hajime Igarashi. Synthesis of a Cauer Equivalent Circuit for Electric Devices From Computed and Measured Data. *IEEE Transactions on Power Electronics*, 36(4):4513–4521, 2021.

[116] Ruth V. Sabariego, Brent Vanbroekhoven, Johan Gyselinck, and Patrick Kuo-Peng. RL-Ladder Circuit Models for Eddy-Current Problems With Translational Movement. *IEEE Transactions on Magnetics*, 58(9):1–4, 2022.

[117] Chiu-Chih Chou and Jose E. Schutt-Aine. Equivalent Circuit Synthesis of Multiport *S* Parameters in Pole–Residue Form. *IEEE Transactions on Components, Packaging and Manufacturing Technology*, 11(11):1971–1979, November 2021.

[118] Bjørn Gustavsen and H. M. Jeewantha De Silva. Inclusion of Rational Models in an Electromagnetic Transients Program: Y-Parameters, Z-Parameters, S-Parameters, Transfer Functions. *IEEE Transactions on Power Delivery*, 28(2):1164–1174, April 2013.

[119] F. De Leon and A. Semlyen. Time domain modeling of eddy current effects for transformer transients. *IEEE Transactions on Power Delivery*, 8(1):271–280.

[120] A. Kameari, H. Ebrahimi, K. Sugahara, Y. Shindo, and T. Matsuo. Cauer ladder network representation of eddy-current fields for model order reduction using finite-element method. *IEEE Transactions on Magnetics*, 54(3):1–4, 2018.

[121] Korawich Niyomsatian, Johan Gyselinck, and Ruth V. Sabariego. Time-domain homogenization of multiturn windings based on RL cauer ladder networks. *International Journal of Numerical Modelling: Electronic Networks, Devices and Fields*, 33(5):e2649, 2020.

[122] Hamed Eskandari, Hiroyuki Kaimori, and Tetsuji Matsuo. Second order approximation of nonlinear eddy-current problems by a cauer ladder network. *IEEE Transactions on Magnetics*, 59:1–1, 2023.

[123] Metin Sengul. Foster impedance data modeling via singly terminated LC ladder networks. *Turkish Journal of Electrical Engineering and Computer Sciences*, 2013.

[124] H. A. Wheeler. Formulas for the skin effect. *Proceedings of the IRE*, 30(9):412–424, 1942.

[125] Lawrence J. Giacoletto. Frequency and time domain analysis of skin effects. *IEEE Transactions on Magnetics*, 32(1), 1996.

[126] E. Grotel"uschen, K. P. Dyck, and H. Grabinski. Time domain simulation of skin- and proximity-effect in multiconductor transmission lines. *Archiv f"ur Elektrotechnik*, 75(4):255–260, 1992.

[127] Niels Koster, Oliver Konig, and Oszkar Biro. Proper generalized decomposition with cauer ladder network applied to eddy current problems. *IEEE Transactions on Magnetics*, 57(6):1–4, 2021.

[128] Qingjian Yu and O. Wing. Computational models of transmission lines with skin effects and dielectric loss. *IEEE Transactions on Circuits and Systems I: Fundamental Theory and Applications*, 41(2):107–119, 1994.

[129] Oszkar Biro and Niels Koster. Generating a cauer ladder network representation of eddy current fields using scalar potentials. *IEEE Transactions on Magnetics*, 58(9):1–4, 2022.

[130] J. Acero and C. R. Sullivan. A dynamic equivalent network model of the skin effect. In *2013 Twenty-Eighth Annual IEEE Applied Power Electronics Conference and Exposition (APEC)*, pages 2392–2397, Long Beach, CA, USA, March 2013. IEEE.

[131] M. Admane, M. Sorine, and Q. Zhang. Simulation of electric transmission lines with skin effect based on a reduced order differential model. In *IET Colloquium on Reliability of Electromagnetic Systems*, pages 16–16. IEE, 2007.

[132] S. Mei and Y. I. Ismail. Modeling skin effect with reduced decoupled R-L circuits. In *Proceedings of the 2003 International Symposium on Circuits and Systems, 2003. ISCAS '03*, pages IV–588–IV–591. IEEE, 2003.

[133] Nadir Idir, Yannick Weens, and Jean-Jacques Franchaud. Skin effect and dielectric loss models of power cables. *IEEE Transactions on Dielectrics and Electrical Insulation*, 16(1):147–154, 2009.

[134] F. M. Rotella, B. K. Bhattacharya, V. Blaschke, M. Matloubian, A. Brotman, Y. Cheng, R. Divecha, D. Howard, K. Lampaert, P. Miliozzi, M. Racanelli, P. Singh, and P. J. Zampardi. A broad-band lumped element analytic model incorporating skin effect and substrate loss for inductors and inductor like components for silicon technology performance assessment and RFIC design. *IEEE Transactions on Electron Devices*, 52(7):1429–1441, 2005.

[135] Shizhong Mei and Y. I. Ismail. Modeling skin and proximity effects with reduced realizable RL circuits. *IEEE Transactions on Very Large Scale Integration (VLSI) Systems*, 12(4):437–447, 2004.

[136] Bhaskar Mukherjee, Lei Wang, and Andrea Pacelli. A practical approach to modeling skin effect in on-chip interconnects. In *Proceedings of the 14th ACM Great Lakes Symposium on VLSI*, pages 266–270. ACM.

[137] Chu-Sun Yen, Z. Fazarinc, and R. L. Wheeler. Time-domain skin-effect model for transient analysis of lossy transmission lines. *Proceedings of the IEEE*, 70(7):750–757, 1982.

[138] S. Kim and D. P. Neikirk. Compact equivalent circuit model for the skin effect. In *1996 IEEE MTT-S International Microwave Symposium Digest*, volume 3, pages 1815–1818. IEEE, 1996.

[139] Andrea Celentano, Carmine Paolino, Fabio Pareschi, Luca Callegaro, Riccardo Rovatti, and Gianluca Setti. Mutual inductance measurement in wireless power transfer systems operating in the MHz range. *IEEE Transactions on Circuits and Systems II: Express Briefs*, 71(3):1715–1720, 2024.

[140] S. Grivet-Talocia and M. Bandinu. Improving the convergence of vector fitting in presence of noise. *IEEE Transactions on Electromagnetic Compatibility*, 48(1):104–120, 2006.

[141] D. Deschrijver and T. Dhaene. Broadband macromodeling of passive components using orthonormal vector fitting. *Electronics Letters*, 41(21):1160–1161, 2005.

[142] Ansys Inc. *Ansys HFSS User Guide*, 2025.

[143] S. Grivet-Talocia and B. Gustavsen. *Passive Macromodeling: Theory and Applications*. John Wiley & Sons, Inc., November 2015.

[144] A. Bhargava, D. Pommerenke, K. Kam, X. Chang, F. Centola, C. Lam, and R. Steinfeld. EMI prediction in switched power supplies by full-wave and non-linear circuit co-simulation. In *2009 IEEE International Symposium on Electromagnetic Compatibility*, pages 41–46. IEEE.

[145] H. Fan, W. Wang, X. Liang, J. Geng, R. Jin, J. Chen, and X. Zhou. A method of accurate co-simulation by considering lumped port setting in EM simulator. In *2015 IEEE 4th Asia-Pacific Conference on Antennas and Propagation (APCAP)*, pages 108–112. IEEE.

[146] J. Wang and H. S. Chung. Impact of parasitic elements on the spurious triggering pulse in synchronous buck converter. In *2013 IEEE Energy Conversion Congress and Exposition*, pages 480–487. IEEE.

[147] Z. Zhang, J. Fu, Y. Liu, and P. Sen. Switching loss analysis considering parasitic loop inductance with current source drivers for buck converters. *IEEE Transactions on Power Electronics*, 26(7):1815–1819.

[148] David M. Pozar. *Microwave Engineering*. John Wiley & Sons, New York, 4 edition, 2011.

[149] Anto K. Davis and Steven M. Sandler. The 2-port shunt-thru measurement and the inherent ground loop. In *EDICON 2018*, August 2018.

[150] Ultra-low impedance (20 micro ohm) measurement using 2-port shunt-through. Technical report, Picotest, 2018.

[151] OMICRON Lab. *Bode 100, Bode 500 Vector Network Analyzer User Manual*, 2025.

[152] S. M. Sandler. Extending the usable range of the 2-port shunt through impedance measurement. In *LAMC*, 2016.

[153] Picotest. New common mode transformer solves PDN 2-port shunt-through measurement hurdle, 2019.

[154] Ultra-low impedance measurements using 2-port measurements. Technical report, Keysight Technologies.

[155] Matt Commens. There's no such thing as ground (but perhaps there's a bob): Minimize your ports. *Ansys*, 2021.

[156] W. Sun. Accurate EM Simulation of SMT Components in RF Designs. In *IEEE Radio Frequency Integrated Circuits Symposium (RFIC)*, 2017.

[157] Chunlei Shi, Wenxiao Fang, Changchun Chai, Yun Huang, Yunfei En, and Yintang Yang. Using termination effect to characterize electric and magnetic field coupling between tem cell and microstrip line. *IEEE Transactions on Electromagnetic Compatibility*, 57(6):1338–1344, 2015.

[158] Langer EMV-Technik GmbH. Near-Field Microprobes for EMC Measurements, 2024.